Modeling and experimental demonstration of an integrated photoelectrochemical hydrogen generator working under concentrated irradiation

PAR

Saurabh Yuvraj TEMBHURNE

EPFL

ÉCOLE POLYTECHNIQUE
FÉDÉRALE DE LAUSANNE

Suisse
2018

Acknowledgements

First and foremost, I would like to thank Prof. Sophia Haussener, for not only being the perfect thesis supervisor but also a great mentor. Thank you for all the brainstorming discussions, guidance, motivation and support throughout the thesis. I learned a lot from you.

I would like to heartily thanks my colleagues at Laboratory of Renewable Energy Science and Engineering for fruitful discussions and for being a great team where I could learn and improvise which finally helped in pursuing a smooth successful thesis. Special thanks to Meng Lin for being a contemporary, friend and having teamed up for many successful academic and non-academic ventures. Also thanks to fellow labmates Mikael Dumortier, Yannick Gaudy and Fouad Abid for creating a friendly and motivating environment during the first year of the thesis which helped in boosting the thesis on a smooth path.

I would like to thank Domine Didier, Jan-Willem Schüttauf and Stephanie Essig from the Centre Suisse d'Electronique et de Microtechnique (CSEM) for useful input and help in characterizations and development of the photovoltaic component. Special thanks to Giancarlo Corradini from Centre of MicroNanotechnology (CMI, EPFL) for discussions and help in wire bonding and preparation of the PV component, and always being ready to help even with short deadlines. I would like to thank Maxime Raton and Marc Jeanneret from the STI-ATME (mechanical workshop) for frequent and fast help in building various mechanical parts. Thanks to Alfred Thomas from ATPR and Dupuis Roland from AFA (EPFL 3d printing workshop) for help and discussions on fast prototyping of various components which eventually helped in quickly updating the better versions of the prototype.

Thanks to Gael Leveque and Clemens Suter from LRESE, EPFL for discussions and help in operation and characterizations under the high flux solar simulator.

Lausanne, 16 Feb 2018   Saurabh Tembhurne

Abstract

The thesis focuses on producing renewable fuels by direct conversion of concentrated solar energy via photoelectrochemical (PEC) approaches, which is one viable route for renewable fuel processing and energy storage. The aim of the Ph.D. thesis is to assess and support the development of solar fuel production and in particular to develop the practical design and operational guidelines in order to stabilize the performance, maximize hydrogen production, energetic efficiencies, and to minimize the cost of solar-fuel generation systems. The thesis presents a novel integrated photoelectrochemical device design, i.e. composed of an integrated traditional photovoltaic component and an electrolyzer component, which allows to circumvent some of the challenges imposed by solid-liquid interface in traditional PEC devices, and has the potential to operate at higher efficiencies and lower cost than externally wired (non-integrated) photovoltaic (PV) plus electrolyzer (EC) devices. Further, the concentration of irradiation is considered reducing the usage of expensive photoactive/catalytic materials and making the device cost-effective.

A fully automated coupled 2D multi-physics non-isothermal model, which uses finite element and finite volume methods to predict the performance of the concentrated integrated PEC (CIPEC) devices, is developed. This validated model is the most complete yet computationally economical model of its kind. Further, the model is exploited formulating thermal management strategies and design guidelines; and showing that the thermal management is the rationale for CIPEC devices. Additionally, the collaborative work is performed on techno-economic and sustainability analysis showing that CIPEC devices can be economically competitive as well as sustainable.

The extensive learnings from the previous modeling work have been deployed to implement a lab-scale CIPEC prototype (A_{PV} = 4 cm^2, A_{EC} = 25 cm^2, C = 474). This resulted in a successful implementation and demonstration of high performance (17.2% solar-to-fuel efficiency) at an operating electrochemical current density of

0.88 A/cm_{EC}^2 (with 6.04 A/cm_{PV}^2) and output power of 27 W, the first demonstration of such high current density/power operation and a step towards production of cost-effective solar fuels. The dissertation further exploits the developed model which led to the design and development of controller/controlling strategies utilizing only the water mass flow to actively track the optimum power point of the system during the day and in turn counteract the adverse effects of frequent and sustained disturbances like weatherly irradiation changes and device degradation.

The thesis shows that concentrated photoelectrochemical approaches can provide a competitive solar fuel processing pathway. The detailed multi-physics model and techno-economic-sustainability model prove that operation of these devices is feasible and dynamic, and can be cost-effective as well as sustainable. The reactant flow based controlling approach shows device's ability to produce in a stable, reliable and robust way in spite of sustained/fluctuating disturbances. Finally, the experimental demonstration strengthens the case for the competitive performance and scalability of these devices. The thesis helps in bridging the gap between academia and practical implementation, and this work may lead to fast realization of these systems.

Keywords: Integrated photoelectrochemical device, Irradiation concentration, Coupled multi-physics model, Design and operational guidelines, Thermal management, Reactant flow-based control, Optimum power point tracker, High-efficiency solar fuel demonstration, High photoelectrochemical current density.

Résumé

Le contenu de ce manuscrit porte sur la production de "combustibles renouvelables" par la conversion directe du rayonnement solaire concentré via des procédés photoélectrochimiques (PEC), ce qui représente une voie prometteuse pour l'exploitation et le stockage des énergies renouvelables. L'objectif global de cette thèse de doctorat est d'analyser les mécanismes physiques en jeu et de proposer des solutions techniques, dans le but de favoriser le développement des combustibles solaires. En particulier, elle se propose d'étudier en détail les paramètres de conception, d'implémentation et d'opération des réacteurs PEC, dans le but de maximiser la production de combustible (hydrogène) et le rendement de conversion, et de minimiser les coûts de production, tout en maintenant une bonne stabilité et durabilité. Cette thèse présente un nouveau concept de réacteur PEC intégré, c'est-à-dire constitué d'un composant photovoltaïque directement intégré à un électrolyseur. Cette configuration permet d'éviter les problèmes de stabilité dus à l'interface solide-liquide qu'on rencontre dans les réacteurs PEC traditionnels, et a le potentiel de fonctionner non seulement à des rendements plus élevés, mais aussi à des coûts plus bas que les systèmes photovoltaïques couplés à un électrolyseur par le biais des câbles électriques (systèmes non intégrés). En outre, la concentration du rayonnement solaire permet de réduire la demande en matériaux photoactifs et catalytiques (qui sont très couteux) et ainsi de rendre la technologie plus compétitive.

Un modèle 2D multiphysique incluant la thermique, qui utilise les méthodes des éléments finis et des volumes finis pour la discrétisation est développé, validé et automatisé, dans le but de prédire la performance du réacteur PEC à concentration. Cela représente le modèle le plus économique de ce genre, du point de vue computationnel. En utilisant ce modèle pour l'analyse des stratégies de gestion thermique et pour l'étude des paramètres de conception, il apparait que la gestion thermique est un enjeu majeur pour la performance des réacteurs PEC à concentration. Des travaux complémentaires portant sur les paramètres techno-

économiques ainsi que la durée de vie mettent clairement en évidence la compétitivité économique et la durabilité de cette typologie de réacteur.

Les résultats des travaux de modélisation sont exploités pratiquement, à travers le développement et l'implémentation d'un prototype de réacteur PEC à concentration, atteignant un facteur de concentration de 474. Ce prototype, qui présente une surface active de 4 cm^2 pour le composant photovoltaïque et 25 cm^2 pour l'électrolyseur, a un excellent rendement de conversion (17.2 %) à une densité de courant de 0.88 A/cm^2 dans l'électrolyseur, et à une puissance de sortie de 27 W. Cette densité de courant, ainsi que la puissance de sortie représentent des records mondiaux, et permettent de faire un grand pas vers la production de combustibles solaires compétitifs. Enfin, cette thèse se sert du modèle multiphysique pour proposer un contrôleur et une stratégie de contrôle qui ajuste la valeur du débit d'eau non seulement pour suivre le point de puissance optimal du système, mais aussi pour contrecarrer les effets défavorables des perturbations journalières ou saisonnières du rayonnement solaire incident, ainsi que les effets de la dégradation des composants du réacteur.

Cette thèse prouve que les réacteurs photoélectrochimiques à concentration peuvent représenter des voies prometteuses pour la production de combustibles solaires. Les modèles multiphysique et technico-économique démontrent que l'application de ces réacteurs est techniquement viable et dynamique, et peut aussi être rentable et durable. La technique de contrôle basée sur l'ajustement du débit du fluide réactif met en évidence la capacité du réacteur à fonctionner de manière stable, fiable et robuste, malgré les fluctuations des conditions opératoires. Enfin, la démonstration expérimentale met en évidence la compétitivité et la flexibilité de ces réacteurs. La thèse permet donc de combler le fossé entre le monde académique et l'application pratique, et ces travaux pourraient déboucher sur la réalisation de ces systèmes.

Mots clés : Réacteur photoélectrochimique intégré, Rayonnement concentré, Modèle multiphysique couplé, Paramètres de conception et d'opération, Gestion thermique, Contrôle basé sur le débit du fluide réactif, Pisteur du point de fonctionnement optimal, Démonstration de réacteur à haut rendement, Haute densité de courant photoélectrochimique.

Table of contents

List of figures

List of figures

List of Tables

List of Symbols

α_a	Anodic charge transfer coefficient	[-]
α_c	Cathodic charge transfer coefficient	[-]
$\mathbf{B}$	Magnetic flux density	[T]
c_0	Speed of light	[m/s]
c_i	Concentration of species i	[mol/m^3]
C	Irradiation concentration	[-]
D_i	Diffusion coefficient of species i	[m^2/s]
$\mathbf{D}$	Electric flux density	[C/m^2]
D_{ik}	Fick diffusivities	[m^2/s]
$\mathbf{d_k}$	Diffusional force acting on species k	[-]
D_i^T	Thermal diffusion coeff.	[kg/(m s)]
$D_{n.th}$	Electron thermal diffusion coeff.	[kg/(m s)]
$D_{p.th}$	Hole thermal diffusion coeff.	[kg/(m s)]
$\mathbf{E}$	Electric field intensity	[V/m]
E_{eq}	Equilibrium potential	[V]
E_g	Bandgap of semiconductor	[eV]
E_{ph}	Photon energy	[eV]
ε_s	Static electric permittivity	[C/m]
ε_0	Vaccum permittivity	[C/m]
ε_p	Porosity	[-]
ε_r	Relative permittivity	[-]
ε_{rr}	Convergence error	[-]

List of symbols

F	Faraday's constant	[A s/mol]
F	Force term accounting for gravitational influence	[kg/m^2/s]
G_{opt}	Optical generation rate	[W/m^3/s]
ΔG	Gibbs free energy	[kJ/mol]
h	Planck constant	[J s]
h_{eff}	Effective heat transfer coeff.	[W/m^2/K]
H	Magnetic field intensity	[A/m]
i_0	Exchange current density	[A/m^2]
I_{in}	Incident radiation flux	[W/m^2]
i_{loc}	Local charge transfer current density	[A/m^2]
I_d	Identity matrix	[-]
J	Current density	[A/m^2]
J_n	Electron current density	[A/m^2]
J_{op}	Operating current density	[A/m^2]
J_p	Hole current density	[A/m^2]
J_l	Electrolyte current density	[A/m^2]
J_s	Electrode current density	[A/m^2]
J_{sc}	Short circuit current density	[A/m^2]
k_B	Boltzmann constant	[J/K]
k_{conc}	Thermal conductivity of concentrator	[W/(m K)]
κ_p	Permeability of the porous medium	[m^2]
k_{ref}	Imaginary part of refractive index	[-]
k_{th}	Thermal conductivity	[W/(m K)]
L_{conc}	Length of concentrator through which heat flows/ mean photon flow length	[m]
$\dot{m}$	Mass flow rate	[g/s]
n	Electron density	[1/m^3]
N_A^-	Ionized acceptor concentration	[1/m^3]
N_D^+	Ionized donor concentration	[1/m^3]
N_c	Effective density of states in conduction band	[1/m^3]

N_{v}	Effective density of states in Valence band	[1/m³]
$\dot{n}_{H_2}$	Molar flow rate of hydrogen	[mol/s]
n_{ref}	Real part of refractive index	[-]
$\eta_{\mathrm{act},m}$	Activation overpotential corresponding to reaction m	[V]
n_{opt}	Quantum yield	[-]
η_F	Faradic efficiency	[-]
η_m	Total overpotential corresponding to reaction m	[V]
η_{STH}	Solar to hydrogen efficiency	[-]
P	Pressure	[Pa]
p	Hole density	[1/m³]
ρ	Density	[kg/m³]
P_{in}	Incident power	[W]
ϕ_{l}	Electrolyte potential	[V]
ϕ_{s}	Electrode potential	[V]
Q_{br}	Mass source or mass sink	[kg/(m³ s)]
Q_{H}	Total heat dissipation density	[W/m³]
Q_k	Electrode (k=s) or electrolyte (k=l) current source term	[A/m³]
Q_{M}	Magnetic losses	[W/m³]
Q_{R}	Resistive losses	[W/m³]
Q_{TH}	Thermalization losses	[W/m³]
$\bar{R}$	Universal gas constant	[J mol⁻¹ K⁻¹]
$\dot{\mathbf{S}}_{\mathrm{av}}$	Time averaged Poynting vector	[W/m²]
σ	Electrical conductivity	[S/m]
T_{init}	Initial temperature	[K]
T_{l}	Lattice temperature	[K]
T_{OP}	Operating temperature of PV/semiconductor	[K]
T_{PV}	Average photovoltaic component temperature	[K]
T_{EC}	Average electrochemical cell temperature	[K]
U	Net recombination rate in PV	[1/m³]

List of symbols

u	Velocity vector	[m/s]
$\mathbf{u}_w$	Velocity field in water channel	[m/s]
$\mathbf{u}_a$	Velocity field in anodic channel	[m/s]
$\mathbf{u}_c$	Velocity field in cathodic channel	[m/s]
μ	Magnetic permeability	[H/m]
μ_d	Dynamic viscosity	[kg/(m s)]
$\mu_{m,i}$	Ionic mobility of species	[mol s/kg]
μ_n	Electron mobility	[m²/(V s)]
μ_p	Hole mobility	[m²/(V s)]
V_{op}	Operating voltage	[V]
V_{oc}	Open circuit voltage	[V]
ν	Frequency of incoming light	[Hz]
υ_{water}	Surface normal velocity of water	[m/s]
ω_i	Mass fraction	[-]
$\boldsymbol{\omega}$	Angular frequency of incoming light	[rad/s]
z_i	Charge no. of ionic species	[-]

ACRONYMS

AMPS	Analysis of microelectronic and photonic structure simulator
AM1.5	Air mass 1.5
ASSA	Active specific surface area
BC	Boundary condition
BOS	Balance of system
BP	Bipolar plate
CB	Conduction band
CCD	Charge coupled device
CIPEC	Concentrated Integrated PhotoElectrochemical
CPV	Concentrated photovoltaics
DC	Direct current
DI	De-ionized
DNI	Direct normal irradiation
DOS	Density of states

EC	Electrochemical component/eletrolyzer
EHP	Electron hole pair
EM	Electromagnetic
FF	Fill factor of PV
GDL	Gas diffusion layer
GHI	Global horizontal irradiation
HER	Hydrogen evolution reaction
HFSS	High flux solar simulator
HT	Heat transfer
IPEC	Integrated PhotoElectrochemical
MEA	Membrane electrode assembly
MOCVD	Metal-organic chemical vapor deposition
MPP	Maximum power point
OER	Oxygen evolution reaction
PEEK	Polyether ether ketone
PCM	Phase change material
PV	Photovoltaic
PEC	Photoelectrochemical
RFF	Reacting fluid flow
SC	Semiconductor
STH	Solar to hydrogen
VB	Valance band

Introduction

Significant and harmful impacts on our health, environment, and climate are being created by overloading the atmosphere with global warming gas emissions caused due to human activities. Burning fossil fuels for heat, electricity and transportation accounts for more than 60% of the global warming gas emissions [1]. In contrast, manufacturing, installation, operation and maintenance, and dismantling and decommissioning— associated with renewable energy have minimal life-cycle global warming emissions [2]. The goal is to reduce the geopolitical tension over the current energy resources, i.e. fossil fuels, by increasing the share of renewable energy resources in driving our economy; and to keep the global temperature rise under the limit. With this goal the need for the development of energy conversion technology and processes for the generation of carbon-free renewable fuels, which can compete with the fossil fuel's prices, is evident. The solar energy received on earth's surface can meet mankind's current and future energy demands [3], [4]. It can be converted into electricity using photovoltaic cells or concentrated solar power technology but the electricity is difficult to store and considerable losses are induced when distributing it over long distances. This problem can be circumvented by converting energy into fuel, the simplest example is the electrolysis of water to produce hydrogen (with $\Delta G = +237\,\text{kJ/mol}$ at 25°C and 1 atm)

$$2\text{H}_2\text{O}_{(l)} \rightarrow \text{O}_{2(g)} + 2\text{H}_{2(g)}\,. \tag{1}$$

The hydrogen can potentially become the main energy carrier in an economy. Additionally, hydrogen can serve as an energy-packed reagent for the formation of methanol, methane, or even hydrocarbons (where atmospheric CO_2 can be used as the carbon feedstock). To realize this future, sustainable hydrogen production approaches are needed. However, this is certainly not the case; today ~96% of the hydrogen production globally is based on steam reforming of conventional fossil fuels [5]. Several possible routes for sustainable hydrogen production are being investigated [6]–[8], which include thermochemical processes [9], fermentation of

biomass [10], [11], and photo-biological processes [12]. In this thesis, the focus is on solar driven hydrogen production using photoelectrochemical pathways.

Traditional photoelectrochemical devices consist of a semiconductor-electrolyte interface where the semiconductor can be single-junction or multi-junction (tandem). Tandem cells based photoelectrochemical devices are one of the best performing devices [13]. In such devices, the potential required for the electrochemical reaction is provided by a combination of dual or multiple semiconductors which have buried solid state junctions and solid-electrolyte junctions. Tandem cells benefit from the fact that smaller band gaps, hence greater solar spectrum response, can be utilized. Efficiencies of around 12.4% (p-GaInP$_2$(Pt)/GaAs photocathode) [14] have been achieved. But the performance could not be sustained because of the stability issues of the photoelectrode materials under operating conditions which suffer from photo-corrosion due to semiconductor-electrolyte interface [15]. The multiple constraints imposed upon such materials are demanding e.g. the band edge's absolute positions are required to straddle the oxidation and reduction redox levels so as to provide a driving force for the reaction, the semiconductor interface also needs to be catalytically active etc. [16]. There has been much effort towards the search of such materials and 100s of compounds have been looked into [17] but no material which could perform well in all the fundamental steps has been found. If we can get rid of the semiconductor-electrolyte interface then this qualifies for many otherwise non-interesting materials and opens new doors.

One simple way to achieve this is by grid-connected PV-electrolysis, but this suffers from inherent resistive losses in the grid and power-electronics' conversion losses. Additionally, this configuration is not really a single device but just a combination of two devices i.e. PV plus electrolyzer connected by the grid. If connected to the grid, annual transmission and distribution losses toward the end user are typically of the order of 7% [18]. The need for inverters and the losses in the grid [19] would be removed if solar cells are directly connected to the electrolyzer instead of via the grid. To substantially reduce the transmission losses and still benefit from the exclusion of semiconductor-electrolyte interface, a novel integrated photoelectrochemical device design is proposed as shown in Fig. 1.1 where the PV and electrolyzer are combined in an integrated (μm-mm scale) fashion.

A key issue for economic competitive PEC devices is the reduction of rare and expensive device components, such as catalysts and light absorbers [20]. This can be achieved by concentrating the solar irradiation.

One needs to simultaneously respect and optimize technical, economic, sustainability, and operating time constraints for device and system design choices for solar energy conversion and storage. This thesis was started with the collaborative work [21] on quasi-transient techno-economic and sustainability analysis to formulate the holistic design guidelines for photoelectrochemical routes of hydrogen production. This modeling provided evidence that the concentrated integrated photoelectrochemical devices can be economically competitive as well as efficient and sustainable. This model, which is based on 0-dimensional physical consideration, accounts for the device and immediate peripheral components (i.e. balance of system- BOS) allowing for the comparison of different device designs with different combinations of materials. The different options for device components are presented in Fig. 1. Here C (concentration of irradiation) is defined as the ratio of A_{conc}/A_{PV} and F (dilution of current) factor is defined as the ratio of A_{EC}/A_{PV} (where A denotes the respective areas).

The results of the techno-economic analysis show that when the time-averaged solar tohydrogen (STH) efficiency is plotted (Fig. 2(a)) against the calculated hydrogen price for varying irradiation concentration (denoted by color of dots) and varying F factor (denoted by size of dots) a Pareto front is formed for most of the device types studied. It is only for the III-V material based PV and Ru-Pt catalyst based concentrated photoelectrochemical device that a Pareto point exists. That indicates that a global optimum exists which maximizes STH efficiency as well as minimizes the hydrogen cost for device type 1 (type 1 = variable C and F). Similar Pareto plots have been discussed in Dumortier et al. [21] for Si PV based device, all of which show the existence of a Pareto front with no global optimum point. In fact, if the limiting point of the Pareto fronts are plotted for the STH efficiency versus hydrogen price analysis, it is found that it is only the optimal configurations of device type 1 (Ru-Pt catalyst with $C = 1000$ and $F = 2$) and of type 2 (Co-Ni catalyst with $C = 1000$ and $F = 2$) which have the highest STH efficiency with the lowest prices, among all the other 16 device types and optimal configurations analysed. Additionally, Fig. 2(b) shows that the optimal configurations of device types 1 and 2 are also the most sustainable (with lowest input energy demand) and most economical device designs.
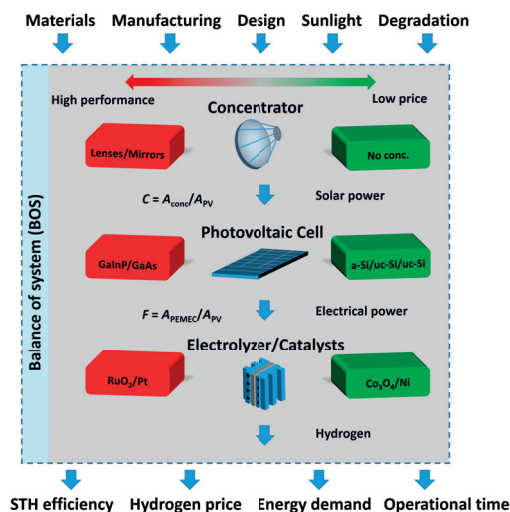
Fig. 1 Schematic showing different options for device components and input/outputs of the quasi-transient techno-economic and sustainability analysis.

Integrated PEC devices, which are composed of a traditional photovoltaics (PV) component closely incorporated with an electrolyzer (EC) component, allow circumventing the challenges imposed by solid-liquid interfaces in traditional PEC devices while operating at higher efficiencies than externally wired (non-integrated) PV plus EC devices. Additionally, the results of the techno-economic and sustainability analysis proved that the III-V based photoelectrochemical devices working with concentrated irradiation are also the most economical as well the most sustainable. This served as the motivation for the thesis to focus on concentrated integrated photoelectrochemical devices and develop a detailed multi-physics model to understand if concentrated irradiation is feasible for PEC devices and to understand the coupled physics inherent in these devices. The model development has been presented in chapter 1 and is exploited for formulating device design and device controlling guidelines in chapter 2 and 3, respectively. Finally, the learnings from chapter 1-3 have been implemented to develop and test a lab-scale prototype, which is presented in chapter 4.
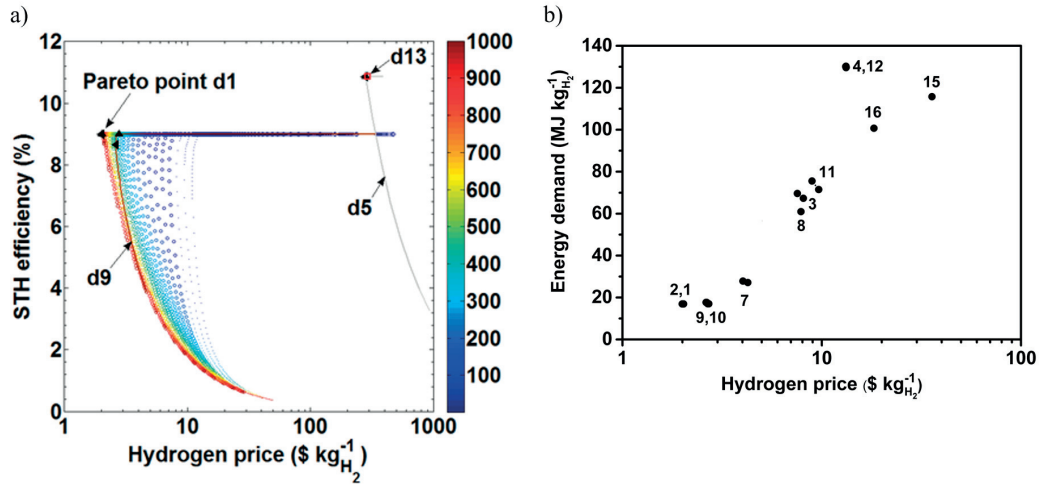
Fig. 2 Plot (a) shows operating time averaged STH efficiency as a function of hydrogen price for III-V/Ru-Pt PV/EC based device types 1 (variable *F* and *C*), 5 (var. *F*, *C* = 1), 9 (*F* = 1, var. *C*) and 13 (*C* = 1, *F* = 1). Point colors indicate the irradiation concentration (indicated by the color bar), *C*, and point sizes indicate the $\log_{10}$ of the current concentration, *F*. Plot (b) shows the limiting points of the Pareto fronts for the input energy demand versus hydrogen price analysis [21].

Chapter 1 presents the development of a detailed multi-physics non-isothermal PEC device model to conduct feasibility studies and to better understand the coupled physical phenomena occurring in integrated photoelectrochemical devices. The development of a 2-dimensional non-isothermal model using finite element and finite volume methods along with the discussion of underlying physics is presented. The model accounts for charge generation and transport in the multi-junction solar cell and the components of the integrated electrolyzer (polymeric electrolyte and solid electrode), electrochemical reaction at the catalytic sites, fluid flow and species transport in the channels delivering the reactant (water) and removing the products (hydrogen and oxygen), radiation absorption (in semiconductor and water) and heat transfer in all components. Various computational techniques to make the model autonomous as well computationally economic are also discussed. The design of the CIPEC device, which is at the center of this thesis, is detailed. Additionally, a sensitivity analysis for material and dimensional parameters, along with a discussion of the 2-dimensional output parameter profiles, is presented. Finally, the model has been validated by comparing the results with experimental data of individual components (PV and EC) from literature. The chapter is concluded with the discussion of the importance of the developed model for the design of CIPEC

devices working at elevated temperatures and an outlook is presented for its exploitation.

Chapter 2 presents the need for the consideration of thermal management in integrated photoelectrochemical devices, particularly for those operating with concentrated irradiation. Details about the modeling of various heat sources in different components of the device are discussed. Parametric analysis is performed for operational parameters (irradiation concentration and reactant flow rate), for material parameters (electrode's exchange current density and active specific surface area), and for dimensional parameters (membrane thickness, catalyst thickness, and gas diffusion layers' thickness). This parametric analysis presents characteristic current-voltage curves, the evolution of temperature as well as the evolution of the different objective functions (efficiency and output production rate) for all parameters studied. The chapter is concluded with the discussion of the importance of water flow rate as an integral part of thermal management, and thermal management is argued to be the rationale for concentrated integrated devices.

Chapter 3 starts with the presentation of the need for the controlling of the photoelectrochemical devices during their lifetime in order to ensure a stable and robust operation. A comparison is presented between the use of an external power electronics versus the use of a reactant mass flow controller to actively track the optimum power point of the device. For this purpose, the model (discussed in chapter 1 and 2) is extended to incorporate the realistic degradation phenomena for the various components of the device. This extended model is then used for performing the yearly degradation (sustained disturbance) analysis and daily irradiation variation (frequent disturbance) analysis, both of which highlight the positive effects of the smart control of the reactant mass flow rate on the overall performance of the device, enabling stability and security of the product's supply.

Chapter 4 discusses the details of the design, fabrication, implementation, and testing of the lab-scale prototype (157 W input power) of the integrated photoelectrochemical device working with concentrated irradiation. A comprehensive review of all the major demonstrations, from 1965-2017, for the photoelectrochemical production of hydrogen is also presented with the detailed categorization of the materials and device-configurations. The PV material categorization includes cheap/expensive and Si or III-V based, the EC material categorization includes cheap/expensive and rare/abundant element based, and the PV and catalyst configurations are categorized as integrated, partially integrated and non-integrated along with PV being single/multi-junction. Methods and results of the preparation and protection of the PV component for its stable operation under deionized water immersion are discussed. In addition, the experimental techniques

for the preparation of the electrolyzer component, as well the testbench developed for testing of the CIPEC devices is also presented. The discussion is also presented for the validation of the results obtained with the 2-dimensional model. Finally, the implemented device and system's dynamic response testing, stability testing and performance figures at varying irradiation concentrations are discussed.

Two Dimensional Non-Isothermal Multi-physics Modeling[1]

1.1 Introduction

Integrated photoelectrochemical (IPEC) devices, i.e. composed of an integrated "buried" [16] photovoltaic (PV) component and an integrated electrochemical component (consisting of membrane-separated catalysts and porous charge collectors), as discussed earlier, allow circumvention of some of the challenges imposed by solid-liquid interfaces in traditional PEC devices, while also exhibiting potential to operate at higher efficiencies and lower cost than externally wired (non-integrated) PV plus electrolyzer (EC) devices [19], [22], [23]. The design is referred as "integrated" to signify that the PV and electrolyzer components are in direct contact (and area-matched for particular design discussed in this chapter), allowing heat transfer from one component to the other and for thermal management strategies to be applied. In order to increase the economic competitiveness of IPEC devices compared to conventional hydrogen generation pathways, the concentration of irradiation [20], [21], [24] is considered. This leads to large driving current densities (approximately proportional to the concentration factor), and thus introduces larger overpotentials and potential mass transport limitations [25]. Concentration also decreases the performance of the photoactive components due to increased temperature. On the other hand, the kinetics are enhanced with increased temperature. Ionic transport in the solid electrolyte is also enhanced with increased temperature, but this increase stops abruptly and sharply drops at temperatures above 120°C due to membrane dry-out [22], [26], [27]. This competing and coupled behavior of the components requires a detailed understanding of the heat transfer, charge transport, fluid flow, and reaction kinetics in order to formulate performance

---

[1] The material from this chapter has been published in Journal of Electrochemical Sociecity under the reference 'S. Tembhurne and S. Haussener, *J. Electrochem. Soc.*, 2016, **163**, 988–998'.

optimization strategies for concentrated integrated photoelectrochemical (CIPEC) cells via device design and adaptation of the operational conditions.

Multi-physics computational models are a crucial support in device design and engineering. They allow in-depth analysis of conceptual designs, support feasibility investigations of devices and integrated systems, and permit the quantification of performance. Modeling efforts of PEC and specifically IPEC devices are limited. The earliest attempts used lumped-circuit models of a photocell in series with a current-dependent electrochemical load [28]. Berger et al. [29] presented a basic 1-dimensional model for light absorbers and electrolyzers with applicability to both wired and wireless PEC systems. Gaudy et al. [30] extended the 1D model by adding detailed wave propagation modeling and an advanced semiconductor-electrolyte interface model accounting for pinning and unpinning of interface states. Haussener et al. [22], [31] developed a 2-dimensional PEC model focusing on the charge transport in the electrolyte and reaction kinetics incorporating the idealized Shockley-Queisser limit for the photoabsorber approximation. In Haussener et al. [22], an isothermal model was used to provide predictions for the temperature-dependent performance behavior of PEC devices.

However, none of the modeling efforts accounted for the detailed solution of the energy conservation and the resulting corresponding spatial variations in temperature. Understanding these variations assists the development of thermal management strategies to benefit overall performance, i.e. guiding operation and design to maximize high-temperature advantages in kinetics and transport while minimizing high-temperature disadvantages in charge transport and recombination in the photoabsorber. Thermal management is, therefore, a rationale for CIPEC device designs. The formulation of detailed guidelines not only requires the solution of the energy conservation in a multi-dimensional design, but also the detailed modeling of charge transport in the semiconductor materials in order to reliably predict charge separation and recombination. Furthermore, the detailed prediction of the charge generation (the radiation absorption) in a nanostructured heterogeneous component is needed, requiring the solution of Maxwell equations instead of the usually applied Beer's law. None of the modeling efforts, up till now, have accounted for all of these phenomena, namely a coupled 2-dimensional multi-physics model for light propagation and absorption, semiconductor physics, fluid flow and reaction kinetics, and energy conservation. Such advanced multi-physics, multi-dimensional models require focusing on the accurate definition of the boundary conditions between the components and the consistency of the physical phenomena. The various conservation and transport equations must be solved with accurate interface conditions for component coupling. This coupling introduces additional complexity, as detailed component models accounting for a subset of

physical phenomena rely on the solution of other subsets of equations. Consequently, such coupled modeling efforts require additional external iterative solution steps, which generally increases computational efforts and features challenges related to model robustness. These complexities are addressed in this chapter.

An advanced multi-physics and multi-scale numerical modeling tool has been developed to assist in designing and building an integrated photoelectrochemical device using concentrated solar irradiation. The IPEC device is shown in Fig. 1.1(a). A variation of this design is presented in Fig. 1.11 which integrates a novel self-tracking concentrator [32] and provides additional design considerations specific to that design. Concentrated solar irradiation irradiates the device from the x-direction where it is delivered and absorbed by a buried dual/triple-junction (e.g. $Ga_{0.51}In_{0.49}P$-GaAs or aSi-ucSi-ucSi) PV cell. The radiation arriving at the PV cell produces electron-hole-pairs (EHPs) if the radiation energy exceeds the bandgap energy of the absorber materials and is effectively absorbed. The charge carriers are then delivered to the electrochemical components, i.e. the solid electrolyte and the catalysts, building the integrated electrolyzer. The arrangement of the PV and EC can be done either in p-n-cathodic-anodic configuration, shown in Fig. 1.1(a), or n-p-anodic-cathodic configuration. The holes are delivered to the anode causing oxidation of water and production of oxygen and protons at the catalytic sites. The protons travel to the cathode through the polymeric electrolyte where they are reduced by the electrons delivered from the PV's n-terminal to produce hydrogen at the catalytic sites. A water channel between the irradiation input (or concentrator exit) and the PV cell is introduced to cool the PV cell as well as to preheat the reactant (water) before it enters the anodic electrolyzer channels. The connection between the water channel and the anodic chamber is represented by black dots in the schematic of Fig. 1.1(a). The reactant is therefore preheated by the energy which is rejected from the photoabsorbers.

The motivation for this integrated device – in addition to the aforementioned economic advantage [21] – is an expected increase in efficiency as the rejected heat of the PV cell (energy above the band energy which is converted to heat), see Fig. 1.1(b), is utilized for preheating of the reactant. In the case where a heat-driven, self-tracking concentrator is used [32], the radiation with longer wavelengths (above the smallest band gap of the solar cell materials) can additionally be utilized for the tracking of the concentrator (as detailed in the chapter's section 1.3.5), further increasing the system efficiency.

a)

b)
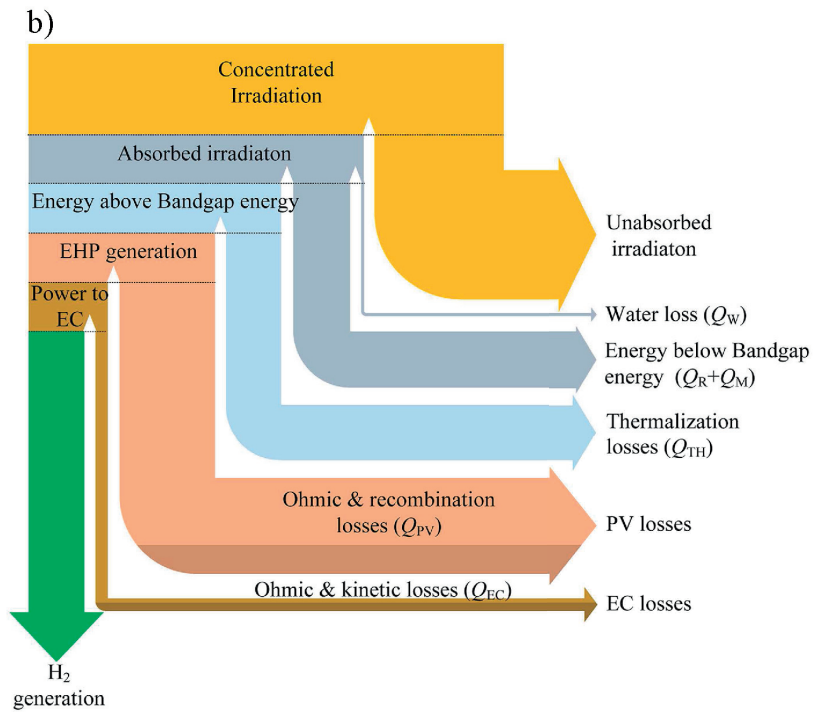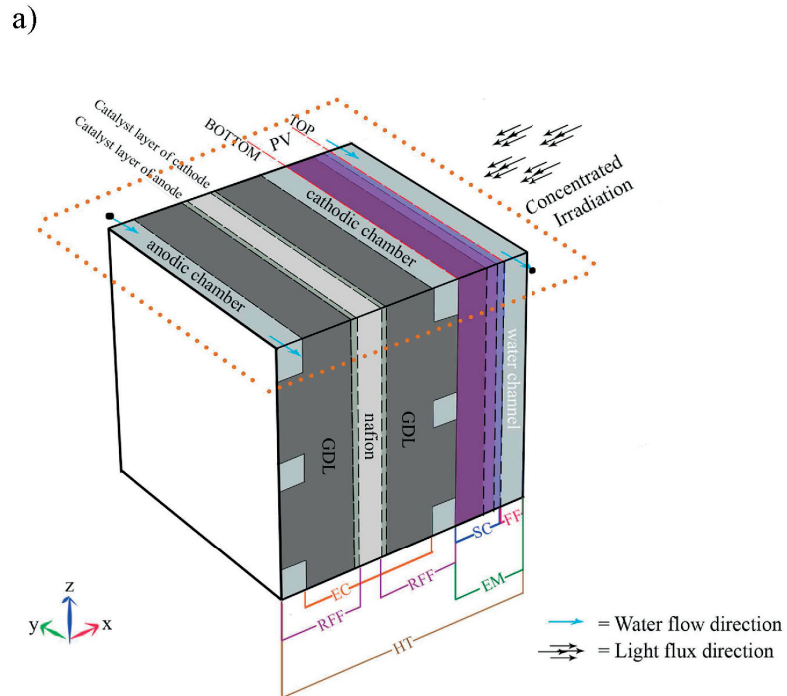
Fig. 1.1 (a) 3D schematic (not to scale) of the integrated PEC device depicting the incoming concentrated irradiation, cooling and preheating water channel, triple-junction solar cell (violet colors), and integrated electrolyzer consisting of anodic and cathodic channels, gas diffusion layers (GDL), catalyst layers, and polymeric electrolyte (Nafion). The 2D simulation domain in the xy-plane is indicated by the dashed orange rectangle. Electromagnetic wave propagation (EM), semiconductor charge transport (SC), heat transfer (HT), fluid flow and reacting fluid flow (FF, RFF), and electrochemical charge transport (EC) simulation domains are represented by their respective color labels in the schematic. (b) The energy re-partition diagram shows the distribution of energy at various stages of its utilization for $C = 18$. The width of the arrows shows approximate re-partitioning for the device utilizing a III-V based solar cell. The darkened areas of the arrows of the PV and EC losses are not considered in the total heat source of the energy equation, as discussed in section 1.3.2.

A 2D multi-physics model of the IPEC device is developed by customizing the combination of a commercial finite element/volume solver [33] and an open source finite difference Newton Raphson solver [34], coupling local mass and heat transfers for the electrochemical component of the device to the detailed multi-physics model of the photoabsorber. The simulation domain consisted of the xy-plane as depicted in Fig. 1.1(a). The model supports the development of design and operational guidelines to maximize hydrogen production, energetic efficiency, and device durability, and to minimize size and cost.

Governing equations and methodology

1.2.1 Electromagnetic wave propagation (EM) The combined form, Eq. (1.3), of Maxwell curl equations (1.1) and (1.2) [35], is solved using the MUltifrontal Massively Parallel Sparse direct Solver (MUMPS) [33] via the finite element method. The electrical field vector, **E**, and the magnetic field vector, **H**, are solved for a finite number of wavelengths spanning the entire spectral range of the incoming solar irradiation.

$$\frac{\partial}{\partial t}\mathbf{B}_\lambda(r,t) = -\nabla \times \mathbf{E}_\lambda(r,t) \tag{1.1}$$

$$\frac{\partial}{\partial t}\mathbf{D}_\lambda(r,t) = \nabla \times \mathbf{H}_\lambda(r,t) - \mathbf{J}_\lambda(r,t) \tag{1.2}$$

$$\nabla \times \mu_r^{-1}(\nabla \times \mathbf{E}_\lambda) - k_0^2(\varepsilon_r - \frac{j\sigma}{\omega\varepsilon_0})\mathbf{E}_\lambda = 0 \tag{1.3}$$

The real parts of the calculated electric and magnetic vector fields, $\Re(\mathbf{E}_\lambda)$ and $\Re(\mathbf{H}_\lambda)$, are used to calculate the time-averaged Poynting vector [35], $\mathbf{S}_{av\lambda}$, Eq. (1.4), and the corresponding optical generation rate, $G_{opt\lambda}$, in the semiconductor region, Eq. (1.5),

$$\mathbf{S}_{av_\lambda} = \frac{1}{2}\Re(\mathbf{E}_\lambda \times \mathbf{H}_\lambda), \tag{1.4}$$

$$G_{opt_\lambda} = \eta_{opt}\frac{-\nabla \cdot \mathbf{S}_{av_\lambda}}{h\nu}. \tag{1.5}$$

However, instead of the divergence calculation, the numerically stable equivalent $G_{opt_\lambda} = \eta_{opt}\dfrac{\frac{1}{2}2\pi\nu|\mathbf{E}_\lambda|^2\Im\{\varepsilon_\lambda\}}{h\nu}$ is used to calculate the generation rate for each wavelength where $\Im\{\varepsilon_\lambda\}$ represents the imaginary part of the complex permittivity of the material for the respective wavelength.

The optical quantum yield, η_{opt}, is assumed to be 1 for photons with energies larger than the band gap of the material and zero for less energetic photons. The wavelength dependence of η_{opt} is different for each of the three (two) semiconductors of the triple (dual) junctions of the solar cell and is determined by their respective band gaps. The overall generation rate, G_{opt}, is the sum of all the individual wavelengths' generation rate, $\sum_\lambda G_{opt_\lambda}$. The boundary conditions (BCs) for Eq. (1.3) are depicted in Fig. 1.2(a), consisting of irradiation flux BC on the top, and absorbing BC at the bottom of the simulation domain. The EM simulation domain consists of the water channel and PV regions for the IPEC device, as it is assumed

that the light doesn't penetrate into the electrochemical cell (EC). The irradiation flux at the top boundary of the device is provided by the concentrator's output, which is equal to $C \cdot I_{in}$, where C is the effective concentration ratio and I_{in} is the solar intensity equal to the AM 1.5G solar spectrum with a flux of 1000 W/m². Floquet periodicity is used to account for the realistic propagation of the plane wave.

Out of the total solar energy incident on the PV, part is absorbed according to the material's complex refractive index and the remainder, which is not absorbed, is lost. The absorbed energy comprises of two parts: one part due to photons above the bandgap energy ($E_a > E_g$), and the other part due to
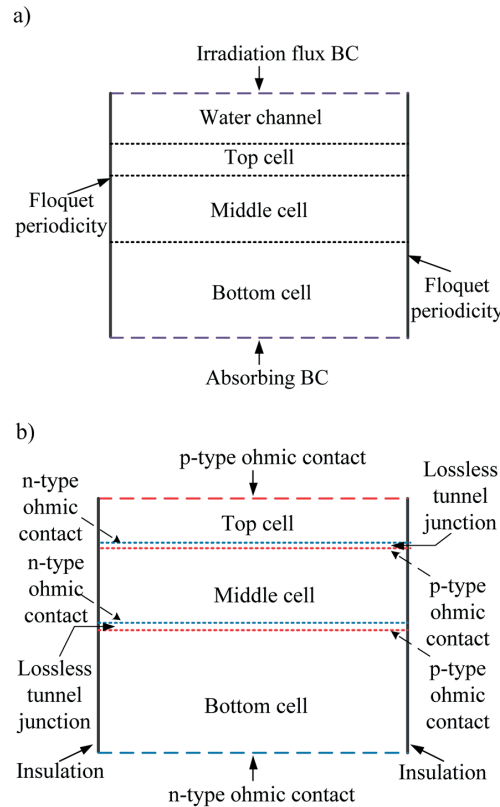
Fig. 1.2 Schematic of the 2D computational domain (not to scale), indicating the boundary conditions for the solution of (a) the coupled Maxwell equations (Eq. (1.3)) in the PV and water channel domain (*xy*-plane), and (b) the charge generation and transfer equations (Eqs. (1.9) – (1.11)) in the semiconductor domain (*xy*-plane).

photons below the bandgap energy ($E_b < E_g$). It should be noted that photons with energies below the bandgap energy of the semiconductor can be absorbed according to the extinction coefficient of the material. However, these absorbed photons won't contribute to the EHP generation and instead result in lattice perturbations which contribute to the heating of the material as described by Q_R and Q_M, discussed below. Out of E_a, one part leads to EHP generation (i.e. equal to $E_a(E_g/hv)$ for each photon) and the other part (i.e. $E_a(1- E_g/hv)$) comprises of the energy lost due to thermalization of photoexcited electrons and holes.

Two fractions are defined, $f_{EHP} = E_g/hv$ and $f_{TH} = (1- f_{EHP})$, such that $f_{EHP}(-\nabla \cdot \mathbf{S}_{av\lambda})$ gives the optical generation rate when divided by respective E_g, consistent with the calculations in Eq. (1.5), and $f_{TH}(-\nabla \cdot \mathbf{S}_{av\lambda})$ gives the heat dissipation density due to the thermalization process (Q_{TH}).

Accordingly, the net heat source term coming from EM wave propagation is defined to be the sum of the individual source and sink terms:

$$Q_{EM_\lambda}^{PV} = Q_{TH}\Big|^{\lambda < hc/E_g} + Q_R\Big|^{\lambda > hc/E_g} + Q_M\Big|^{\lambda > hc/E_g} \tag{1.6}$$

Q_R is the electrical (resistive) loss, and Q_M is the magnetic loss, given by:

$$Q_R = \frac{1}{2}(\Re(J_x \cdot E_x) + \Re(J_y \cdot E_y) + \Re(J_z \cdot E_z)), \tag{1.7}$$

$$Q_M = \Re(\frac{1}{2}i\omega((B_x \cdot H_x^*) + (B_y \cdot H_y^*) + (B_z \cdot H_z^*))), \tag{1.8}$$

where $\mathbf{J} = \sigma\mathbf{E}$ and $\mathbf{B} = \mu\mathbf{H}$. For simulation domains not involving semiconductors, the net heat source is simply $Q_{EM\lambda} = Q_{R\lambda} + Q_{M\lambda}$. The overall Q_{EM} is calculated by summing the individual wavelengths' net heat source terms.

The data of the complex refractive index for $Ga_{0.51}In_{0.49}P$ is from Schubert et al. [36], and data for water and GaAs from Palik [37]. The optical constants for various layers of the aSi-ucSi-ucSi triple junction solar cell were adopted from Collins et al. [38]. The spectrally resolved data has been plotted in Fig. 1.5.

1.2.2 Semiconductor charge transport (SC) The Poisson equation, Eq. (1.9), and current conservation equations, Eqs. (1.10) and (1.11), are solved simultaneously, incorporating the definitions of both the electron current density vector, $\mathbf{J_n}$, and the hole current density vector, $\mathbf{J_p}$, from Eqs. (1.12) and (1.13), respectively [39].

$$\nabla \cdot \left(\varepsilon_s \nabla V \right) = -q(p - n + N_D^+ - N_A^-) \tag{1.9}$$

$$\nabla \cdot \mathbf{J_n} = q\left(R - G \right) + q\frac{\partial n}{\partial t} \tag{1.10}$$

$$-\nabla \cdot \mathbf{J_p} = q\left(R - G \right) + q\frac{\partial p}{\partial t} \tag{1.11}$$

ε_s is the static electric permittivity, q is the electronic charge, and N_D^+, N_A^- are the concentrations of ionized donors and acceptors, respectively. R and G are the carrier recombination and optical generation rates (Eq. (1.5)) [40].

$$\mathbf{J_n} = n\mu_n \nabla E_c + \mu_n k_B TM(n / N_c)\nabla n + \frac{nq}{T} D_{n.th} \nabla T \tag{1.12}$$

$$\mathbf{J_p} = p\mu_p \nabla E_v - \mu_p k_B TM(p / N_v)\nabla p - \frac{pq}{T} D_{p.th} \nabla T \tag{1.13}$$

In Eqs. (1.12) and (1.13), n and p are the free electron and free hole densities, ∇E_c and ∇E_v are the gradients of the local conduction and valence band energies, T is the lattice temperature, μ_n and μ_p are the electron and hole mobilities, and $D_{n.th}$ and $D_{p.th}$ are the thermal diffusion coefficients. The function $M(a)=a/(F_{-1/2}(F_{1/2}^{-1}(a)))$ with $F_{-1/2}$ as the Fermi-Dirac integral. The total current, and thus its variation with voltage, is obtained from the sum of the hole and electron current densities. The recombination term in the current conservation equations considers Shockley-Read-Hall, Auger, and direct recombination phenomena. Temperature independent and temperature dependent baseline parameters are presented in Table 1.1 and section 1.2.7.

The existence of continuous density of states (DOS) in the band gap of aSi:H/ucSi:H, with no well-defined conduction band (CB) and valence band (VB) edges, is due to the spatial disorders in its atomic structure. The localized states in the mobility gap of aSi:H are represented by the CB and VB tail states and the defect states. These states strongly influence the trapping and recombination phenomena [41]. The Urbach tails and defect states in amorphous/microcrystalline semiconductors have been incorporated using wxAMPS [34], and the underlying physics and methodology are discussed in the following discussion.

Table 1.1 Temperature independent reference case parameters used in the simulations.

Parameter name	Parameter value	Unit
No. of wavelengths for EM simulation	150	-
Integrated PEC system width-y direction	1	cm
Diameter of water channel on top of PV	0.2	mm
Thickness of top aSi layer	130*	nm
Thickness of middle ucSi layer	1.86*	μm
Thickness of bottom ucSi layer	4.5*	μm
Thickness of top $Ga_{0.51}In_{0.49}P$ layer	280*	nm
Thickness of bottom GaAs layer	1.5*	μm
Diameter of Anodic and Cathodic channels of EC	0.2	mm
Thickness of GDL	400	μm
Thickness of catalyst layer	100	nm
Active specific surface area	10000	1/m
Thickness of Nafion/membrane	50.8	μm
Current density of EC @1.82V	1.285	A/cm^2
Anodic exchange current density of IrO$_2$ [42]–[44]	$4.62 \times \exp(-48600/\bar{R}T)$	A/cm^2
Cathodic exchange current density of Pt [45], [46]	$142.02 \times \exp(-28900/\bar{R}T)$	A/cm^2

This value is used unless otherwise specified. Here, there are two material choices for PV- 1: a thin film triple junction aSi-ucSi-ucSi, and 2: a III-V based dual junction $Ga_{0.51}In_{0.49}P$-GaAs cell. The reference case I refers to material choice 1 and case II refers to material choice 2. The optical thicknesses for these cells are examples which were not optimized.

The internal heat source term coming from ohmic losses and net recombination losses in the semiconductor is given by [47]

$$Q_{PV} = \mathbf{J} \cdot \nabla V + (E_g + 3k_B T)U , \qquad (1.14)$$

where U is the net recombination. Fermi-Dirac statistics and finite volume solvers [33] are used to solve Eqs. (1.9) to (1.11). The BCs for Eqs. (1.9) to (1.11) are depicted in Fig. 1.2(b). They describe the different ohmic contacts used for each part of the PV. Each p-n junction is simulated separately and then the overall PV's

current-voltage characteristic is generated assuming series connection of these two or three p-n junctions. The tunnel diode connecting the two p-n junctions is not modeled, assuming that it has negligible optical and resistive losses. This assumption is justified by an experimental measurement (which includes all existing resistances) of the 1 cm^2 InGaP/InGaAs solar cells fabricated by CESI S.p.A. Italy, using a Pasan BV-81 AM1.5D concentration cell tester at 25°C and 500 kW/m^2. The measured FF at $C = 500$ was 0.86 and the solar-to-electricity efficiency was 33.7%, showing that the optimized cells exhibited minimal losses even at high concentrations.

Modeling of the amorphous/microcrystalline thin film silicon solar cell- For aSi:H/ucSi:H, the density of states (DOS) exists in between the bandgap region (due to its amorphous nature), which is not the case for crystalline semiconductors, and these special DOS needs an adaptation of the modeling.

The physics of charge transport in amorphous/microcrystalline thin film silicon solar cells is captured by three governing equations namely: a) Poisson's equation (Eq. (1.9)), b) the continuity equation for free electrons (Eq. (1.10)), and c) the continuity equation for free holes (Eq. (1.11)) and appropriate boundary conditions. In Eq. (1.9), n and p are the free electron and free hole densities; and N_D^+, N_A^- are the concentrations of ionized donors and acceptors, respectively. For semiconductors having disorders and defects, Eq. (1.9) is updated:

$$\nabla \cdot \left(\varepsilon_s \nabla V\right) = -q(p - n + N_D^+ - N_A^- + p_d - n_d) \qquad (1.15)$$

where n_d is the total number density of charged acceptor-like sites (or simply trapped electron density) and p_d is the total number density of charged donor-like sites (or simply trapped hole density) in the gap states due to defects and disorders. For materials with disorders, the entire semiconductor simulation procedure is conducted in the same way as described previously in the section- Semiconductor charge transport, but with this updated Poisson's equation (i.e Eq. (1.15)).

The trapped hole/electron density can be due to discrete, banded, or continuous defect states and p_d or n_d is the sum of all these defects. Using the density of states model, the number of trapped holes per volume, p_{d_c}, in continuous donor-like defect states is given by

$$p_{d_c} = \int_{E_v}^{E_c} G_D(E) f(E) dE \qquad (1.16)$$

where $G_D(E)$ is the distribution function or density of states per unit energy per unit volume of donor like states with the energy E in the gap; and $f(E)$ is the Fermi function. Similarly, the trapped electron density is defined as

$$n_{d_c} = \int_{E_v}^{E_c} G_A(E) f(E) dE \tag{1.17}$$

where $G_A(E)$ is the distribution function or density of states per unit energy per unit volume of acceptor-like states. These donor (acceptor)-like Urbach tail states resulting from the valence (conduction) band are modeled using exponential functions (Eq. 1.18), and other defect states are modeled using Gaussian distributions. [48]

$$G_D(E) = G_{DO} \exp(-\frac{E - E_V}{E_D}) \qquad G_A(E) = G_{AO} \exp(\frac{E - E_C}{E_A}) \tag{1.18}$$

E_A and E_D are the characteristic energies (these energies establish the slopes of their respective tails). Capture-cross sections for these tails are to be specified for electron capture and for hole capture (i.e. because these states can exchange carriers with the valence and conduction bands). The values of E_A and E_D, capture cross sections, pre-factors G_{AO} and G_{DO} (states per volume per energy) along with other modeling parameters for aSi-ucSi-ucSi triple junction thin film solar cell are described in Table 1.2.

To reduce the complexity of the model discussed earlier, without compromising the detailed physical treatment, the Eqs. 1.15-1.18 are solved using wxAMPS [34] and the recombination profile (at varying operating voltages) resulting from all these defect states is exchanged with the main semiconductor model of the section- Semiconductor charge transport, which treats the defect states' recombination profile as an additional input.

1.2.3 Electrolyser charge transport (EC) and reacting fluid flow (RFF) Charge transport in the electrode and electrolyte (subscript k = l for the ionic conductor and s for the electronic conductor) is given by [49]:

$$\nabla \cdot \mathbf{J}_k = Q_k, \tag{1.19}$$

$$\mathbf{J}_s = -\sigma_s \nabla \phi_s \text{ and } \mathbf{J}_1 = F \sum_{i=1}^{n_s} z_i (-D_i \nabla c_i - z_i u_{m,i} F c_i \nabla \phi_1), \tag{1.20}$$

obeying electro-neutrality, $\sum_i z_i c_i = 0$. The electrochemical reaction at the electrode-electrolyte interface is accounted for via the reaction current, i_{loc}, modeled via the Butler-Volmer expression [49],

$$i_{loc,m} = i_{0,m}(C_R \exp(\frac{\alpha_{a,m}F\eta_m}{\bar{R}T}) - C_O \exp(\frac{-\alpha_{c,m}F\eta_m}{\bar{R}T})) , \qquad (1.21)$$

where η_m is the total overpotential for reaction m at the electrode-electrolyte interface given by

$$\eta_m = \phi_s - \phi_l - E_{eq.m} , \qquad (1.22)$$

for $m = 1,2$, accounting for the anodic one-step oxygen evolution reaction (OER),

$$2H_2O \rightarrow O_2 + 4H^+ + 4e^- , \qquad (1.23)$$

and cathodic one-step hydrogen evolution reaction (HER),

$$4H^+ + 4e^- \rightarrow 2H_2 . \qquad (1.24)$$

The charge conservation equations, Eqs. (1.19) and (1.20), are solved via finite element methods and a MUMPS solver [33]. The corresponding boundary conditions are: a positive electric potential applied to the anode side, a cathode maintained at zero potential, and insulated sidewalls of the simulation domain. The fluid flow and mass transport in the channels and the porous gas diffusion layers (GDLs) are modeled by the Navier-Stokes equation (Eq. (1.25)) with Darcy extension, [50], [51]

$$\frac{\rho}{\varepsilon_p}(\mathbf{u} \cdot \nabla)\frac{\mathbf{u}}{\varepsilon_p} = \nabla \cdot [-P \cdot I_d + \frac{\mu_d}{\varepsilon_p}(\nabla\mathbf{u} + (\nabla\mathbf{u})^T) - \frac{2}{3}\frac{\mu_d}{\varepsilon_p}(\nabla \cdot \mathbf{u})I_d] - (\frac{\mu_d}{\kappa_p} + \frac{\mathbf{Q_{br}}}{\varepsilon_p^2})\mathbf{u} + \mathbf{F} ,$$
$$(1.25)$$

where ε_p is porosity (refer to list of symbols for nomenclature) and species transport (Eq. (1.26)) is modeled by the Maxwell-Stefan diffusion model [52] for a low-density fluid mixture, with the diffusivities replaced by the binary diffusivities for the existing species pairs,

$$\rho\frac{\partial}{\partial t}(\omega_i) + \rho(\mathbf{u}\cdot\nabla)\omega_i = -\nabla\cdot\mathbf{j}_i + R_i, \qquad (1.26)$$

where ω_i is the mass fraction and $\mathbf{j}_i$ is the mass flux vector relative to the mass average velocity vector $\mathbf{u}$ given by [53]

$$\mathbf{j}_i = -\rho\omega_i\sum_k D_{ik}\mathbf{d}_k - D_i^T\frac{\nabla T}{T}. \qquad (1.27)$$

R_i is the rate expression describing production or consumption, D_i^T are the thermal diffusion coefficients, $\mathbf{d}_k$ is the diffusional driving force acting on species k, and D_{ik} are the multicomponent Fick diffusivities. Argon is incorporated as the sweeping gas for both anodic and cathodic chambers. The binary diffusivities and effective thermal conductivity, density, and specific heat capacities in each chamber vary with temperature as detailed in section 1.2.7.

The species transport equation, Eq. (1.26), is solved using a MUMPS solver [33] via finite element methods. BCs for Eq. (1,26) are depicted in Fig. 1.3(a), describing the inlet and outlet conditions of the different channels. The water at the output of the water channel is fed to the anodic channel at its inlet with normal velocity, v_{water}.

1.2.4 Heat Transfer (HT) The steady-state energy conservation equation [54],

$$\rho C_{\text{p}}\mathbf{u}\cdot\nabla T = \nabla\cdot(k_{\text{th}}\nabla T) + Q, \qquad (1.28)$$

is solved in order to calculate the temperature field in the PEC device. Finite element methods and a PARDISO solver [33] are used for its solution. $Q_{\text{H}} = Q_{\text{EM}} + Q_{\text{PV}} + Q_{\text{EC}}$ describes the heat source for the integrated PEC which includes the heat from electromagnetic heating (Eqs. (1.6)-(1.8)), semiconductor transport (Eq. (1.14)), and solid/liquid-phase charge transport and electrochemical reactions [49], Eq. (1.29):

$$Q_{\text{EC}} = -J_{\text{s}}\cdot\nabla\phi_{\text{s}} - J_{\text{l}}\cdot\nabla\phi_{\text{l}} + (\phi_{\text{s}} - \phi_{\text{l}} - E_{\text{eq}} + T\frac{\partial E_{\text{eq}}}{\partial T})i_{\text{loc}}. \qquad (1.29)$$

The velocity vector, $\mathbf{u}$, is zero for the solid components. The SC (section 1.2.2) and EC (section 1.2.3) simulations do not explicitly solve for energy conservation but are based on charge and current conservation. This results in the appearance of two heat loss terms, $Q_{\text{PV\_lost}}$ and $Q_{\text{EC\_lost}}$, which are defined as $Q_{\text{i\_lost}} = P_{\text{input,i}} - Q_{\text{i}} - P_{\text{output,i}}$, for i

= PV, EC. The total heat source in the integrated device domain is defined as $Q_{EM}+Q_{PV}+Q_{EC}$. Q_{PV_lost} and Q_{EC_lost} are not considered in the heat source term.
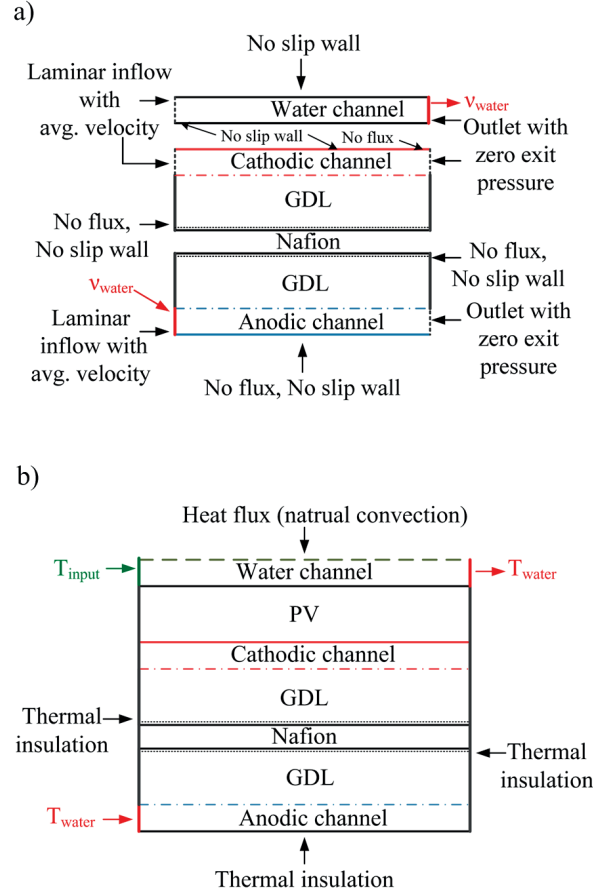
Fig. 1.3 Schematic (xy-plane) (not to scale) showing boundary conditions for (a) fluid flow simulations (both reactive and non-reactive) , and (b) energy conservation (HT) simulations.

For porous media (e.g. GDL), the thermal conductivity, k_{th}, is replaced by an effective conductivity, k_{eff}, accounting for a volume-averaged electrolyte-solid conductivity. The BCs for energy conservation are depicted in Fig. 1.3(b), and consist of thermal insulation on the sidewalls and back side of the simulation domain, and heat flux (natural convection) on the top side. For the PEC device simulation, the concentrator is modeled by a thermal resistance approach [54]. Thus, an effective heat transfer coefficient is used which equals $h_{eff}=(1/h_{coeff}+L_{conc}/k_{conc})^{-1}$,

with L_{conc} representing the mean photon flux length in the concentrator. The temperature-dependent heat transfer coefficient for natural convection at the top of the water channel is calculated using $h_{coeff} = \mathrm{Nu} \cdot k_{air}(T_{film})/\delta$ where Nu is the Nusselt number [55], k_{air} is the temperature-dependent thermal conductivity of the air, and δ is the characteristic length.

1.2.5 Meshing strategy and computational expense Different meshing strategies are adopted for different physical simulation modules in order to minimize the overall solution time of the coupled multi-physics problem and assure mesh independence of the solution. The most restrictive requirement came from the EM simulations (Eq. (1.3)), as minimum element size in the direction of incident radiation had to be at least 1/5 (or 1/10) of the incoming wavelength for second order elements (or first-order elements). Additionally, this minimum element size was adjusted by a factor of $1/n_{ref}$ accounting for the change in the refractive index as light travels from one material to another. A variable meshing approach was used for different wavelengths to minimize the computational time. The solution of the other transport and conservation equations, Eqs. (1.9)-(1.11), (1.19)-(1.22), and (1.28), were similarly optimized in order to allow for mesh convergence and to minimize the computational expense. A distributed mesh with arithmetic sequenced symmetric distribution and with an element ratio of 9 was used in the direction perpendicular to the flow in order to resolve the boundary layer for fluid flow, mass transport, and heat transfer calculations. A dense meshing approach in the catalyst layer of EC and around the junction interfaces in the PV was utilized. The mesh size was increased in the other domains for the solution of Eqs. (1.9)-(1.22) in order to reduce computational time.

A workstation with 128 GB RAM and 12 cores was used to solve the coupled equations. Approximately 15 hours were required (with 150 wavelength bands of ~7 nm and ~41 nm in the above bandgap energy and below bandgap energy spectrum, respectively) to find a converged solution for reference case I (see the following section). Typically, 3 global (blue loop in Fig. 1.4), 3 local (dark red loop in Fig. 1.4), and 20 internal (dotted box in Fig. 1.4) iterations were needed to achieve final convergence. The number of global and local iterations increased with increasing irradiation concentration and with decreasing water mass flow rate, as these parameters significantly influenced the device temperature profile.

1.2.6 Simulation flow Fig. 1.4 is a simulation flow diagram of the coupled model containing six physical modules: EM, HT, FF, RFF, EC, and SC. The flow depicts the simulation flow for the PEC device without the concentrator and takes as input the irradiation spectrum from any concentrator simulation.

The EM simulation is performed for the given temperature field, starting with a constant initial temperature profile (T_{init} = 293 K). The resulting heat dissipation density is input to the heat transfer (HT) simulation module. The fluid flow (FF) module provides the velocity of the water (flowing in the cooling water channel) to the reacting fluid flow (RFF) module and the heat transfer (HT) module. The HT module provides the temperature input to all the other modules. The EC module - being fed by water mass fraction from the RFF module and temperature from the HT module - provides Q_{EC} to HT and i_{loc} to RFF. In parallel, the semiconductor device simulation is performed starting with T_{init} (using the input of the defect/disorder recombination profile, Rec_d, from AMPS). The resulting surface averaged current densities and electric potential from the semiconductor and electrolyzer charge transfer equations are input to the operating point calculation module, which calculates the operating current and voltage decided by the intersection of the PV and EC J-V curves. If the PV temperature distribution, $T_{op}(\mathbf{r})$, at the operating point is not equal to the initial temperature profile of the semiconductor simulation module ($T_{semi}(\mathbf{r})$), a new $T_{op}(\mathbf{r})$ is provided to the corresponding modules (similar for $T_{EM}(\mathbf{r})$) and the loop is repeated. This process is iteratively repeated until the temperature converges ($T_{op,old}(\mathbf{r})$ - $T_{op,new}(\mathbf{r}) < \varepsilon_{rr}$) where ε_{rr} is the tolerable error in temperature, which equals 0.1K in accordance with Eq. (1.30).

The AM 1.5G solar irradiation spectrum was adapted to contain 150 wavelengths ($\Delta\lambda$ = 7-41 nm) between 280 nm – 2500 nm in order to reduce the number of wavelengths simulated but to still capture the spectral variations in the visible and infrared parts of the spectrum. The change in the absorbable spectrum with temperature requires the choice of an adaptive wavelength spectrum for each global iteration step. The minimum wavelength difference for a temperature change from T_1 to T_2 is given by

$$\frac{hc}{E_g(0)-\dfrac{\alpha T_1^2}{T_1+\beta}} - \frac{hc}{E_g(0)-\dfrac{\alpha T_2^2}{T_2+\beta}} = \Delta\lambda_{min}. \tag{1.30}$$
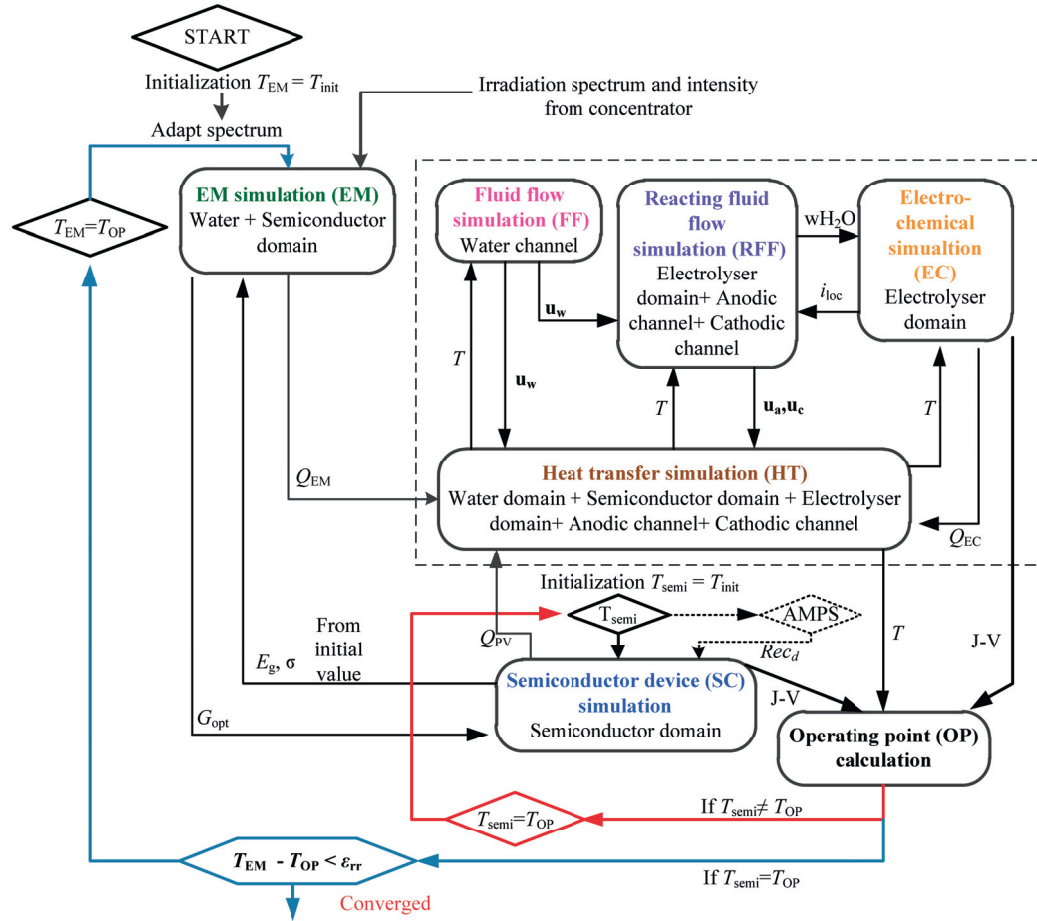
Fig. 1.4 Simulation flow of the integrated PEC system. Arrows show interaction among the subroutines solving for multiple physics and corresponding conservation and transport equations. The interaction with AMPS is only for the cases involving aSi/ucSi based PV.

1.2.7 Reference case The ASTM G173-03 Global tilt Reference Spectra Derived from SMARTS v. 2.9.2, referred to as AM1.5G hereafter, is used. It contains ~2000 wavelengths and has the integrated intensity of 1003 W/m^2. In order to capture the same intensity at a reduced number of input wavelengths (which in turn reduces the computation time), the spectrum is adapted to contain 150 wavelength bands. The intensity of each band's wavelength has been increased by a factor such that the total intensity under the modified spectrum is still 1003 W/m^2.

For the analysis presented in the main script (except section 1.3.5), the input to the PV is assumed to be coming from a concentrator having 100% optical efficiency with AM1.5G. This is done to have a general understanding of effects of the AM1.5G spectrum rather than being limited to a spectrum coming from a particular concentrator.

The temperature dependent baseline parameters used in the simulations are presented herewith. The bandgap (E_g) of $Ga_{0.51}In_{0.49}P$ [56] varies with temperature as

$$E_g = -0.2722x_f^2 + 1.1925x_f + 1.3399 - 0.00066(T - 293) \text{ [eV]}, \quad (1.31)$$

where x_f [57] is 0.51 for $Ga_{0.51}In_{0.49}P$, and E_g of GaAs is given as [58]

$$E_g = 1.519 - \frac{5.41 \times 10^{-4} T^2}{T + 204} \text{ [eV]}, \quad (1.32)$$

with effective density of states varying as $(T/300)^{3/2}N_{v0}$ or $(T/300)^{3/2}N_{c0}$. The various recombination constants for $Ga_{0.51}In_{0.49}P$ depend on E_g which, in turn, depend on temperature. These constants and their variations have been adopted form Haas et al. [57]. The recombination constants and related parameters for GaAs have been incorporated from [59], [60]. E_g of all aSi or ucSi based photoabsorber varies as [58]

$$E_g = E_{g_0} - \frac{4.73 \times 10^{-4} T^2}{T + 636} \text{ [eV]}, \quad (1.33)$$

where E_g is the mobility band gap presented in Table 1.2. The standard equilibrium potential for water electrolysis varies with temperature as [61]

$$E_{eq} = 1.229 - 0.9 \times 10^{-3} \left(T - 298 \right) \text{ [V]}, \quad (1.34)$$

The model incorporates electrical conductivity of Nafion [27], [62] as 22.73×exp(-2000/$\bar{R}T$) [S/m], anodic exchange current density of IrO_2 [42]–[44] as 4.62×exp(-48600/$\bar{R}T$) [A/cm^2], and cathodic exchange current density of Pt [45], [46] as 142.02×exp(-28900/$\bar{R}T$) [A/cm^2]. Thermal conductivity, specific heat capacity at constant pressure and volume, density of H_2O, H_2, O_2, Ar at varying temperature are interpolated from [63], and temperature dependent electrical and thermal conductivity of Pt are used from [64].

The spectrally-resolved complex refractive index ($n_{ref}+ik_{ref}$) of $Ga_{0.51}In_{0.49}P$, GaAs, water, and aSi/ucSi photoabsorber materials is shown in Fig. 1.5. The data for $Ga_{0.51}In_{0.49}P$ is from Schubert et al. [36], data of water and GaAs from Palik [37]; and data of aSi/ucSi from Collins et al. [38]. The parameters for the electrolyzer validation curves presented in Fig. 1.6(b) are given in Table 1.3.
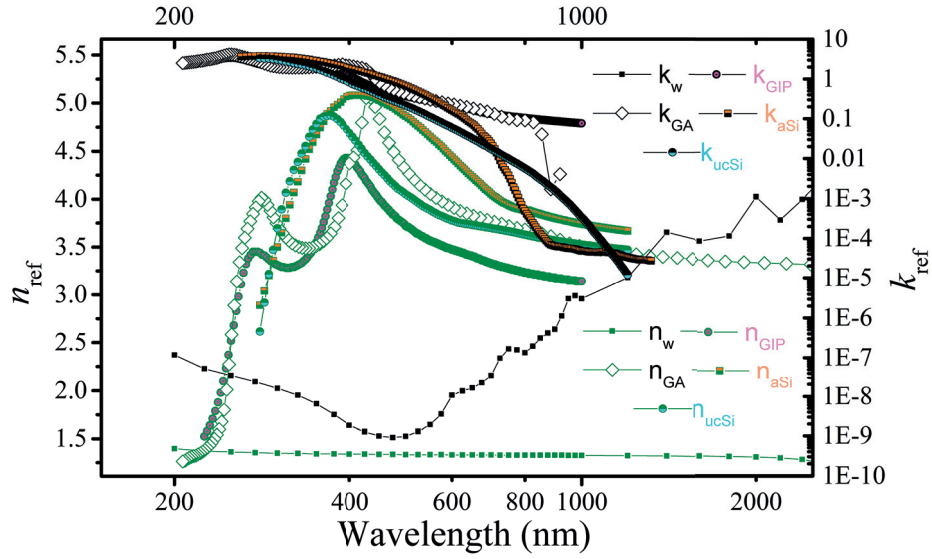
Fig. 1.5 The plot showing real (n_{ref}) and imaginary (k_{ref}) parts of refractive index for water, $Ga_{0.51}In_{0.49}P$, GaAs, aSi and ucSi photoabsorber materials. The green lined curves (n_{ref} values), correspond to the left y-axis and black lined curves (k_{ref} values), correspond to right y-axis.

1: Two Dimensional Non-Isothermal Multi-physics Modeling

Table 1.2 The set of input parameters for the 3 layers of aSi-ucSi-ucSi triple junction thin film solar cell used in electrical simulations.

Parameter name	aSi:H Top cell [65]			ucSi:H middle cell [66]			ucSi:H bottom cell [66]		
	p layer	i layer	n layer	p layer	i layer	n layer	p layer	i layer	n layer
Electrical									
Electron affinity [eV]	3.7	3.8	3.8	4	4	4	4	4	4
Mobility band gap [eV]	1.92	1.82	1.72	1.2	1.4	1.6	1.2	1.4	1.6
Dielectric constant [-]	11.9	11.9	11.9	11.9	11.9	11.9	11.9	11.9	11.9
Effective DOS in CB [cm^{-3}]	2.5×10^{20}	2.5×10^{20}	2.5×10^{20}	2×10^{20}	2×10^{20}	2×10^{20}	2×10^{20}	2×10^{20}	2×10^{20}
Effective DOS in VB [cm^{-3}]	2.5×10^{20}	2.5×10^{20}	2.5×10^{20}	2×10^{20}	2×10^{20}	2×10^{20}	2×10^{20}	2×10^{20}	2×10^{20}
Electron mobility [$cm^2/(V\,s)$]	10	20	20	100	32	20	100	32	20
Hole mobility [$cm^2/(V\,s)$]	1	2	2	25	8	4	25	8	4
Bandtail states									
G_{D0}/G_{A0} [cm^{-3}/eV]	1×10^{21}	1×10^{21}	1×10^{21}	1×10^{21}	4×10^{21}	4×10^{21}	1×10^{21}	4×10^{21}	4×10^{21}
Characteristic energy E_D, E_A [eV]	0.1,0.05	0.05,0.02	0.05,0.02	0.02,0.01	0.02,0.01	0.05,0.03	0.02,0.01	0.02,0.01	0.05,0.03
Capture cross section for donor states, e, h, [cm^2]	10^{-15},10^{-17}	10^{-15},10^{-17}	10^{-15},10^{-17}	2×10^{-14},10^{-15}	10^{-15},10^{-17}	10^{-15},10^{-16}	2×10^{-14}, 10^{-15}	10^{-15},10^{-17}	10^{-15},10^{-16}
Capture cross section for acceptor states, e, h, [cm^2]	10^{-17},10^{-15}	10^{-17},10^{-15}	10^{-17},10^{-15}	10^{-15},2×10^{-14}	10^{-17},10^{-15}	10^{-16},10^{-15}	10^{-15}, 2×10^{-14}	10^{-17},10^{-15}	10^{-16},10^{-15}
Defect states –Gaussian									
Gaussian density of states [cm^{-3}]	10^{16}	5×10^{15}	10^{16}	-	-	-	-	-	-

1: Two Dimensional Non-Isothermal Multi-physics Modeling

Gaussian peak energy [eV] donors, acceptors	1.17,1.27	1.02,1.12	0.87,0.97	-	-	-	-	-
Standard deviation [eV]	0.08	0.08	0.08	-	-	-	-	-
Capture cross section for donor states, e, h, [cm²]	$10^{-14},10^{-15}$	$10^{-14},10^{-15}$	$10^{-14},10^{-15}$	-	-	-	-	-
Capture cross section for acceptor states, e, h, [cm²]	$10^{-15},10^{-14}$	$10^{-14},10^{-15}$	$10^{-14},10^{-15}$	-	-	-	-	-
MidGap states								
"Switch-over energy" [eV] measured positively from VB	-	-	-	0.56	0.56	0.56	0.56	0.56
Density of acceptor-like, donor-like midgap states [cm⁻³/eV]	-	-	-	$10^{15},10^{15}$	$10^{16},10^{15}$	$10^{15},10^{15}$	$10^{16},10^{15}$	$10^{15},10^{15}$
Capture cross section for donor-like midgap states, e, h, [cm²]	-	-	-	$10^{-14},10^{-16}$	$10^{-14},10^{-16}$	$10^{-14},10^{-16}$	$10^{-14},10^{-16}$	$10^{-14},10^{-16}$
Capture cross section for acceptor-like midgap states, e, h, [cm²]	-	-	-	$10^{-16},10^{-14}$	$10^{-16},10^{-14}$	$10^{-16},10^{-14}$	$10^{-16},10^{-14}$	$10^{-16},10^{-14}$

Table 1.3 Parameters utilized for the electrolyzer validation shown in Fig. 1.6(b).

Parameter name	Green curve in Fig. 1.6(b)	Black curve in Fig. 1.6(b)	Unit
Thickness of Anodic & Cathodic channels of EC	0.2	0.2	mm
Thickness of GDL	400	400	μm
Thickness of catalyst layer	40	30	nm
Thickness of Nafion/membrane	125.8	50.8	μm
Anodic exchange current density	$6.4351\cdot10^{-5}$	$2.99\cdot10^{-3}$	A/m^2
Cathodic exchange current density	30.25	75.436	A/m^2
GDL conductivity	111	222	S/m
Catalyst porosity	0.2	0.3	-
GDL porosity	0.5	0.4	-
Cell temperature	323.15	353.15	K
Mean flow velocity at anodic inlet	0.06	0.2	m/s

1.3 Results and discussion

1.3.1 Reference Case and Validation Two reference cases are defined: reference case I with aSi-ucSi-ucSi and p-n-cathodic-anodic configuration, and reference case II with $Ga_{0.51}In_{0.49}P$-GaAs and n-p-anodic-cathodic configuration. The dimensions and component characteristics used for the reference case, with aSi-ucSi-ucSi thin film triple junction ($V_{oc} \sim 2.1V$, $J_{sc} \sim 47 \ A/m^2$, FF $\sim 64\%$) or $Ga_{0.51}In_{0.49}P$-GaAs dual junction ($V_{oc} \sim 2.35V$, $J_{sc} \sim 100 \ A/m^2$, FF $\sim 93\%$) example solar cells, are given in Table 1.1.

The detailed modeling parameters for the aSi-ucSi-ucSi thin film cell and temperature dependent baseline parameters used in the simulations are given in Tables 1.2 and section 1.2.7, respectively. The operating normal mean flow velocity of water in the top cooling channel is 0.2 m/s for both reference cases. The choice of material for these two reference cases was motivated by the techno-economic analysis presented in [21] which highlights that both choices have the potential to achieve low-cost production of hydrogen. The F factor, defined as A_{EC}/A_{PV} [21], is chosen to be 1 in this study. This choice is not optimal from a performance and cost point of view [21] but represents a closely integrated device. The solar to hydrogen efficiency (STH) is calculated using

$$\eta_{STH} = \frac{J_{OP} \cdot E_{eq}^0}{C \cdot I_{in}},$$

(1.35)

assuming Faradaic efficiencies of 1 and negligible product crossover with E_{eq}^0 equal to 1.23 V (equilibrium potential at neutral pH, $T = 298$ K, and atmospheric pressure).

Non-integrated, externally wired concentrated PV and electrolysis devices have experimentally demonstrated efficiencies in the range of 17 to 24% [67]–[69]. Due to the lack of CIPEC device demonstration, the PV and EC components are separately validated. The experimental validation for PV and EC components is presented in Fig. 1.6(a) and (b), respectively. The modeling parameters and operating conditions were chosen to be similar to those presented in other studies [61], [70]–[72]. In order to validate the mass transport effects in the EC, a comparison was made with fuel cell (FC) data available from Kim et al. [72] assuming the electrolysis to be a perfectly reversible process of FC. The voltage scale was then adapted using $V_{new} = (E_{eq} - V_{exp}) + E_{eq}$, where V_{exp} is the experimentally measured voltage, V_{new} is the adapted voltage, and E_{eq} is the equilibrium voltage of 1.208 at 353 K, Eq. 1.34. This was due to limited availability of experimental data for current saturation and mass transport effects in PEM electrolyzers. The materials and dimensional parameters used in the EC simulations are detailed in Table 1.3.

The simulated and experimental characteristic curves were in good agreement, i.e. maximal differences in the current of the ECs of 8.6% at a voltage of 1.78 V for the black curve and 12% at a voltage of 1.64 V for the green curve were observed. The FF of PV for the simulated case was 91% compared to the 75% for the experimental case. It should be noted that the PV model didn't take into account the contact resistance (instead an ohmic contact is assumed) and the anti-reflection coating used in Lueck et al. [70], explaining the observed fill factor difference between simulated and experimental curves. This is within the physical feasibility limits, as the maximal FF for a V_{oc} of 2.35 V is approximately 0.94 as reported by Green [73].

a)

b)
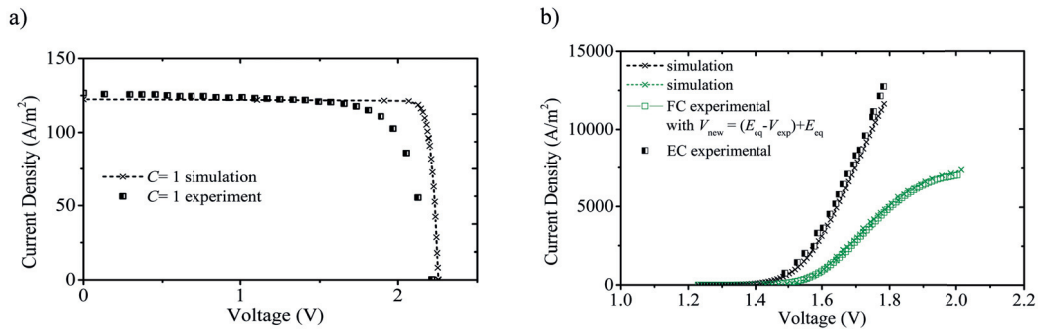
Fig. 1.6 Simulated (crosses) and measured (rectangles) characteristic J-V curves for (a) the Ga$_{0.51}$In$_{0.49}$P-GaAs dual junction solar cell at $C = 1$, and (b) the electrolyzer with Pt/IrO$_2$ at 80°C (black), or the fuel cell with Pt-Pt at 50°C (green) with adapted voltage scale as per $V_{new} = (E_{eq} - V_{exp}) + E_{eq}$. The experimental data in (a) is taken from Lueck et al. [70] and in (b) from Carmo et al. [61], [71] (black) and Kim et al. [72] (green).

1.3.2 Irradiation Concentration Analysis The characteristic J-V curves (see Fig. 1.7) for both reference cases show that the STH efficiency, η_{STH}, decreases with increasing irradiation concentration. J_{sc} increases linearly with C. V_{oc} is influenced by the combined effect of increasing temperature and increasing J_{sc}, resulting in its logarithmic increase with increasing C. FF of the Si based PV (~64%) is significantly lower than that of the III-V based PV (~93%) at $C = 1$. The fill factor for both cases decreases (~4% for reference case I, ~1% for reference case II) when increasing C from 1 to 1000. J_{op}, and hence $\dot{M}_{H_2}$ (signifying the rate of hydrogen production in g/min/m^2 and calculated by Faraday's law of electrolysis), increases with increasing C, but at a decreasing rate for larger C. PV and EC average temperatures (i.e. T_{PV} and T_{EC}) increase with C, and consequently the activation overpotentials for the EC

decrease with C. These trends for η_{STH}, T_{PV}, and T_{EC} are shown in Figs. 1.7(c)-(d) for Si and III-V PV based devices.
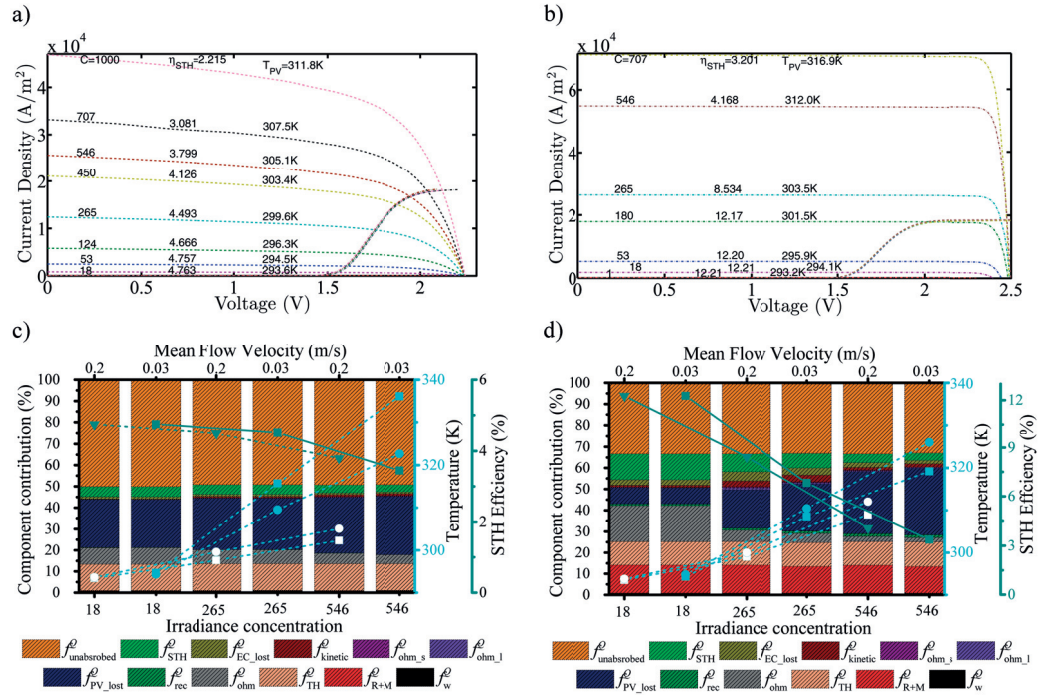
Fig. 1.7 Characteristic J-V curves for (a) the thin film triple junction aSi-ucSi-ucSi, and (b) the $Ga_{0.51}In_{0.49}P$-GaAs dual junction based integrated PEC device, for varying irradiation concentration. The temperature of the PV is averaged over the PV volume. The EC J-V curves have the same color as the corresponding PV curves but are overlapping due to their limited sensitivity to C. The water mean flow velocity is 0.2 m/s. The various heat source contributions for (c) the thin film triple junction aSi-ucSi-ucSi, and (d) the $Ga_{0.51}In_{0.49}P$-GaAs dual junction based device, for varying irradiation concentration and varying mean flow velocity. The STH efficiency decreases and PV/EC temperature increases with increasing C for both cases. Rectangles describe the EC temperature, circles the PV temperature.

The optimal irradiation concentration for the III-V material based case is around $C_{opt} = 180$. Higher concentrations lead to current saturation in the EC and a further increase in C doesn't benefit J_{op}. For the Si case, the optimal concentration is around $C_{opt} = 707$. For both reference cases, the STH efficiency decreases when increasing C from 1 to C_{opt}. For the III-V based PV cell this decrease is 0.3% while for the Si

based PV cell this decrease is ~38%. This behavior is due to the relatively low FF of the Si based case. Generally, for devices using low FF PVs, PV and EC are limiting for operation under high irradiation concentration. For devices using large FF PVs, the EC's saturation current is the limiting factor.

The heat source contribution ($\mathcal{f}_i = Q_i/\Sigma Q_i = Q_i/P_{input}$) for various sources including: absorption losses in the water channel (Q_w), EM resistive and magnetic losses (Q_{R+M}), thermalization losses (Q_{TH}), PV ohmic losses (Q_{ohm}), PV recombination losses (Q_{rec}), EC ohmic losses in electrolyte (Q_{ohm_l}) and electrodes (Q_{ohm_s}), and EC kinetic losses ($Q_{kinetic}$), are plotted in Figs. 1.7(c) and (d) for Si and III-V based cases respectively. $Q_{unabsorbed}$, Q_{PV_lost}, and Q_{EC_lost} are closing the energy balance. The total heat source in the integrated domain comes from $\mathcal{f}_{EM}$ ($\mathcal{f}_w + \mathcal{f}_{R+M} + \mathcal{f}_{TH}$), $\mathcal{f}_{EC}$ ($\mathcal{f}_{ohm\_l} + \mathcal{f}_{ohm\_s} + \mathcal{f}_{kinetic}$) and $\mathcal{f}_{PV}$ ($\mathcal{f}_{ohm} + \mathcal{f}_{rec}$). For the Si based device, the $\mathcal{f}_{EM}$ and $\mathcal{f}_{EC}$ increases with increasing C while $\mathcal{f}_{PV}$ decreases. For III-V material based device, the same trend is followed for $\mathcal{f}_{EM}$ and $\mathcal{f}_{PV}$, but $\mathcal{f}_{EC}$ initially increases up to $C = 265$ and then decreases. This $\mathcal{f}_{EC}$ trend is the result of the C_{opt} being 180 for the III-V based case, because after $C = 180$ the operating current is not increasing, resulting in a smaller relative contribution of Q_{EC}. The $\mathcal{f}_{R+M}$ is higher for reference case II because of the refractive index of the materials used which have significant absorption below the bandgap wavelength.

The sum of $Q_{EM} + Q_{PV} + Q_{EC}$ is higher (1.5-2 times) for the III-V based case than the Si one for the choice of design parameters presented in Table 1.1. Despite this, the T_{PV} and T_{EC} were observed to be less than or comparable to reference case I. This implies that the n-p-anodic-cathodic configuration, used in reference case II, provides better cooling. This results from the direct feed of the water from the cooling channel above the n-side of the PV to the anodic channel lying between the p-side of the PV and the EC's anode, making the location central within the major heat sources in the device, resulting in better heat removal. Figs. 1.7(c)-(d) also present $\mathcal{f}_i$ for a lower mean flow velocity (0.03 m/s), implying that lower mass flow rates are less effective in heat removal, leading to higher device temperatures. The parasitic absorption in the top water channel is found to be minimal (see Figs. 1.7(c)-(d)) and is in accordance with the findings reported by Döscher et al. [74] for a water channels of thickness of 0.2 mm with overpotentials in the range observed in our device.

1.3.3 Sensitivity analysis with material and dimensional parameters The characteristic operating curves for EC and PV for reference case I, for the variation of parameters including exchange current density, membrane thickness, as well as catalyst and GDL thicknesses, are presented in Fig. 1.8. Only one parameter is varied

at a time, holding all others at the reference case values. The intersection of the EC and PV curves represent the operating point of the integrated PEC device.

Table 1.4 STH efficiency and operating current density (of reference case I) for parametric studies shown in Fig. 1.8 at $C = 450$.

Parameter name	STH efficiency η_{STH} [%]	Percentage change in η_{STH} from a to c or a to d	Operating current density [kA/m^2]
Exchange current density multiplier		+9.7 %	
a. 1	4.12		15.09
b. 5	4.29		15.68
c. 50	4.48		16.38
d. 1000	4.52		16.53
Membrane thickness [μm]		-28 %	
a. 30	4.38		16.02
b. 50.8	4.13		15.09
c. 80	3.15		11.53
Catalyst thickness [nm]		+4 %	
a. 50	4.04		14.79
b. 100	4.13		15.09
c. 150	4.18		15.23
d. 200	4.21		15.40
GDL thickness [μm]		-4 %	
a. 300	4.16		15.21
b. 400	4.13		15.09
c. 800	3.99		14.57

The operating current density and the STH efficiency, shown in Table 1.4, increases with increasing exchange current density and catalyst thickness (leading to improved EC kinetics), Figs. 1.8(a)-(c). STH efficiency decreases with increasing membrane and GDL thickness as visible in Figs. 1.8(b)-(d). Increasing the membrane thickness results in increased mass transport limitations in the EC. The coupled model allows a temperature maintenance in the range of ~300 K for all parameter variations, even at $C = 450$. A water inlet mean flow velocity of 0.2 m/s was found be sufficient in

effectively maintaining the device temperature at ~300 K, signifying the importance of thermal management, which is solely possible due to the integrated nature of the device.
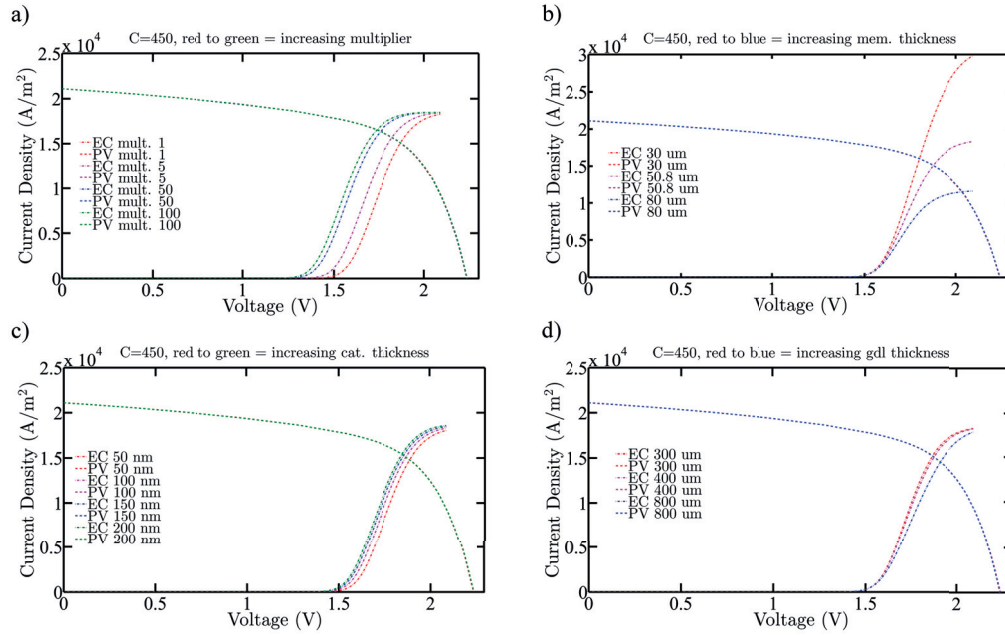
Fig. 1.8 Characteristic curves for EC and PV showing operating points for changing: (a) exchange current density multiplier, (b) Nafion membrane thickness, (c) catalyst layer thickness, and (d) GDL thickness at an irradiation concentration of 450 for reference case I, i.e. the thin film Si based PEC device.

1.3.4 Two-dimensional results The 2D modeling for the various physics involved allowed for the generation of an in-depth knowledge of the spatial variation of various physical parameters in the device. This 2D treatment is important because various physical phenomena have orthogonal main directions to one another, for example: the fluid flow's main direction is along the y-axis, perpendicular to the main direction of the charge transport, and absorption in the PV occurs along the x-direction.

A typical temperature distribution in the EC of the integrated PEC is shown in Figs. 1.9(a)-(b). The EC consists of the anodic and cathodic GDLs, catalyst layers, and Nafion membrane (in middle). The cathodic side operates at a higher temperature than the anodic side. The temperature increases along the positive *y*-direction, the

direction of the fluid flow. This results from the heating of the fluid once it enters the channel and moves towards the positive *y*-direction. The cathodic side shows higher temperatures because it hosts a positive heat source, $Q_{GDL+cat,c} = 2.93 \cdot 10^7$ W/m³, while the anodic side is at lower temperatures as it hosts a negative heat source, $Q_{GDL+cat,a} = -7.50 \cdot 10^6$ W/m³, both for $C = 1000$ and mean flow velocity of 0.2 m/s. The same trend at absolute increased temperatures is observed for lower water flow velocities, as depicted in Fig. 1.9(b).
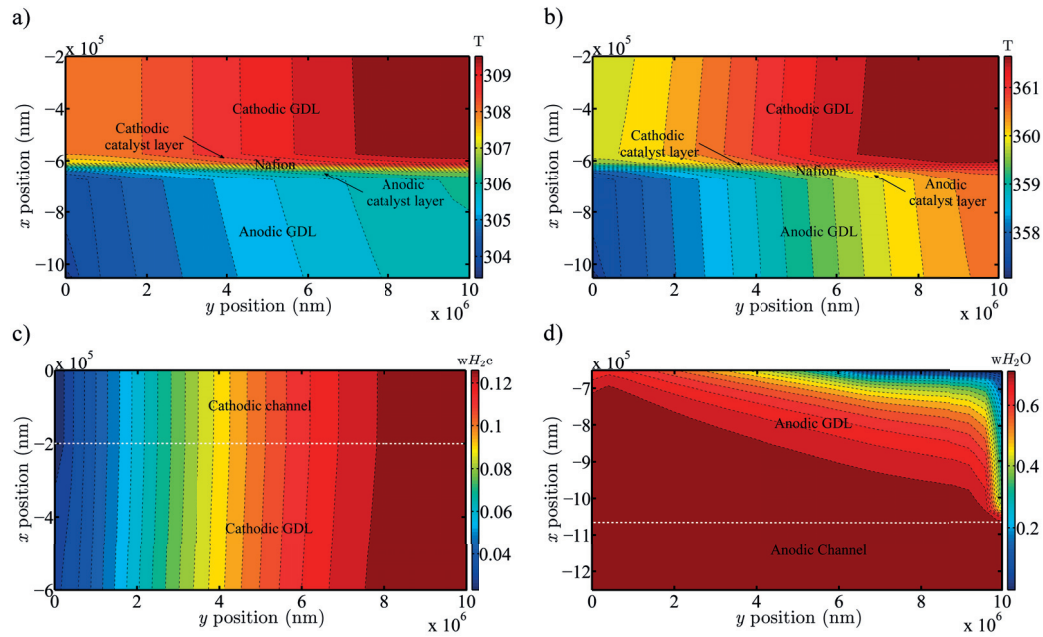
Fig. 1.9 Typical EC temperature profiles for $C = 1000$ and mean flow velocity of (a) 0.2 m/s, and (b) 0.03 m/s. The contour plots show the evolution of (c) the H_2 mass fraction in the cathodic GDL and channel, and (d) the H_2O mass fraction in the anodic GDL and channel, both for $C = 1000$ and mean flow velocity of 0.03 m/s. The GDL layers are 400 μm thick with the catalyst layers 100 nm, the Nafion membrane 50.8 μm and the channels having thicknesses of 200 μm. The inlet corresponds to y position of 0 nm (left) and the outlet is at the position of $y = 1$ cm (right).

The H_2 mass fraction (wH₂c) in the cathodic GDL and channel assembly increases homogenously in the direction of sweep gas flow because the generated H_2 gas has better diffusivity and is swept in the flow direction. The input water diffuses through

the anodic GDL to the catalytic site where it is oxidized. This results in a decrease of H_2O mass fraction (wH_2O) in the anodic GDL and also in the channel in the direction of water flow as shown in Fig. 1.9(d). The ionic flux given by the Nernst-Plank equation decreases in the Nafion membrane from the inlet to outlet, forcing the electrolyte current density to follow the same trend, shown in Fig. 1.10(a). The local current density, given by the concentration-dependent Butler-Volmer equation, is governed by the concentration of H_2O at the anodic side and H^+ ion on the cathodic side, giving rise to the current density profiles shown in Figs. 1.10(c)-(d).

The 2D modeling enables knowledge of the full distribution profile of various physical parameters, which in turn helps in identifying the local maxima and minima. This is beneficial from the perspective of identifying and removing hot spots in the device which may lead to thermal stress and generally affect performance and operational uniformity. The 2D profile of wH_2O shows that the channel length is optimized for the given conditions. Longer channels do not benefit the operation, as the H_2O is fully consumed towards the end of the channel.
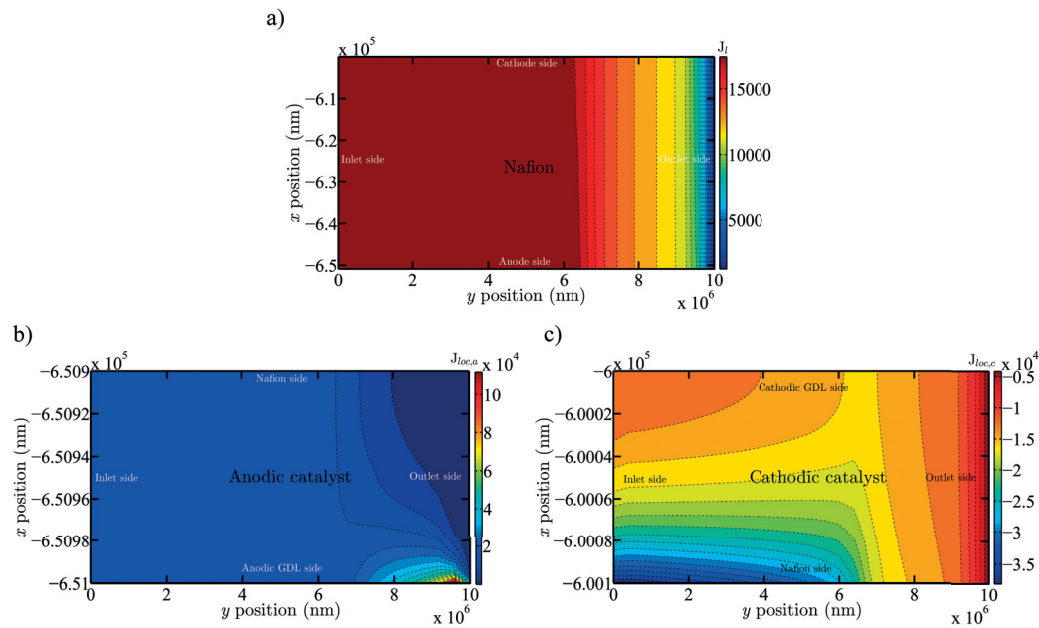
Fig. 1.10 Contour plots showing current density distributions in (a) the electrolyte domain of the electrochemical cell, (b) the anodic catalyst domain, and (c) the cathodic catalyst domain, for $C = 1000$ and mean flow velocity of 0.03 m/s.

Hence, only a simultaneous and corresponding increase of both the channel length and the mean flow velocity would provide additional benefit to the performance.

As illustrated, the correct realization of complex geometries for electromagnetic propagation can only be done with 2D and 3D treatment. 2D modeling provides locally resolved information which is necessary for complete design guidance and optimization of PEC devices.

1.3.5 IPEC with self-tracking concentrator For the case when the self-tracking concentrator, see Fig. 1.11, is also integrated with the rest of the IPEC device, the AM1.5G spectrum is incident on to the lens array of the concentrator assembly. The lens array focusses light through the glass waveguide on the dichroic prism layer which splits the incoming spectrum into the low wavelength part and high wavelength part. The high wavelength part goes to the actuator (hereafter called actuator spectrum) and the low wavelength split part is reflected inside the glass waveguide at angles such that these wavelengths get trapped inside the waveguide due to total internal reflection occurring at the top air-glass interface. The light travels towards the PV i.e. x-direction (assuming the opposite side of the glass waveguide is covered with highly reflecting material). These various spectra for the case with self-tracking concentrator are shown in Fig. 1.12(a), and they show the various losses occurring in the concentrator assembly. Consequently, the green spectrum is the input for the PV when the self-tracking concentrator is used, as opposed to the blue AM1.5G spectrum for a traditional mirror-based concentrator, implying the total optical losses in the self-tracking concentrator amounts to around 29% of the incoming radiation.

The actuator consists of the steel casing with cylindrical holes filled with a phase change material (PCM), which in our design is a paraffin wax with a melting point of ~37.6 °C. It absorbs the infra-red part of the incident spectrum being split by the dichroic prism layer and in turn, the PCM expands vertically so that the other split part i.e. the visible spectrum is reflected in such a way that it gets trapped inside the waveguide and is effectively provided to the PV. The actuating action of the actuator of the self-tracking solar concentrator has been modeled using EM and HT physics. The results of ray-tracing modeling for the lens array and glass waveguide has been taken from [32] and the spectrum coming to the top of a paraffin wax cylinder is the input for our EM model, based on which the heat sources were calculated and the corresponding temperature profile in the wax cylinder was obtained which ultimately provided the wax's thermal expansion, Fig. 1.12(b).
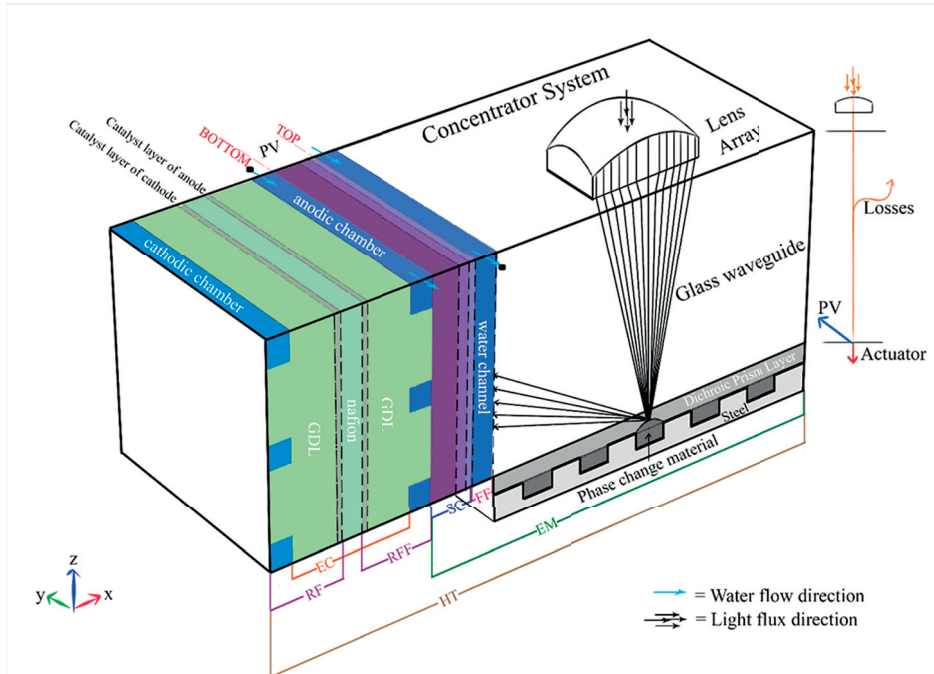
Fig. 1.11 3D schematic (not to scale) of the IPEC device including self-tracking concentrator depicting the incoming irradiation, the light trapping glass waveguide, the dichroic prism layer, the actuator (steel casing with paraffin wax cylinders), the cooling and preheating water channel, the solar cell (violet colors), and the integrated electrolyzer consisting of anodic and cathodic channels, gas diffusion layers (GDL), catalyst layers, and polymeric electrolyte (Nafion).

It has been confirmed experimentally [32] that 30-50 μm vertical expansion of wax cylinder is sufficient to cause proper actuation such that the low wavelength spectrum gets trapped inside glass waveguide. The required displacement of ~50 μm is achieved at 314 K, as shown in Fig. 1.12(b), which is around the melting point of the paraffin wax used. However, HT simulation concluded that only 10% of the heat absorbed in the wax cylinder is needed to heat it to 314 K, implying that the remaining 90% of the heat can be utilized in preheating water by putting channels beneath the actuator. Additionally, the total optical losses in the self-tracking concentrator amount to around 29% of the incoming radiation, see Fig. 1.12(a). Due to these losses the operating current density of the device for the case with self-tracking concentrator was much lower than the ideal case where the whole AM1.5G spectrum was incident on the PV without the spectral splitting by dichroic prism layer.

a)

b)
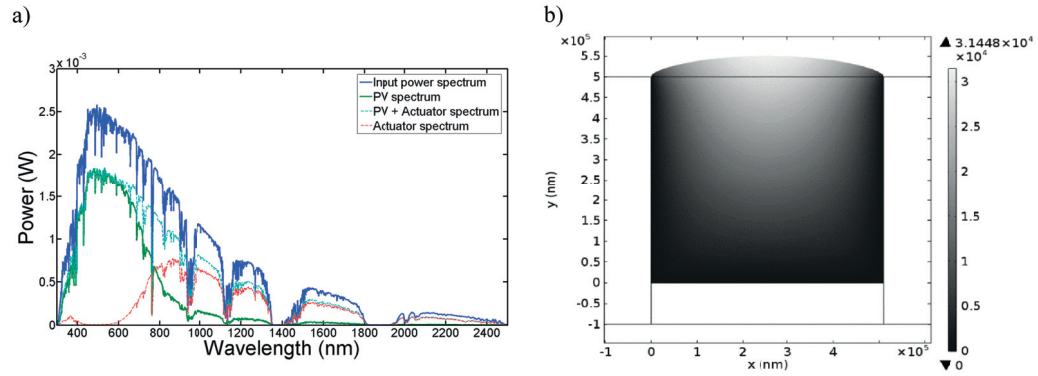
Fig. 1.12 Figure showing (a) input power spectrum (with AM1.5G), PV and actuator power spectrum in the case with self-tracking concentrator. (b) Wax expansion for a wax cylinder of 510 µm diameter and 500 µm height, at a temperature of ~314 K. The color legend in (b) shows the displacement of wax.

1.4	**Conclusion**

In this chapter, a coupled 2D multi-physics model and solution methodology has been developed to simulate the performance of integrated photoelectrochemical devices using concentrated solar irradiation. The model couples electromagnetic wave propagation, semiconductor charge generation and transport, heat transfer, fluid flow, mass transport, electrolyte and electrode charge transport, and electrochemical reactions. Finite element and finite volume methods were used to solve the governing equations and the corresponding boundary conditions. Complex temperature dependencies were included in the model. The absorbable spectrum changes with temperature and therefore requires an adaptive spectrum, changing for each iteration step, giving rise to a trade-off between precision and computation time. The various heat source/sink terms' calculations were treated in detail to ensure accurate energy calculations and to allow for subsequent effective thermal management. The model and its simulation flow were fully automatized. Efficient computational power saving techniques have been rigorously employed, making our model detailed yet computationally economic.

Two reference cases were defined, utilizing different photovoltaic (PV) components: *i*) a triple junction thin film aSi-ucSi-ucSi cell, and *ii*) a dual junction III-V based $Ga_{0.51}In_{0.49}P$-GaAs cell. These cells showed a decreasing trend in STH efficiency with increasing irradiation concentration. The low FF of the aSi-ucSi-ucSi cell resulted in a PEC device performance limited by both the electrocatalysts (i.e. the integrated electrolyzer) and the photoabsorbers (i.e. the PV). The high FF $Ga_{0.51}In_{0.49}P$-GaAs cell, on the other hand, was limited only by the electrolyzer's saturation current.

In order to maximize the produced amounts of H_2, using high irradiation concentrations is recommended. Large concentrations additionally benefit the economic competitiveness of the device [21]. However, due to the limiting saturation current of the electrolyzer and the relatively small FF of PV, there exists an optimal irradiation concentration. Larger concentrations (for device configurations with equal EC and PV areas) do not increase performance. The water channel on top of the PV can effectively cool the device if a large enough mass flow rate is chosen. For example, the device could be maintained at around 300 K for $C = 450$. The optimal mean flow velocity of water was found to be 0.2 m/s (or 40 g/s/m) for all irradiation concentrations. Large water mass flow rates provide a greater benefit in terms of cooling capability compared to smaller rates, and additionally provide more reactant to the electrodes, alleviating mass transport limitations.

J_{op} increases with increasing exchange current density, i.e. catalyst activity, at a particular C. A similar trend is observed for the STH efficiency. Changes in the

exchange current density show minimal changes in device temperature due to optimized thermal management. The dimensional properties such as membrane thickness lead to significant changes in the operating points, highlighting the importance of the membrane for thermal management in the integrated device. With increasing membrane thickness, the mass transport limitations are instigated earlier, resulting in reduced saturation currents. Despite large operating point variations, temperature variations are small (a few Kelvin only), as the water mass flow rate ensures proper device cooling. In spite of significant increases of heat sources, these minimal temperature variations attest to functional and efficient device thermal management. STH efficiency and H_2 production increase with increasing catalyst thickness, in contrast to the decreasing efficiency with increasing GDL thickness resulting from increased electronic and diffusional resistance.

To the best of the knowledge, the model developed in this analysis is the most detailed yet computationally economic model reported up to this point. The model allows for the investigation of any complex device design and geometry, and its simulation in fine physical detail. The model shows to be a valuable tool for the design of integrated PEC cells working with concentrated irradiation at elevated temperatures and illustrates that smart thermal management can assist in achieving efficient and low-cost production of solar fuel at large volumes. Thermal hot spots in a device operating at high irradiation concentration can be reduced utilizing calculated, spatially resolved temperature profiles, reducing the thermal and operational stress on photoabsorbers or catalysts, and potentially slowing their degradation rate. A more detailed analysis and the quantitative/qualitative benefits of smart thermal management for the integrated design of IPECs are detailed in follow-up studies [75] or chapter 2.

Thermal Management a Crucial Design Consideration[2]

2.1 Introduction

Today more than 95% of global hydrogen production is based on steam reforming of fossil fuels [5]. A promising sustainable approach to hydrogen production is solar driven, using integrated photoelectrochemical (IPEC) pathways. An IPEC device is defined as a device in which a (area-matched for particular design discussed in this chapter) photoabsorber and electrocatalyst are in direct contact. An integrated photoelectrochemical device design was proposed in chapter 1 and is detailed in Fig. 2.1. The design incorporates an electronic conductor for the transfer of charge carriers from the photoabsorber to the reaction site – as contrasted with devices designed with an ionic conductor - in order to reduce the overpotentials and to benefit from larger conductivities [76]. The issue for the economic competitiveness of PEC devices concerning the use of rare and expensive device component has been addressed through concentrating the solar irradiation.

Two examples of experimental investigation of non-integrated PEC devices using concentrated irradiation demonstrate that very interesting efficiencies can be achieved [68], [77]. However, irradiation concentration leads to driving current densities which are approximately proportional to the concentration factor, thus inducing larger overpotentials and possible mass transport limitations [25]. Optical concentration generally increases the device temperature and consequently enhances the kinetics and the ionic transport in the solid electrolyte (however, its conductivity drops at temperatures > 120°C due to membrane dry-out [22], [27]), while reducing the performance of the photoabsorbers [26]. A (concentrated) integrated photoelectrochemical device allows heat transfer between the components:

---

[2] The material from this chapter has been published in Journal of Electrochemical Society under the reference 'S. Tembhurne and S. Haussener, *J. Electrochem. Soc.*, 2016, **163**, 999–1007'.

transferring heat from components whose performance suffers from high temperature operation to components whose performance benefits from high temperature operation. Therefore, the overall performance of concentrated integrated photoelectrochemical (CIPEC) devices can potentially gain from smart thermal management, which is not possible in a non-integrated system. Thermal management is a rationale for CIPEC designs. Through dedicated modeling efforts, the aim is to support the development of thermal management strategies together with design and operational guidelines in order to maximize hydrogen production, energetic efficiencies, device durability, and to minimize device size and cost.

Several PEC modeling efforts have focused on 1-dimensional isothermal investigations [28]–[30]. In Haussener et al. [22], an isothermal model was used to predict the temperature-dependent performance behavior of PEC devices. None of the efforts were directed towards consideration of thermal management as a crucial design parameter. To incorporate this parameter, a fully automated coupled 2D multi-physics non-isothermal model was developed which uses finite element and finite volume methods to predict the performance of the concentrated integrated PEC device [78] which was discussed in chapter 1. The model has been validated [78] and accounts for: charge generation and transport in the triple/dual junction solar cell and the components of the integrated electrochemical system (polymeric electrolyte and solid electrode), electrochemical reaction at the catalytic sites, fluid flow and species transport in the channels delivering the reactant (water) and removing the products (hydrogen and oxygen), and radiation absorption and heat transfer in all components. Here, this model is used to quantify the gain in the performance of a CIPEC device, incorporating heat transfer between the different components and thermal management to actively steer the heat transfer process. Parametric analysis for various operational parameters (irradiation concentration, reactant flow rate), material parameters (exchange current density, active specific surface area), dimensional parameters (gas diffusion layer thickness, catalyst layer thickness, Nafion/separator membrane thickness) along with their effects on the device thermal profile is also presented in detail.

a)

b)
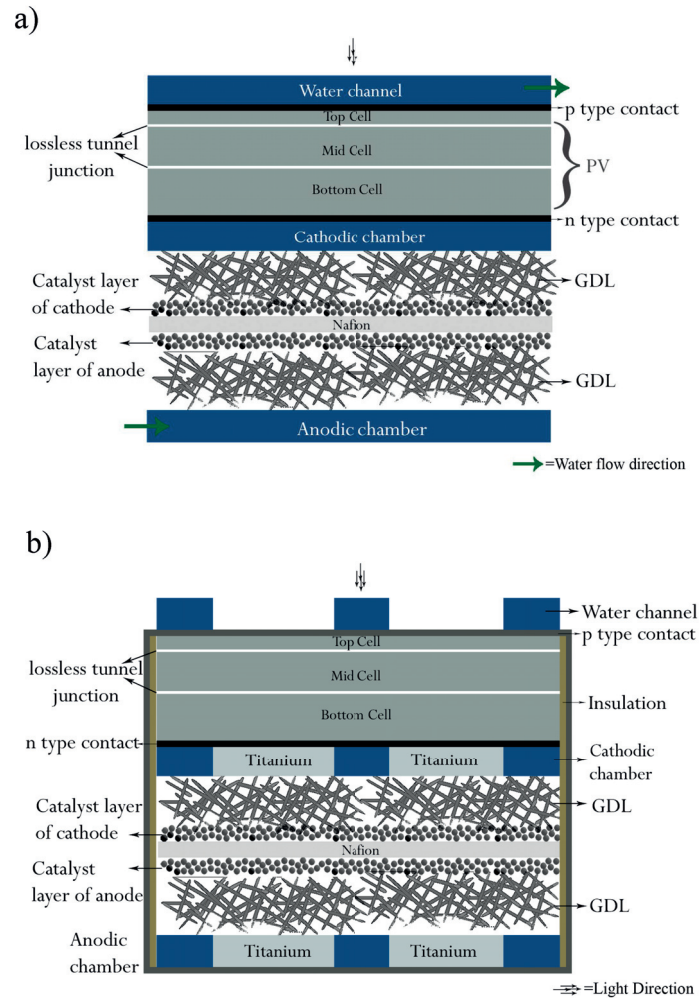
Fig. 2.1 Schematic (not to scale) showing (a) the top view and (b) the side view of the integrated PEC device depicting incoming concentrated irradiation, cooling and preheating water channel, triple/dual-junction PV, and the integrated electrochemical system consisting of anodic and cathodic channels, gas diffusion layers (GDLs), catalyst layers, and a polymeric electrolyte (Nafion). The 2D simulation domain is the plane shown in (a). A 3D schematic is shown in chapter 1 and Tembhurne et al. [78]. The water from the top water channel is fed to the anodic chamber shown in (a) with green arrows. The PV's top p-type contact is connected to the titanium flow plate of the anode side via an electronic conductor, providing a flow of positive charge (holes), shown in (b) with dark gray.

In the CIPEC shown in Fig. 2.1, the incoming concentrated irradiation is incident on the photoabsorber through the water channel. The absorbed photons with energies larger than the bandgap allow for the generation of charge carriers in the photoabsorber. The holes, coming from the p-side of the PV travel to the anodic catalyst, cause the oxidation of water to produce oxygen and protons. The electrons travel from the n-side of the PV to the cathodic catalyst and reduce the protons, which have traveled through the Nafion membrane, causing hydrogen evolution. The water from the top water channel removes the heat from the PV and is subsequently fed to the inlet of the anodic chamber of the electrochemical system, providing the preheated reactant.

Methodology

For electromagnetic (EM) wave propagation in any complex 2-dimensional geometry, the combined form of the Maxwell curl equations [35] is solved for the simulation of the electromagnetic field using the finite element method and MUMPS direct Solver [33]. The detailed modeling methodology is presented earlier in chapter 1 and in Tembhurne et al. [78]. The net heat source term coming from EM wave propagation is defined to be the sum of the individual source and sink terms:

$$Q_{EM_\lambda}^{PV} = Q_{TH}\big|^{\lambda < hc/E_g} + Q_R\big|^{\lambda > hc/E_g} + Q_M\big|^{\lambda > hc/E_g} \qquad (2.1)$$

$$Q_R + Q_M = -\nabla \cdot \mathbf{S}_{av_\lambda}\big|^{\lambda > hc/E_g} \qquad (2.2)$$

$$Q_{TH} = (1 - \frac{E_g}{h\nu})(-\nabla \cdot \mathbf{S}_{av_\lambda})\big|^{\lambda < hc/E_g} \qquad (2.3)$$

Q_R is electrical (resistive) loss, Q_M is magnetic loss, and Q_{TH} is thermalization loss. For simulation domains not involving semiconductors, such as water, the net heat source is simply $Q_{EM\lambda} = -\nabla \cdot S_{av\lambda}$. The overall Q_{EM} is calculated by summing the net heat source terms for individual wavelengths.

For the charge transport in the semiconductor (SC), the Poisson equation and current conservation equations are solved simultaneously using Fermi-Dirac statistics and a finite volume solver, incorporating the transport of electrons via the electron current density vector, $\mathbf{J_n}$, and holes via the hole current density vector, $\mathbf{J_P}$, where their sum gives the total current density [39]. The internal heat source term in the semiconductor is given by

$$Q_{PV} = \mathbf{J} \cdot \nabla V + (E_g + 3k_B T)U \qquad (2.4)$$

Where U is the net recombination. The first term ($\mathbf{J} \cdot \nabla V$) represents the ohmic losses, and the second term $(E_g + 3k_B T)U$ gives the recombination losses in the semiconductor. A detailed modeling methodology for the semiconductor simulation, electrochemical (EC) charge transport and reacting fluid flow, and heat transfer (HT) is presented in the companion paper [78] and was also presented earlier in chapter 1.

Charge transport in the electrolyte is simulated by the current conservation and Nernst-Planck equations, obeying electro-neutrality. Ohm's law is used for the current conservation in the electrode. The electrochemical reaction at the electrode-electrolyte interface is accounted for via the reaction current, i_{loc}, modeled via the

Butler-Volmer expression [49] for the anodic one-step oxygen evolution reaction (OER),

$$2H_2O \rightarrow O_2 + 4H^+ + 4e^-, \tag{2.5}$$

and cathodic one-step hydrogen evolution reaction (HER),

$$4H^+ + 4e^- \rightarrow 2H_2. \tag{2.6}$$

The charge conservation equations in the electrode and electrolyte are solved via finite element methods and a MUMPS solver. The fluid flow and mass transport in the channels and the porous gas diffusion layers (GDLs) are modeled by the Navier-Stokes equation with Darcy extension [50], [51]. Species transport for the low density fluid mixture is modeled by the Maxwell-Stefan diffusion model [52]. The water at the output of the water channel is fed to the anodic channel at its inlet with normal velocity, ν_{water}. The heat source in the electrochemical system [21], comprised of electrode ohmic losses, electrolyte ohmic losses and kinetic losses, is given by:

$$Q_{EC} = -\mathbf{J}_s \cdot \nabla \phi_s - \mathbf{J}_l \cdot \nabla \phi_l + (\phi_s - \phi_l - E_{eq} + T\frac{\partial E_{eq}}{\partial T})i_{loc}. \tag{2.7}$$

For heat transfer, the steady-state energy conservation equation [54] is solved using finite element methods in order to calculate the temperature field in the PEC device. $Q_H = Q_{EM} + Q_{PV} + Q_{EC}$ describes the total heat source for the integrated PEC which includes the heat from electromagnetic heating, semiconductor transport, and electrochemical reactions.

Non-isothermal treatment was used in the entire modeling framework. Variations of temperature-dependent parameters, detailed simulation flow and coupling between different physical nodes have been shown in Tembhurne et al. [78]. Urbach tails and defect states in amorphous/microcrystalline semiconductors were incorporated using wxAMPS [34]. The simulation flow is completely automatized using multiple interactions between Matlab, Comsol, and wxAMPS. Efficient computational power saving techniques were rigorously employed, making the model detailed yet computationally economic in nature.

2.3 Results and Discussion

The temperature independent baseline parameters used in this study are shown in chapter 1 Table 1.1. The operational temperature was maintained below 80ºC, implying operation with liquid water and no dry-out of the polymeric electrolyte membrane. The results and discussions for various parametric analysis and the effects of thermal management are presented. The results are for reference case I (i.e. for thin film aSi-ucSi-ucSi based PEC) unless otherwise specified.

2.3.1 Operating conditions: Irradiation concentration and water mass flow rate Water mass flow rate plays a major role in the thermal management. Water with an initial temperature of 293 K is fed through the inlet with varying mass flow rates per length (range: 6 g/s/m to 400 g/s/m), corresponding to varying normal velocities of the water (range: 0.03 m/s to 2 m/s). The two objective functions, H_2 production rate and STH efficiency, were studied for each change in water mass flow rate for a range of irradiation concentrations (1-1000). The H_2 production rate is proportional to the operating current density.

For any concentration in the low concentration range (i.e. $C < 300$), the increase in mass flow rate leads to a decrease in H_2 production, $\dot{M}_{H_2}$, as is evident from Fig. 2.3(a), though this decrease is minimal. At larger C, this trend reverses and H_2 production increases. This increase becomes more significant in the larger concentration range (i.e. 750-1000). Fig. 2.3(b) shows a similar trend for STH efficiency. The reversal in trend for both H_2 production and STH efficiency is due to the two specific operating regions observed in the characteristic J-V curves. The occurrence of these two regions in detail is explained herewith.

The slope of the linear region of the EC curves decreases with decreasing mass flow rate, see Fig. 2.2, due to increased charge transport losses, mostly resulting from the increased temperature of the stream. The saturation current of the EC decreases with decreasing mass flow rate due to mass transport limitations occurring in the porous electrodes. Due to this behavior, the EC curves for varying mass flow rates at a given concentration intersect in a small voltage range, giving rise to two regions of characteristic operation for the device (indicated as regions I and II). In region I, at a particular C, the EC curves shift to the right side on the voltage scale with increasing mass flow rate, while in the region II they shift to the left side. The identification of the two characteristic operating regions explains the performance effects observed for varying concentrations: increasing the concentration from small to large values shifts the operational point from the region I to region II, resulting in the previously discussed trend for H_2 production rates and STH efficiencies. The

stronger changes observed for concentrations above 450 result from operation in the falling region of the *J-V* curve of the PV, leading to a drastic efficiency decrease with mass flow rate decrease.
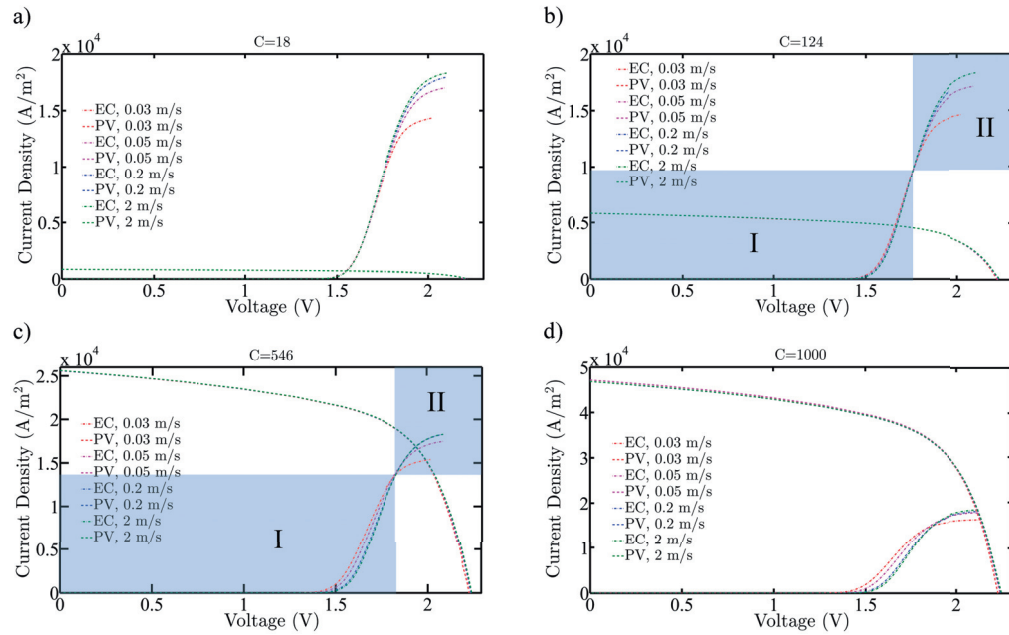
Fig. 2.2 Characteristic curves for mass flow rate analysis for reference case I, for irradiation concentrations of (a) *C* = 18, (b) *C* = 124, (c) *C* = 546, and (d) *C* = 1000. The colors, from red to violet, blue, and green represent increasing mean flow velocity of water (0.03, 0.05, 0.2, 2 m/s).

Average EC and PV temperatures, Figs. 2.3(c)-(d), decrease with increasing water mass flow rates. At a mean flow velocity of 0.03 m/s, there is a 40-fold increase in the Q_{EC} (EC heat source) when going from *C* = 53 to 1000. At a mean flow velocity of 2 m/s, for the same concentration range, the increase in the Q_{EC} is 48-fold. Similar behavior is observed for the PV heat source, Q_{PV}. However, despite of significant increases in heat sources, the temperature increase in the EC and PV at large mass flow rates is only a few Kelvins, as opposed to increases in temperature of tens of Kelvins for low mass flow rates.

These results imply that higher water mass flow rates have a better cooling capability than low mass flow rates. Additionally, high mass flow rates allow the operation at high *C* with the increased saturation of EC, and hence increased operating currents.
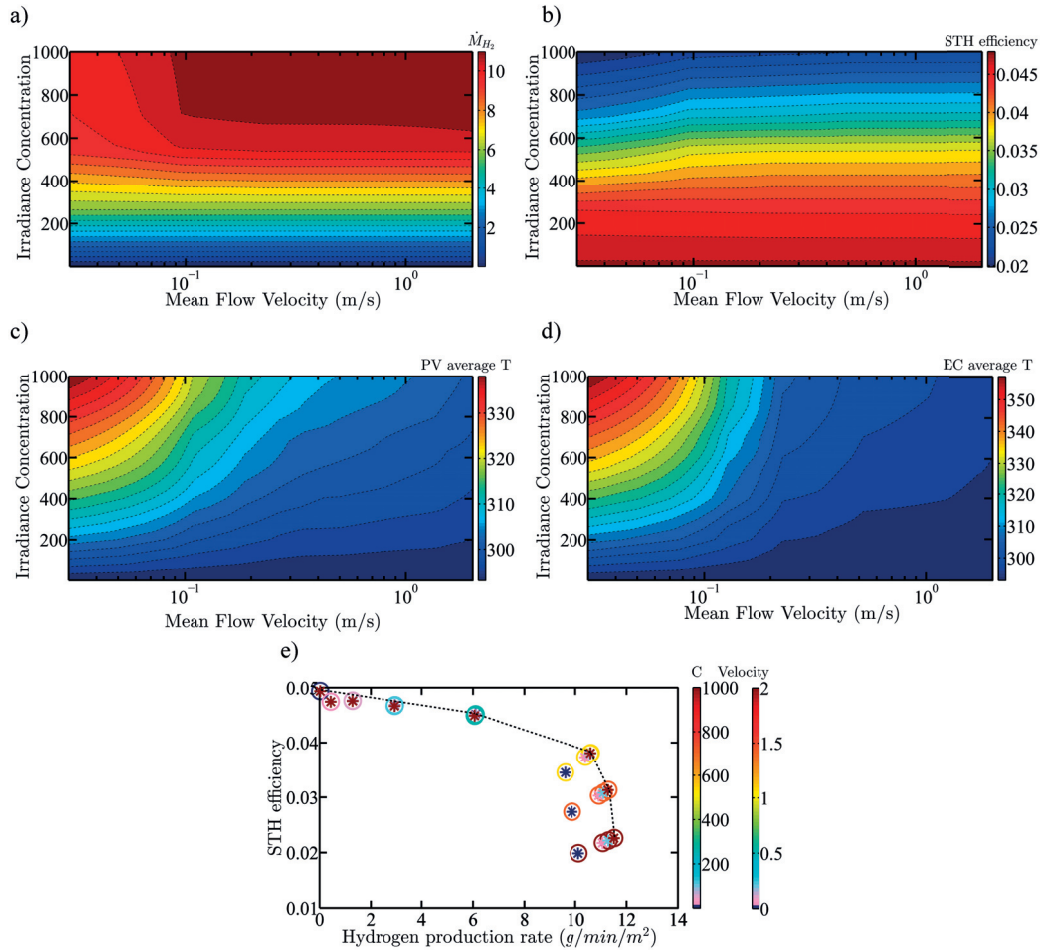
Fig. 2.3 Contour plots showing the evolution of (a) hydrogen production rate [g/min/m²], (b) STH efficiency, (c) average PV temperature [K], and (d) average EC temperature [K], as a function of varying irradiation concentrations and water mean flow velocities for reference case I (Si based PV). (e) Operating STH efficiency for varying mean flow velocities and C as a function of hydrogen production rate. The Pareto front in (e) is shown by the dotted black line. The color of the circles represents concentration and the color of the stars represents the mean flow velocity [m/s].

The optimum region of device operation for highest H_2 production occurs in the large concentration range (700-1000) at large water mean flow velocities (0.1–2 m/s). In contrast, the preferred region of operation maximizing the STH efficiency lies in

the low concentration range and is independent of the mean flow velocities in the inspected range (0.03-2 m/s). This competitiveness in the objectives of H_2 production and STH efficiency is plotted in Fig. 2.3(e). With the aim of having increased H_2 production along with increased STH efficiency, it is observed that the various device configurations, Fig. 2.3(e), form a Pareto front implying the absence of a global optimum but the existence of a range of semi-optimal efficiencies. The frontier has no specific trend with respect to C but consists mainly of parameter combinations with the highest mean flow velocity. The optimum mean flow velocity is around 0.2 m/s, as evident from Fig. 2.3, above which the variations in STH efficiency, H_2 production, and temperature become negligibly small.
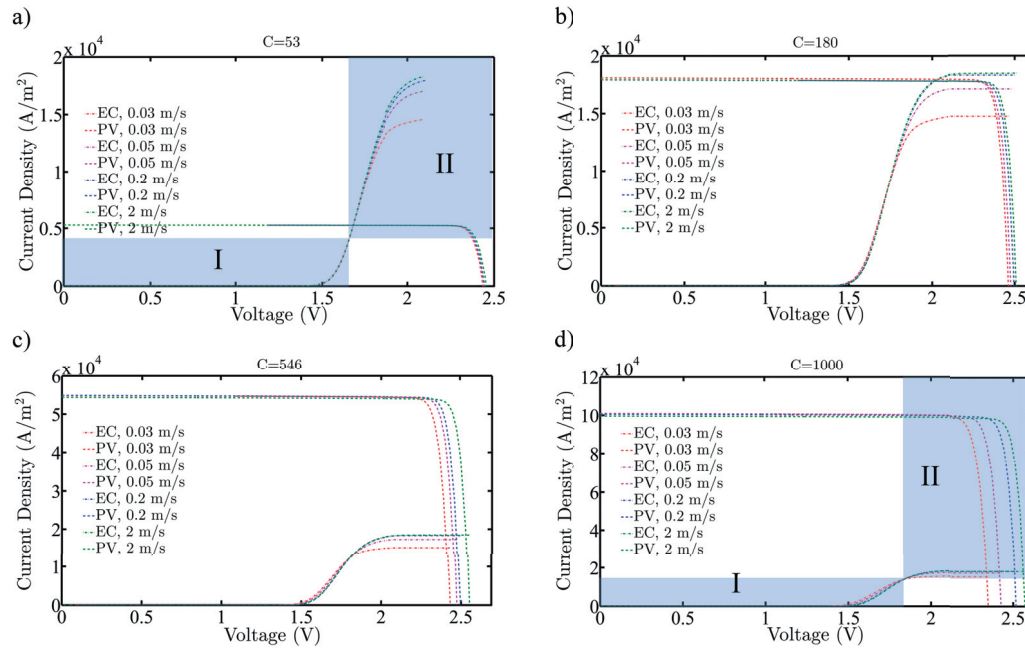
Fig. 2.4 Characteristic curves for the mass flow rate analysis, for reference case II (III-V based PV), for irradiation concentrations of (a) $C = 53$, (b) $C = 180$, (c) $C = 546$, and (d) $C = 1000$. The color from red to violet, blue, and green represents increasing mean flow velocity of water (0.03, 0.05, 0.2, 2 m/s).

For reference case II, i.e. with a dual junction $Ga_{0.51}In_{0.49}P$-GaAs, the characteristic curves and variations of the objective functions are presented in Figs. 2.4-2.5. A similar behavior as for the reference case I is observed, including the formation of the two distinct operational regions (I and II). However, the bandgaps for the $Ga_{0.51}In_{0.49}P$-GaAs cell are more sensitive to the temperature, and therefore a clear

difference in the PV J-V curves with changing mass flow rates is observed. The optimal concentration is at $C = 180$ and a mean flow velocity of 0.2 m/s. For larger concentrations, the J_{sc} of the PV is always larger than the saturation current of the EC (i.e. for the case when PV area is equal to EC area as shown in Fig. 2.1). The J_{op}, and therefore $\dot{M}_{H_2}$, minimally increase with increasing mean flow velocity until $C =$ 150, and significantly increase for $C = 150$ to 1000. The STH efficiency increases with increasing mass flow rate. For reference case II, the J_{op} and STH efficiency trends are not the same as for the reference case I. There is no reversal in trend for H_2 production and STH efficiency as C increases, despite the formation of two distinct operational regions. This follows from the location of the operational points, which always lie in region II. The temperature variations show the same behavior as reference case I. The tradeoff between H_2 production and STH efficiency also leads to a Pareto front for reference case II. However, this front is relatively flat and closer to a global optimum. For reference case II, ~100% of the maximum STH efficiency and ~96% of the maximum H_2 production can be chosen at the same time whereas for reference case I the best configuration turns out to be the one with 50% of the maximum of both objective functions.

The regions of enhanced performance for the thin film Si based device and III-V based device are quantified in Figs. 2.6(a) and (b) respectively. The contour plot of Fig. 2.6(a) agrees with the STH efficiency trend reversal after $C = 300$ shown in Fig. 2.3(b). The x-axis value of 1 corresponds to the reference mean flow velocity, v^0_{mean}, of 0.2 m/s. η^0_{STH} is the STH efficiency at 0.2 m/s for the corresponding concentration. Fig. 2.6(a) shows that maximum efficiency enhancement is observed for $C > 300$ and 0.1 m/s $\geq v_{mean} \geq$ 0.03 m/s. For example at $C = 546$, the STH efficiency increases by 9.2% when v_{mean} increases from 0.03 to 0.2 m/s. For the III-V based case, the significant STH efficiency improvement is seen for $C > 180$ and 0.1 m/s $\geq v_{mean} \geq$ 0.03 m/s. For example at $C = 546$, an efficiency increase of 17.5% is observed for an increase in v_{mean} from 0.03 to 0.2 m/s. Both plots show that there are large efficiency enhancements for higher concentrations with increases in the mass flow rates.

In summary, the mass flow rate plays an integral role in thermal management in integrated devices. IPEC devices can be operated without a significant decrease in performance, even at very high irradiation concentrations, provided the water flow velocity in the cooling channel is at least 0.2 m/s. The changing mass flow rate doesn't affect the performance at low C, but has the potential to significantly improve STH efficiency for larger concentrations. When operating in region II (often given at high C), the mass flow rate allows for control of the operating point of the integrated device and thus can be used as a controlling parameter to counteract

component degradation over the device lifetime. This is particularly pronounced if the operation is close to the maximum power point of the PV. It is predicted that the device degradation and the corresponding decrease in performance over the lifetime of the system can be controlled by smart thermal management.
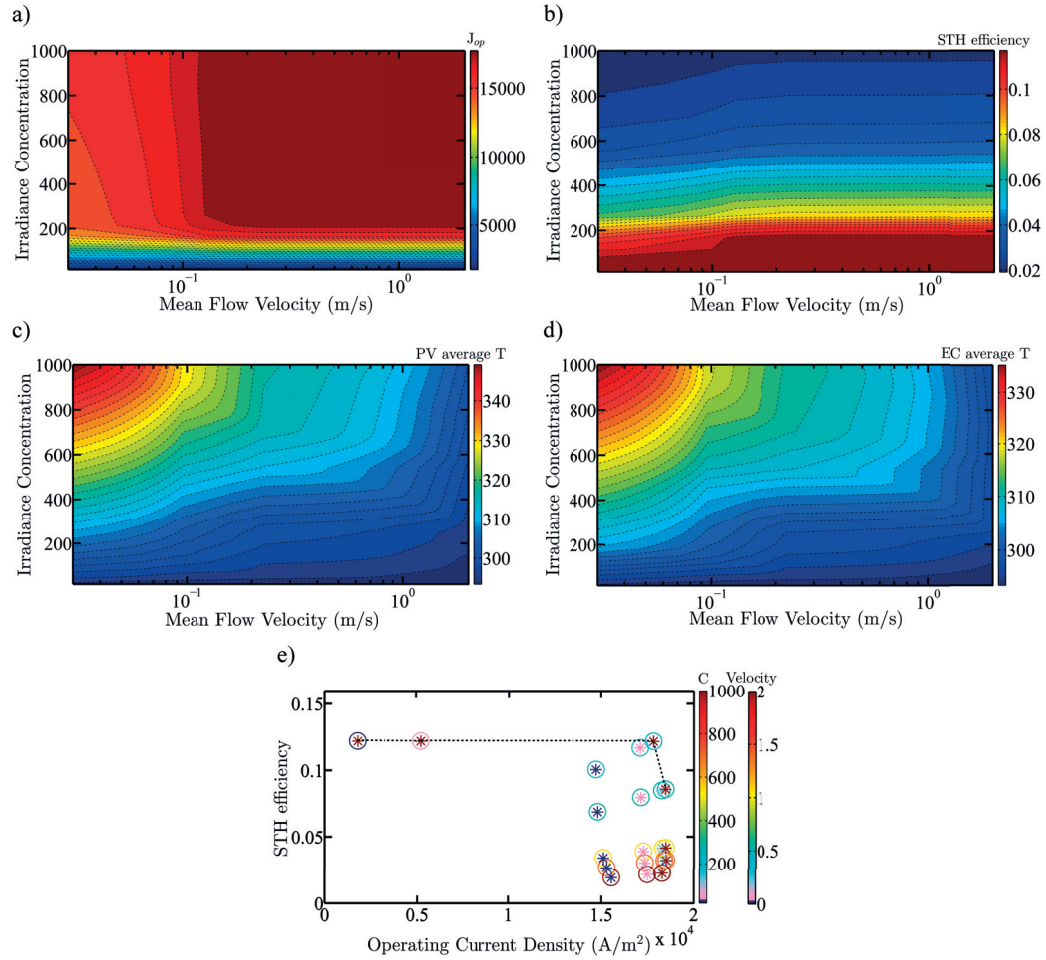
Fig. 2.5 Contour plots showing evolution of (a) operating current density [A/m²], (b) STH efficiency, (c) average PV temperature [K], and (d) average EC temperature [K], as a function of varying irradiation concentrations and water mean flow velocity for reference case II (III-V based PV). The operating STH efficiency for varying (e) irradiation concentrations, and mean flow velocities, as a function of operating current density for the mass flow rate analysis. The dotted black line in (e) shows the Pareto frontier. The color of the circles represents concentration and the color of the stars represents the mean flow velocity [m/s].

For the operation of the Si-based device at $C = 707$, a 12% degradation in STH efficiency can be compensated with a seven-fold increase in the water mass flow rate if the operating point remains in region II, i.e. degradation overpotential in the EC is limited to about 250 mV. This shows that smart thermal management - possible due to the integrated nature of our device design - contributes significantly to a device with stabilized and high performance over an elongated fraction of device lifetime. Additionally, thermal management controls and/or reduces the component temperature, which is expected to further reduce the rate of thermally-induced degradation phenomena.

a)

b)
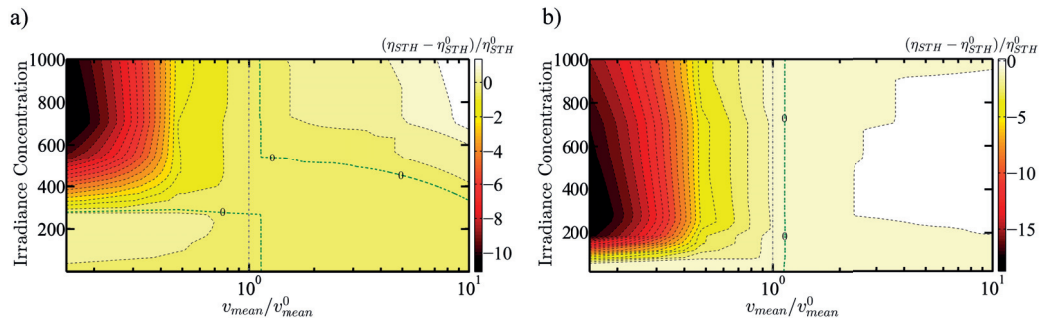
Fig. 2.6 Contour plots showing the STH efficiency enhancement in percentage with respect to the reference case for (a) the thin film triple junction aSi-ucSi-ucSi, and (b) the $Ga_{0.51}In_{0.49}P$-GaAs dual junction based integrated PEC device. The reference velocity, v^0_{mean}, is 0.2 m/s. η^0_{STH} is the STH efficiency at 0.2 m/s for the corresponding concentration. The green contour line represents the 0 level. $\eta^0_{STH,C=1}$ = 4.94%, $\eta^0_{STH,C=18}$ = 4.74%, $\eta^0_{STH,C=124}$ = 4.67%, $\eta^0_{STH,C=265}$ = 4.49%, $\eta^0_{STH,C=546}$ = 3.80%, $\eta^0_{STH,C=707}$ = 3.08%, $\eta^0_{STH,C=1000}$ = 2.22% for the thin film Si case. $\eta^0_{STH,C=1}$ = 12.21%, $\eta^0_{STH,C=53}$ = 12.20%, $\eta^0_{STH,C=180}$ = 12.18%, $\eta^0_{STH,C=265}$ = 8.48%, $\eta^0_{STH,C=546}$ = 4.13%, $\eta^0_{STH,C=707}$ = 3.20%, $\eta^0_{STH,C=1000}$ = 2.25% for the III-V based PV case.

2.3.2 Material choices – Catalyst characteristics The catalysts characteristics investigated are- exchange current density and active specific surface area (ASSA). For reference case I, the exchange current density for each electrode and its temperature variation is given in Table 1.1 of chapter 1, representing Pt and IrO_2 catalysts. The evolution of produced H_2 and STH efficiency of the device for varying exchange current densities of the anodic and cathodic reactions is shown in Figs. 2.7(a)-(b). $\dot{M}_{H_2}$ increases with increasing exchange current densities at a given concentration. This increase is only significant in a concentration range between 250 and 650. Outside this range, J_{op} varies minimally. This behavior results from the

location of the operational points, which lie either in the flat region of the PV (for C < 250) or in the saturation region of the EC (for C > 650). A similar trend is observed for the STH efficiency resulting from the nature of the J-V curves, Fig. 2.8. The EC's J-V curves start separating as the voltage increases above E_{eq} due to the increased activation overpotential at smaller exchange current densities. The EC's J-V curves stay almost constant (parallel) in the linear region, as ohmic losses are not affected, and coincide towards the saturation region. This behavior implies that the mass transport limit is also not affected by the change in exchange current density.
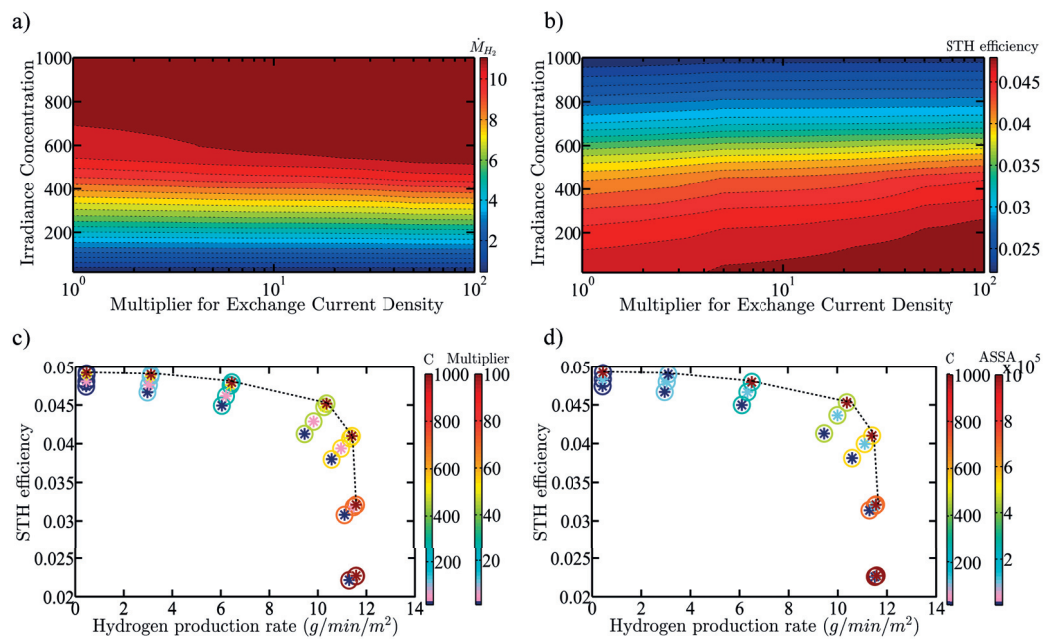
Fig. 2.7 Contour plots showing evolution of (a) hydrogen production rate [g/min/m^2], and (b) STH efficiency as a function of varying irradiation concentrations and exchange current density multipliers. Operating STH efficiency for varying (c) exchange current density multipliers and (d) active specific surface area (ASSA) for varying C as a function of H$_2$ production rate. The Pareto front is shown by the dotted black line. The color of the circles represents concentration and the color of the stars represents the (c) multiplier or (d) ASSA.

The characteristic curves for varying combinations of irradiation concentrations (18-1000) and exchange current density multipliers (1-100 fold increase) are shown in Fig. 2.8. The high C curves of the EC intersect the PV curves in their falling region. The average EC and PV temperatures for the exchange current density analysis are

shown in Figs. 2.8(e)-(f). Both EC and PV temperatures change minimally (less than 1 K) with the increasing exchange current density. The similar behavior is observed for varying active specific surface area.
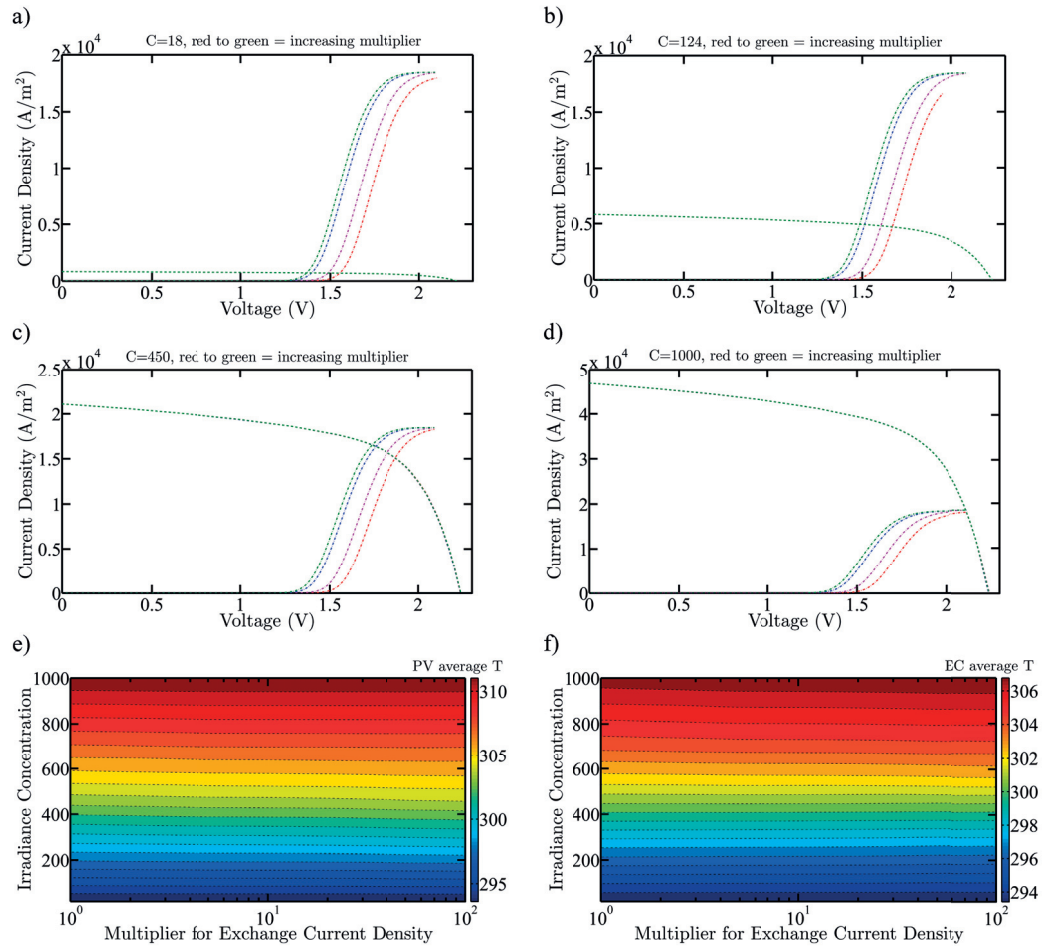
Fig. 2.8 Characteristic curves for the exchange current density analysis for irradiation concentrations of (a) $C = 18$, (b) $C = 124$, (c) $C = 450$, and (d) $C = 1000$. The color from red to violet, blue, and green represents increasing exchange current density multipliers (1, 5, 50 and 100). The contour plots showing the evolution of (e) the average PV temperature [K], and (f) the average EC temperature [K], as a function of varying irradiation concentrations and exchange current density multipliers.

The active specific surface area (ASSA) is defined as active surface area divided by the volume. The variation of $\dot{M}_{H_2}$ and STH efficiency with C and ASSA show very similar behavior to the varying exchange current density multiplier case. Hydrogen production was found to minimally increase with increasing ASSA for $C \leq 600$. For larger C, J_{op} becomes independent of ASSA. The STH efficiency increases significantly at medium C (~ 9.8% increase for an increase from 10^4 to 10^6 m^{-1} in ASSA at $C = 450$) but remains constant at large C. The J-V curves of the EC show similar trends to those observed for changing exchange current densities.

Maximum H$_2$ production can be achieved at a large concentration ($C = 700$-1000) independent of the chosen exchange current density and ASSA. However, maximal STH efficiency is achieved at the lowest C and highest exchange current density, utilizing electrodes with large ASSA. This contradictory choice for optimized operation results in a Pareto front, Figs. 2.7(c)-(d). The fronts are comprised of devices which utilize the largest exchange current densities or ASSA.

In summary, at large irradiation concentration the exchange current density and ASSA do not affect the operating current density, and consequently, a production rate insensitive to the chosen catalysts is predicted. However, the efficiency increases (by 7.8% for exchange current density increase by a factor of 100) for the case with $C = 546$ when the catalysis is enhanced. The highest exchange current density and the ASSA are required for device operation on the Pareto front, i.e. compromising between efficiency and hydrogen production. A ~9.5% increase in hydrogen production caused by increasing the multiplier from 1 to 100 at $C = 450$ only causes a ~0.3% increase in temperature. Similar behavior is observed for temperature variations for the ASSA analysis. This insensitivity of the temperature, despite a significant increase in the heat source, is a result of smart thermal management, with a mean flow velocity of 0.2 m/s, which is the optimized value, see section 2.3.1.

2.3.3 Dimensions and design
2.3.3.1 Membrane thickness The variation of the thickness of the solid electrolyte (a Nafion membrane) affects the diffusional driving force of the ions across the membrane and the membrane's concentration-dependent conductivity. The J-V curves for varying membrane thickness (30-100 μm), Fig. 2.10, show that the operating point changes significantly with changing membrane thickness. Changing membrane thickness has a larger impact on the device performance for large C because, in this case, the operating points lie in the falling region of the PV's J-V curve. The concentration overpotential and ohmic losses are significantly affected

by membrane thickness. They increase with increasing thickness with no change in the activation overpotential.
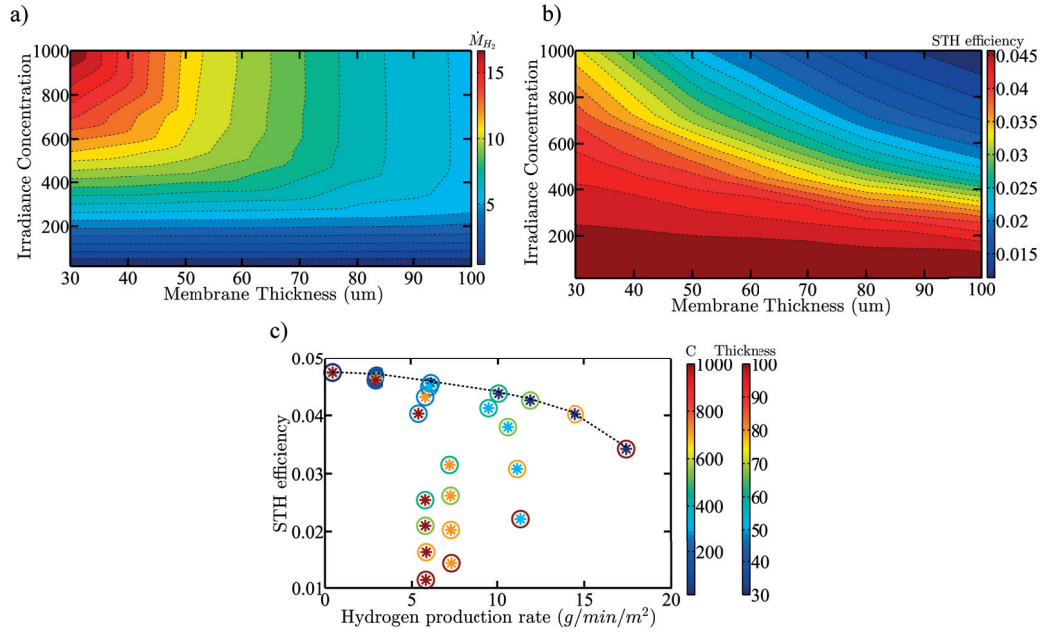
Fig. 2.9 Contour plots showing the evolution of (a) the hydrogen production rate [g/min/m^2], and (b) the STH efficiency as a function of varying irradiation concentrations and Nafion membrane thicknesses. The STH efficiency for varying (c) concentrations and membrane thicknesses as a function of H$_2$ production rate. The Pareto front is indicated by the dotted black line. The color of the circles represents concentration and the color of the stars represents the membrane thickness.

The variation of the amount of H$_2$ produced with varying membrane thicknesses and for different irradiation concentrations is shown in Fig. 2.9(a). J_{op}, and hence H$_2$ production, decrease insignificantly with increasing membrane thickness up to $C = 200$. For $C > 200$, the decrease in J_{op} becomes drastic, i.e. ~60% decrease at $C = 546$. A similar behavior is observed for the STH efficiency, Fig. 2.9(b). Maximum H$_2$ production occurs at the largest C and for the thinnest membrane, while the STH efficiency is maximal for small C and independent of the membrane thickness. The tradeoff between H$_2$ production and STH efficiency is shown in Fig. 2.9(c), showing a Pareto frontier. The Pareto front includes the smaller membrane thickness, but no specific trend exists for C.
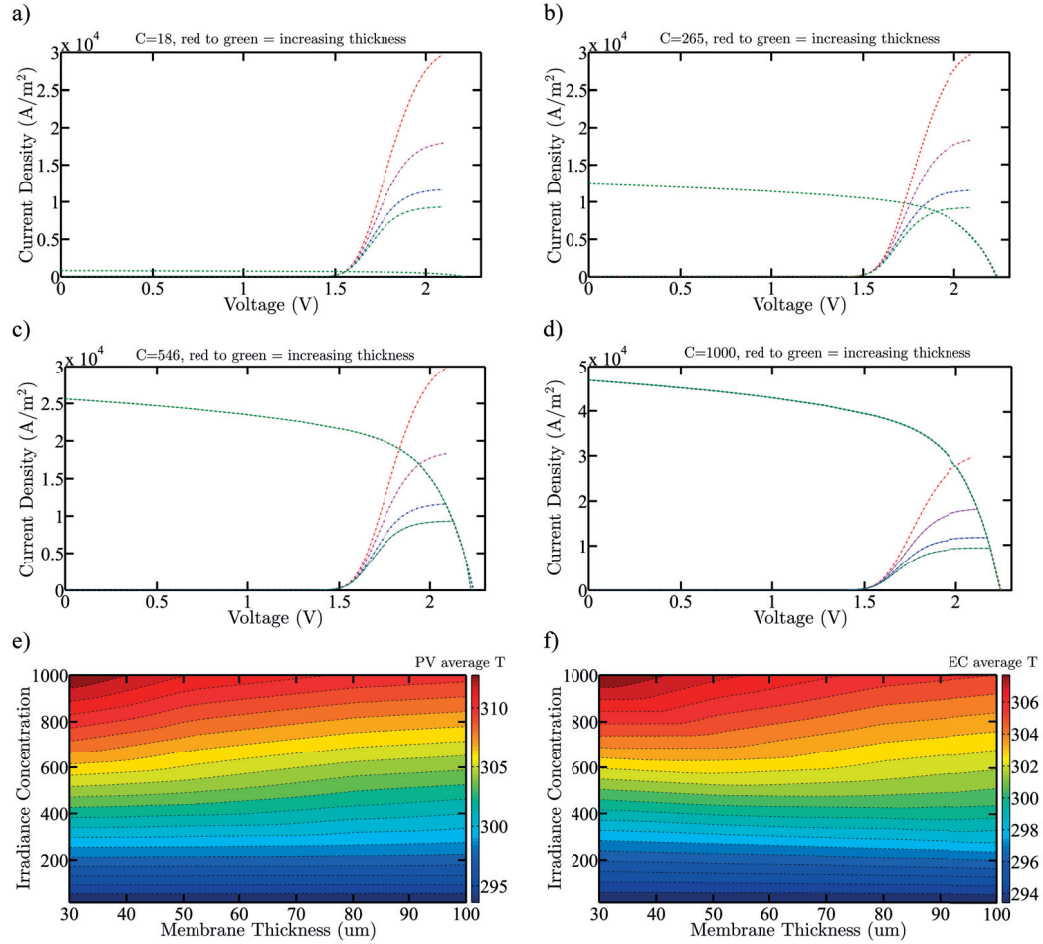
Fig. 2.10 Characteristic curves for the membrane thickness analysis for irradiation concentrations of (a) $C = 18$, (b) $C = 265$, (c) $C = 546$, and (d) $C = 1000$. The color from red to violet, blue, and green represents increasing membrane thicknesses (30, 50.8, 80 and 100 μm). The contour plots showing the evolution of (e) the average PV temperature [K], and (f) the average EC temperature [K], as a function of varying irradiation concentrations and membrane thicknesses.

The average PV and EC temperatures, Figs. 2.10(e)-(f), show minimal variations at a given C with varying membrane thickness. However, for an example case with $C = 1000$, Q_{EC} increases by 2.7 times and Q_{PV} by 1.21 times as the membrane thickness decreases from 100 to 30 μm. This increase in the overall heat source at a large irradiation concentration is a direct result of the large variations in the operating

current. This behavior is also observed for $C > 200$. The temperature variation is only a few Kelvins for this heat source increase, indicating that the device has a good thermal management, which is the result of the water flow velocity choice of 0.2 m/s, an optimized velocity according to mass flow rate analysis (section 2.3.1). The average PV temperature remains constant for low irradiation concentrations. At large C for increasing membrane thicknesses, the PV temperature decreases and this rate of decrease increases for higher C. The average EC temperature increases (for $C = 1$-450) and then decreases (for $C > 450$) because Q_{EC} follows the same trend.

At small irradiation concentrations, the membrane thickness appears to not be relevant for the operating current and only slightly affects the efficiency. For larger concentrations, the membrane thickness must be minimized in order for the device to operate under conditions of the Pareto front.

2.3.3.2 Catalyst and GDL layer thickness

a. Catalyst thickness Here the effect of variation in the thickness (50-200 nm) of the two catalyst layers is discussed. The evolution of STH efficiency and J_{op}, Figs. 2.11(c)-(d), shows that J_{op} insignificantly increases with increasing catalyst layer thickness. STH efficiency has its largest increase at $C = 450$, where its operating point is near the maximum power point of the PV. This concentration spans the largest operating current density change with varying catalysts thicknesses. The J-V curves, Figs. 2.11(a)-(b), illustrate that the activation and concentration overpotentials decrease with almost no change in the ohmic losses when catalyst thicknesses are increased. Average PV and EC temperatures, Figs. 2.11(e)-(f), are independent of catalyst thickness variations, mainly because the heat sources are insensitive to these thickness variations and because the reference flow velocity of the water (0.2 m/s) optimally removes the heat. The combined optimization of STH efficiency and J_{op} forms a Pareto frontier as shown in Fig. 2.13(a), with the front comprised mainly of the thicker catalyst.
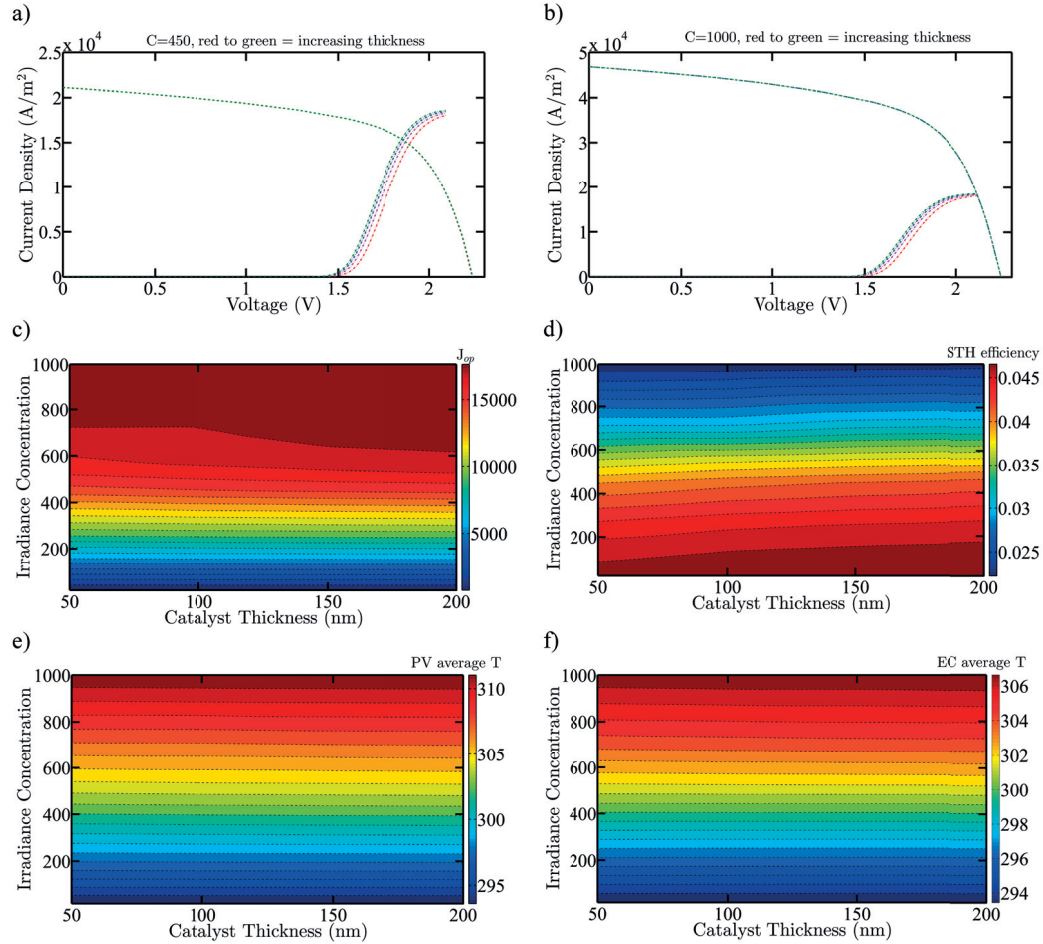
Fig. 2.11 Characteristic curves for the catalyst thickness analysis for irradiation concentrations of (a) $C = 450$, and (b) $C = 1000$. The color from red to violet, blue, and green represents increasing catalyst thicknesses (50, 100, 150, and 200 nm). The contour plots showing the evolution of (c) operating current density [A/m^2], (d) STH efficiency, (e) average PV temperature [K], and (f) average EC temperature [K], as a function of varying irradiation concentrations and catalyst thicknesses.

b. Gas diffusion layer (GDL) thickness The GDL thicknesses of both the anodic and cathodic sides were varied in the range of 300-800 μm. The evolution of $\dot{M}_{H_2}$ shows that H$_2$ production decreases minimally with increasing GDL thickness (e.g. ~0.7% decrease for $C = 124$ with a thickness increase from 300 μm to 800 μm). STH efficiency follows the same behavior. However, for the higher concentration

range (C = 750-1000), the STH efficiency and hydrogen production remain constant with increasing GDL thickness. The *J-V* curves, Figs. 2.12(a)-(b), show that the slope of the EC curve in the linear region decreases with an increase in GDL thickness, however, the saturation current of the EC stays nearly the same.
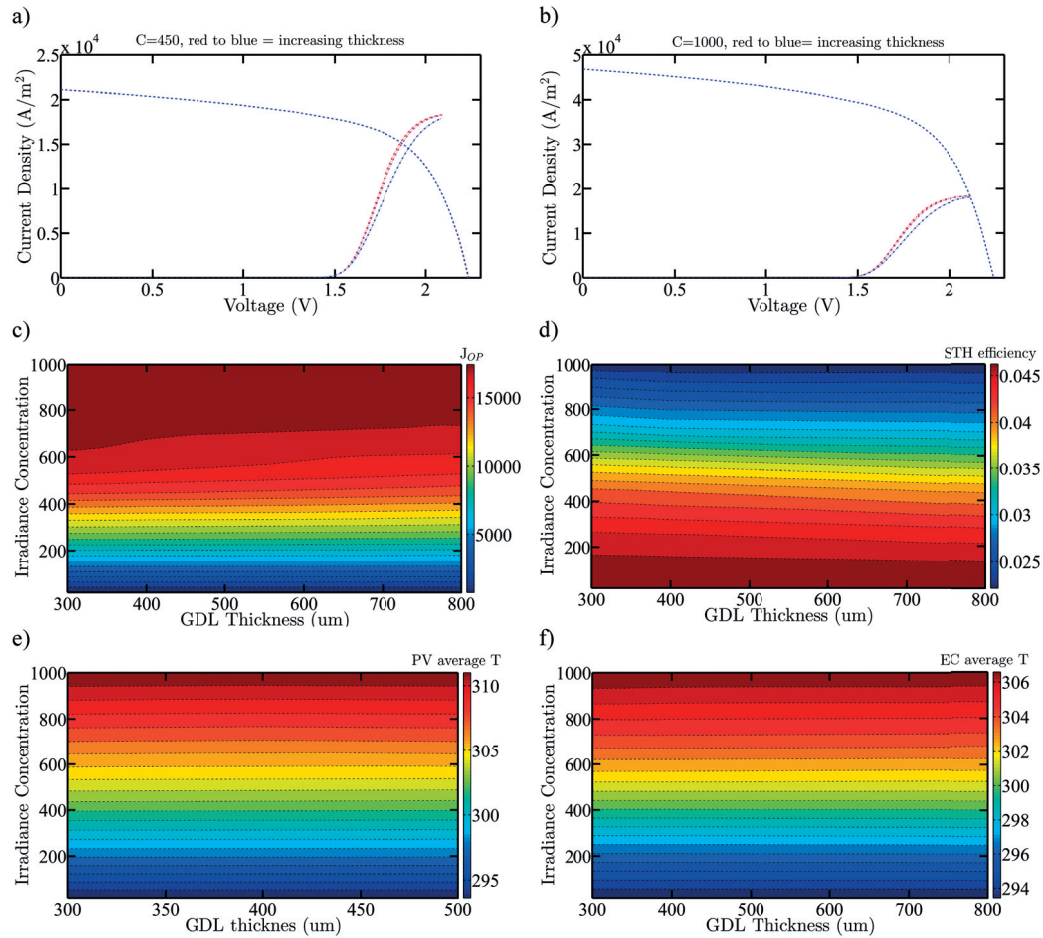
Fig. 2.12 Characteristic curves for the GDL thickness analysis for irradiation concentrations of (a) C = 450, and (b) C = 1000. The color from red to violet and blue represents increasing GDL thicknesses (300, 400, 800 μm). The contour plots showing the evolution of (c) operating current density [A/m²], (d) STH efficiency, (e) average PV temperature [K], and (f) average EC temperature [K], as a function of varying irradiation concentrations and GDL thicknesses.

This implies that ohmic losses due to charge transport in the EC increase, whereas the saturation current of the EC doesn't change with increasing GDL thickness. Additionally, no change in the activation overpotential was noticed. The average PV and EC temperatures, Figs. 2.12(e)-(f), were found to be nearly independent of GDL thickness variations, primarily because the heat sources were found to be insensitive to this thickness variation at the chosen mean flow velocity of water, 0.2 m/s (optimized value). The combinations of C and GDL thickness which result in maximum STH efficiency (C = 1-150 and independent of GDL thickness) and H_2 production (C = 700-1000 and independent of GDL thickness) do not coincide, again forming a Pareto frontier, Fig. 2.13(b). This front has no particular trend with respect to C but consists mainly of the smallest GDL thicknesses.
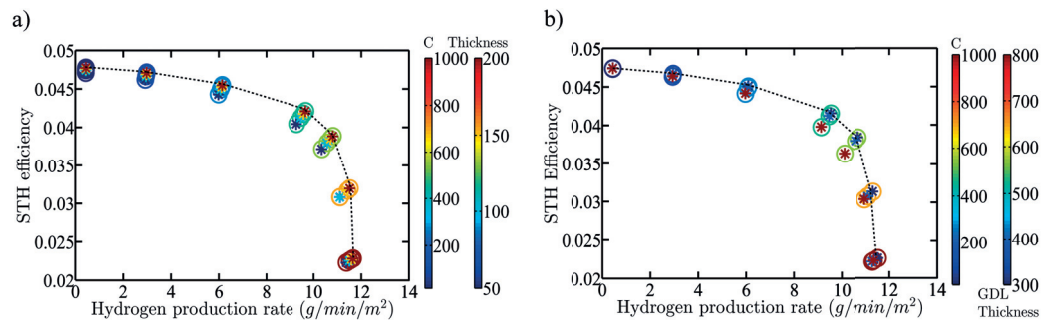
Fig. 2.13 Operating STH efficiency for varying (a) anodic and cathodic catalyst thicknesses, (b) anodic and cathodic GDL thicknesses as a function of hydrogen production rate. The Pareto front is shown by the dotted black line. The color of the circles represents concentration and the color of the stars represents the (a) catalyst thickness and (b) GDL thickness.

2.3.4 Saturating behavior of performance parameters Variation of the hydrogen production rate and STH efficiency with the investigated dimensional, operational, and material parameters is found to follow a saturating trend. This behavior is shown in Fig. 2.14 for C = 707.

The objective performance functions (J_{op} and STH efficiency) change somewhat significantly with an increase of the dimensional (GDL and catalyst layer thickness), material (ASSA and exchange current density), and operational (water velocity) parameters. Nevertheless, a saturation level is reached where any further increase in these parameters does not affect the performance. For GDL and catalyst thicknesses, the decreasing slope signifies the onset of the saturation area. Mean flow velocity of 0.2 m/s, exchange current density of 50 times the reference value, ASSA

of 10^5 m^{-1}, catalyst thickness of 200 nm, and GDL thickness of 300 μm optimize the performance of the integrated PEC device. Similar trends are observed at other irradiation concentrations, however, the exact nature of the curve varies slightly.
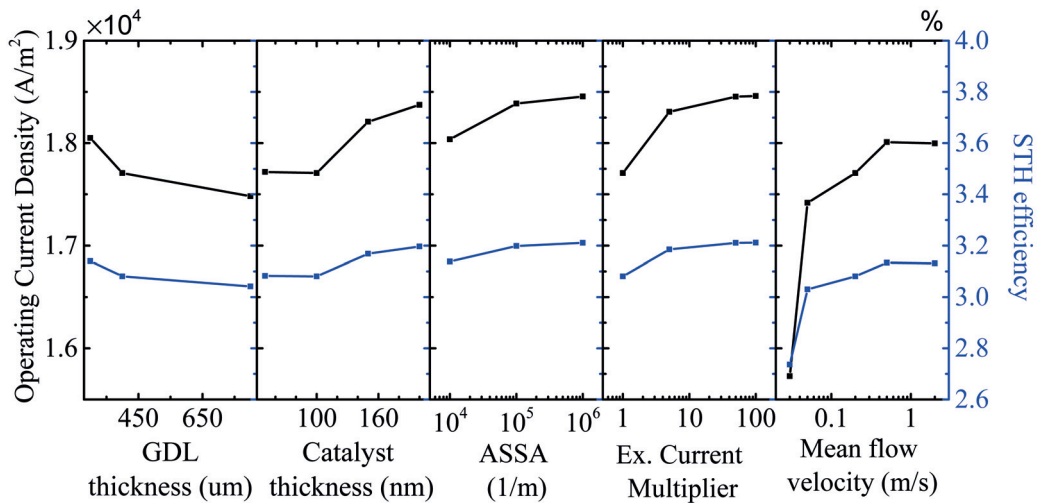
Fig. 2.14 Operating current density (left *y*-axis) and STH efficiency (right *y*-axis) as a function of GDL thickness, catalyst thickness, active specific surface area, exchange current density multiplier, and mean flow velocity, for the reference case I at *C* = 707.

<table>
<tr><td>2.4</td><td></td></tr>
</table>

2.4 Conclusion

The coupled 2-dimensional, non-isothermal multi-physics model [78] is utilized to simulate the performance of an integrated PEC device utilizing concentrated irradiation. The model accounts for concentrated solar irradiation, electromagnetic wave propagation, semiconductor charge generation and transport, heat transfer, fluid flow, mass transport, electrolyte and electrode charge transport, and electrochemical reactions. Operation at large irradiation concentrations allows maximized hydrogen generation rates and increases the economic competitiveness of devices. The low fill factor of the PV cell and mass transport limitations of the electrochemical system put an upper limit on operating current for PV and EC area-matched devices, indicating an optimal irradiation concentration.

The J-V curves of the EC, with varying mass flow rates, intersect in a small potential region, giving rise to two distinct regions of operation. Region I, corresponding to a low operating current density zone, is affected by temperature effects, leading to increasing slopes of the J-V curves of the EC for smaller temperatures. Region II, corresponding to a large operating current density zone, is characterized by mass transport limitations which lead to increased saturation currents of the EC with increasing mass flow rates. The formation of these two characteristic operational regions leads to trend reversals in the objective functions of STH efficiency and H_2 production when increasing the irradiation concentration. For any C, H_2 production and STH efficiency behave independent of the mass flow rate for mean flow velocities above 0.2 m/s. The maximum hydrogen production is achieved at C = 700-1000 and mean flow velocities between 0.1-2 m/s. The maximum STH efficiency is observed at C = 1-30 and doesn't depend on the mass flow rate. The tradeoff between STH efficiency and H_2 production forms a Pareto front. This front consists of device configurations with the largest mean flow velocity. The effective cooling provided by the water channel on the top of the PV, with a mass flow rate of 40/g/s/m (equals a velocity of 0.2 m/s), is found to be optimal at all irradiation concentrations. Large water mass flow rates help in alleviating mass transport limitation and have better cooling capability than smaller rates.

Hydrogen production and STH efficiency increase for more active catalysts, i.e. increased exchange current density and active specific surface area (ASSA), at a particular C. H_2 production is maximized at large C while STH efficiency is maximized at small C. Consequently, a Pareto front exists which consists of cases with large exchange current density and large ASSA. Interestingly, at low and very large concentrations, the ASSA and exchange current density do not influence the performance, therefore the device performance is independent of any choice of catalyst substrate.

The membrane thickness is important for the performance of the integrated device, as its variation leads to significant changes in the operating points. The mass transport limitations are instigated earlier with increased membrane thickness, leading to reduced saturation currents. The large changes in operating current density with varying membrane thickness lead to significant changes in the EC and PV heat sources. However, the water mass flow rate ensures proper device cooling resulting in small temperature variations (a few Kelvin only). These minimal temperature variations, despite significant increases in heat sources, indicate functioning thermal management for the device. The largest H_2 production occurs at largest C and thinnest membranes, whereas the maximum STH efficiency is observed at smaller concentrations ($C \leq 200$), and is found to be independent of membrane's thickness. The objective functions of H_2 production and STH efficiency form a Pareto front which consists mainly of the cases with the thinnest membrane. The other dimensional properties, GDL and catalyst thicknesses, do not lead to significant changes in the operating point with parameter variations. The heat sources, and hence temperature, are found to be quite insensitive to these parameters. The Pareto front for these two cases consists mainly of the thinnest GDL and thicker catalyst.

The two objective functions show a saturating trend with increasing dimensional, operational, and material parameters. Mean flow velocity of 0.2 m/s (40/g/s/m), exchange current density of 50 times the standard value, ASSA of $10^5 \, m^{-1}$, catalyst thickness of 200 nm, and GDL thickness of 300 μm were observed to be the optimum values for enhanced performance of the integrated PEC device for $C = 707$. Similar values are observed for other irradiation concentration factors.

The 2-dimensional coupled multi-physics model proves to be a valuable tool for the design of CIPEC devices working at elevated temperatures and highlights that smart thermal management assists in achieving efficient and low-cost production of solar fuel at large rates. The results predict that thermal management can be used as a cost-effective and simple way of controlling device performance. For example, it is predicted that performance reduction due to degradation over the lifetime of the system can be controlled and counteracted by smart thermal management strategies: For operation at $C = 707$, a 12% degradation in STH efficiency can be compensated by a seven-fold increase in the water mass flow rate. This benefit is observed for the operational region I and II, although the strategy reverses depending on the region. The results illustrate that smart thermal management – which is possible due to the integrated nature of the device design – allows for the development of CIPEC device operation, helps in the design of systems with prolonged high performance, ensures a performance advantage of integrated devices, and indicates that dedicated design and operation can circumvent limitations imposed by primary materials.

Controlling strategies[3]

3.1 Introduction

One viable route to have continuous and stable production from electrochemical systems exposed to sustained and fluctuating disturbances is to have a dynamic control of the operating parameters. The increasing efforts of integrating components in working photoelectrochemical devices for the generation of fuels [68], [69], [79]–[82], [77], [83]–[86], particularly hydrogen, helps in moving closer towards a commercial realization of these approaches. The practical implementation of such devices requires high operating current densities while maintaining high efficiencies. Equally important, the device needs to ensure stable, reliable, durable and robust operation. This implies that the instantaneous operating point shouldn't considerably deviate from the designed operating point. However, this is unrealistic for a practical device given unavoidable degradation phenomena [15] and the irradiation variation, both occurring at different rates and frequencies during the lifetime of the device.

Given the sun being an intermittent source of energy, the reliability and stability become challenging. The intermittency not only affects the production at a particular time of the day, but it also changes the operating point of the system and accelerates the device degradation. For non-integrated, externally wired photovoltaic (PV) plus electrochemical (EC) devices, power electronics (such as a dc-dc based maximum power point (MPP) tracker) can be interconnected between the PV and EC. However, employing external power electronics adds to the system complexity and to the expenses. Earlier demonstration by Chang et al. [80] has shown the effects of employing external converter/MPP tracker in-order to boost the solar-to-fuel efficiencies by as much as 12%. Though they started with a badly designed/operated photoelectrochemical device which had a large difference between the operating

---

[3] Material from this chapter is in preparation for publication in following article,
S. Tembhurne, S. Haussener, "Controlling strategies for concentrated integrated photoelectrochemical devices exposed to fluctuating or sustained disturbances" (2018)

power and the maximum power delivered by the PV components. This difference was higher than the losses in the external power electronics components, allowing them to boost the device's efficiency.

To get a general insight into the advantage or disadvantage of a dc-dc based MPP for PEC devices, the 0-dimensional model developed by Dumortier et al. [21] is utilized to estimate and compare the performance of integrated PEC devices and externally wired PV plus EC devices with power electronics. The *J-V* characteristics of a range of PVs with varying fill factors FF (obtained by varying the series resistance) and a range of ECs with varying current dilution factors ($F = A_{EC}/A_{PV}$) are shown in Fig. 3.1(a). The PVs are III-V material based triple junction cells and ECs are with Ni/Co_3O_4 catalysts. The PV curves with FFs between 0.60 and 0.91 are shown with different colors, the EC curves for different *F*s are indicated by numbers. The black dots represent the intersection point between the corresponding PV and EC curves and hence the operating point of the integrated device, the color dots (on each EC curve) represent the operating point if a 93% efficient dc-dc based MPP tracker is employed (for respective colored PV curve), and the orange diamonds represent the MPP of the different PV curves.
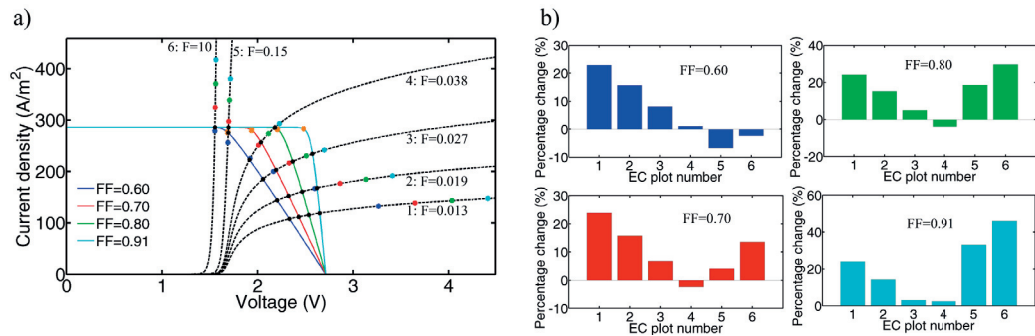
Fig. 3.1 (a) Characteristic current density versus voltage curves of III-V based triple junction PV and Ni/Co_3O_4 based EC for varying FF (0.60, 0.70, 0.80, 0.91) and varying $F = A_{EC}/A_{PV}$ factors (0.013, 0.019, 0.027, 0.038, 0.15, 10). The black dots represent the intersections between the PV and EC curves, the colored dots (on each EC curve) represent the operating point if a 93% efficient dc-dc based MPP tracker is employed (for the respective colored PV curve), and the orange diamonds represent the MPP of the different PV curves. (b) Relative change in the efficiency between a device utilizing an external dc-dc based MPP tracker and an integrated (no-converter) device for each PV case (FF = 0.60, 0.70, 0.80, 0.91) and its corresponding EC curves (curves 1 to 6 correspond to *F* = 0.013 to 10). Positive bars imply the integrated case has a lower efficiency and vice versa.

It is observed that if the corresponding color dot lied vertically below the respective integrated mode's operation point, then the power electronics were not enhancing the efficiency, even though the integrated device was not operating exactly at (but close to) the MPP. The opposite (dc-dc enhances efficiency) is true when the color dot lied above the respective integrated mode's operation point (which lied far away from MPP). The motivation behind analyzing such a wide spread of PVs and ECs is to simulate cases where the integrated operating point lies at varying distances from the MPP of the PV. The relative change in the efficiency with the use of power electronics is plotted in the four bar plots of Fig. 3.1(b) (each bar plot for each PV FF case). It is observed that there are some cases (positive bar) where power electronics enhance the devices' efficiency while for others (negative bar) the use of power electronics causes the device efficiency to decrease. Depending on the distance of the operating point form the respective PV's MPP, the enhancement can be as high as +46% (i.e. for the EC with $F = 10$ and the PV with FF = 0.91) and as low as -7% (i.e. for the EC with $F = 0.15$ and the PV curve with FF = 0.60). Overall, in most cases (though badly designed) the external dc-dc converter seemed to benefit the overall device performance.

This said, the use of power electronics generally requires a non-integrated (PV plus EC) PEC device, for which close thermal and electronic integration is not possible. In order to take benefit of the integrated nature of the device [75], one will have to find ways of adapting and tracking the optimal operating point without the use of external power electronics. This novelty is addressed here.

Designing an integrated device which can dynamically respond to changes in the operating conditions without external power electronics, requires a design providing controllable and adjustable operation. A detailed multi-physics model is required to properly scout for operational parameters which can be controlled/varied, ultimately allowing the changing of the device's operating point. For this purpose, our previously developed fully automated coupled 2D multi-physics non-isothermal model [78] is used, which uses finite element and finite volume methods to predict the performance of the concentrated integrated PEC (CIPEC) devices. The parametric analysis presented in Tembhurne et al. [75] studied the effect of operational parameters such as the flow rate of the reactant and the input irradiation concentration along with variation in materials and dimensional parameters. It has been observed in this detailed coupled analysis that with varying mass flow rates the characteristic J-V curves of the EC component intersected in a small potential region giving rise to two characteristic operating zones, I and II. The zone I, occurring at low to intermediate electrochemical current densities is characterized by the temperature effects where the higher EC temperature leads to lower overpotentials and hence better performance. However, the zone II (occurring at intermediate to

high electrochemical current densities) is dominated by the mass transport limitations which causes lower overpotentials at higher flow rates. This competing behavior in the zone I and II is interesting and in fact, as the device's input irradiation concentration changes (increases) the operating point of the integrated system is found to shift from one zone to another. This behavior makes the reactant mass flow rate to be the perfect parameter to be controlled to track the optimum operating point of the device. This was further supported by observing that a Pareto front was formed for the objective functions of solar-to-hydrogen efficiency and hydrogen production rate. This implies that both these objective functions cannot be maximized at a single reactant flow rate, hence, motivating smart flow rate control. In this chapter, proof and exploitation of this observation and quantification of the benefit is presented. To summarize, three types (see Fig. 3.2(b)) of photoelectrochemical devices i) integrated, ii) non-integrated (PV+EC) with external power electronics control, and iii) integrated with reactant flow control; are analyzed and compared.

Here, focus is on an integrated photoelectrochemical device design for solar fuel generation working under concentrated irradiation and the development of controlling strategies which allow for stable and controllable operation of the device exposed to a variety of disturbances.

The device under consideration consists of a membrane electrode assembly (MEA) sandwiched between gas diffusion layers and bipolar flow plates, which makes the integrated electrolyzer (EC) component. The anodic flow plate incorporates a stage of the dimension of the photovoltaic (PV) component which allows for its direct integration on the plate. The positive contact of the PV is in direct contact with the anode plate and the top-negative contact is connected to the cathode plate via a path made by metal conductors and electrically masked but conducting screws. This device configuration of n-p-anodic-cathodic can alternatively be p-n-cathodic-anodic depending on the designed polarity of the PV component. The design further incorporates a top reactant delivery plate which serves as the inlet for the reactant and which allows the excess heat from the PV component to be removed while preheating the reactant. The reactant is then transferred to the electrochemical component by a direct fluidic connection. The integrated device operates under concentrated irradiation which not only allows to reduce the usage of expensive PV and catalytic materials but also to enhance the device performance by utilizing the normally unused thermal energy. This particular design uses close thermal and electronic integration and allows for the application of thermal management and controlling strategies for ensuring optimal output power. The device design is discussed in more detail in Tembhurne et al. [75], [78], [86] and a schematic is presented in Fig. 3.2.
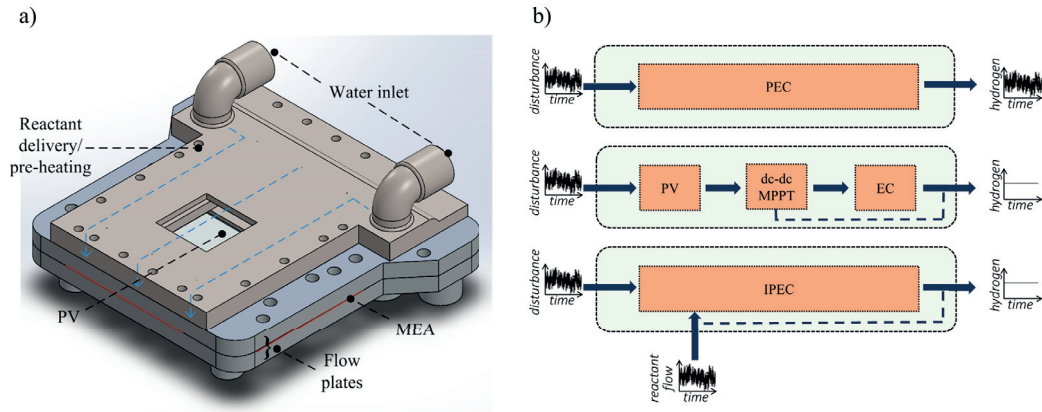
Fig. 3.2 The schematic showing (a) the concentrated integrated photoelectrochemical device with PV, EC (comprised of MEA and flow plates) and top reactant delivery/preheating plate. The blue dotted arrows indicate the flow path of the reactant, i.e. the de-ionized water, which enters the preheating plate through the dual inlets and then passes over and around the PV and fluidically communicates with the anodic plate. (b) Different types of PEC device configurations integrated, PV + EC with dc-dc MPP tracker, and integrated with reactant flow control; are analyzed in this chapter which are schematically presented.

In this chapter, the deployment of the earlier developed 2D multi-physics model [75] to incorporate the degradation modeling is presented, which allows to simulate the close-to-real degradation behavior of the photovoltaic and electrolyzer components. Then the exploitation of the model, for the yearly (sustained disturbances) degradation analysis and daily irradiation variation (frequent disturbances) analysis, is discussed. And finally, the role of the reactant mass flow as an internal optimum power point tracker is presented.

3.2 Methodology

Our previously developed 2-dimensional multi-physics model, presented in Tembhurne et al. [75], [78], served as the basis for the device model. For the electromagnetic wave (EMW) propagation for any complex 2-dimensional geometry, the simulation of the electromagnetic field was done using the combined form of the Maxwell's curl equations [35]. The finite element method was used for this simulation. The net heat source term (Q_{EM}) arising from EMW propagation is detailed in Tembhurne et al. [75] and comprised of the thermalization losses and losses due to absorption of wavelengths above the bandgap wavelength. The sum of the net heat source terms for individual wavelengths gives the overall EM heat source, Q_{EM}.

For the charge transport in the electrolyte, the current conservation and Nernst-Plank equations obeying electro-neutrality were used, whereas Ohm's law was used for the current conservation in the electrode. The Butler-Volmer expression [49] was used to account for the electrochemical reaction at the electrode-electrolyte interface for the anodic oxygen evolution reaction (OER), and cathodic hydrogen evolution reaction (HER). Finite element methods were used for solving the charge conservation equations in the electrode and electrolyte. The fluid flow and mass transport in the channels and the porous gas diffusion layers (GDLs) were modeled by the Navier-Stokes equation with the Darcy extension [50], [51] and species transport by the Maxwell-Stefan diffusion model [52]. The heat source in the electrochemical system (Q_{EC}) [49] comprised of electrode ohmic losses, electrolyte ohmic and kinetic losses, and are detailed in Tembhurne et al. [75].

The Poisson equation and the current conservation equations were solved simultaneously for the charge transport in the semiconductor (SC). Fermi-Dirac statistics and a finite volume solver were utilized where the internal heat source term (Q_{PV}), detailed in Tembhurne et al. [75], comprised of ohmic and recombination losses in the semiconductor.

The steady-state energy conservation equation [54] was solved for heat transfer using finite element methods in order to calculate the temperature field in the IPEC device. $Q_H = Q_{EM} + Q_{PV} + Q_{EC}$ is the total heat source for the integrated PEC which includes the heat from electromagnetic heating, semiconductor transport, and electrochemical reactions.

The material and dimensional characteristics used for the reference case I, with aSi-ucSi-ucSi thin film triple junction ($V_{oc} \sim 2.1V$, $J_{sc} \sim 47$ A/m^2, FF $\sim 64\%$) or reference

case II with $Ga_{0.51}In_{0.49}P$-GaAs dual junction ($V_{oc} \sim 2.35V$, $J_{sc} \sim 100$ A/m², FF $\sim$ 93%) example solar cells, are given in [78] and Table 1.1.

For the degradation analysis to incorporate the degradation phenomena during the lifetime of the device, a reference degradation profile for various components (PV, concentrator, and electrolyzer) was generated based on the earlier work by Dumortier et al. [24], and Fouda-Onana et al. [87], [88]. The concentrator degradation is modeled using $C_{new} = C(1\text{-}0.0065\text{years})$. PV degradation is modeled via an effective concentration received by the PV to be degrading with lifetime as $C_{PV\_new} = C_{new}(1\text{-}0.01\text{years})$ which incorporates both open circuit voltage (V_{oc}) and short circuit current (I_{sc}) degradation. The degradation profiles for the concentrator and PV are presented in Fig. 3.3(a).
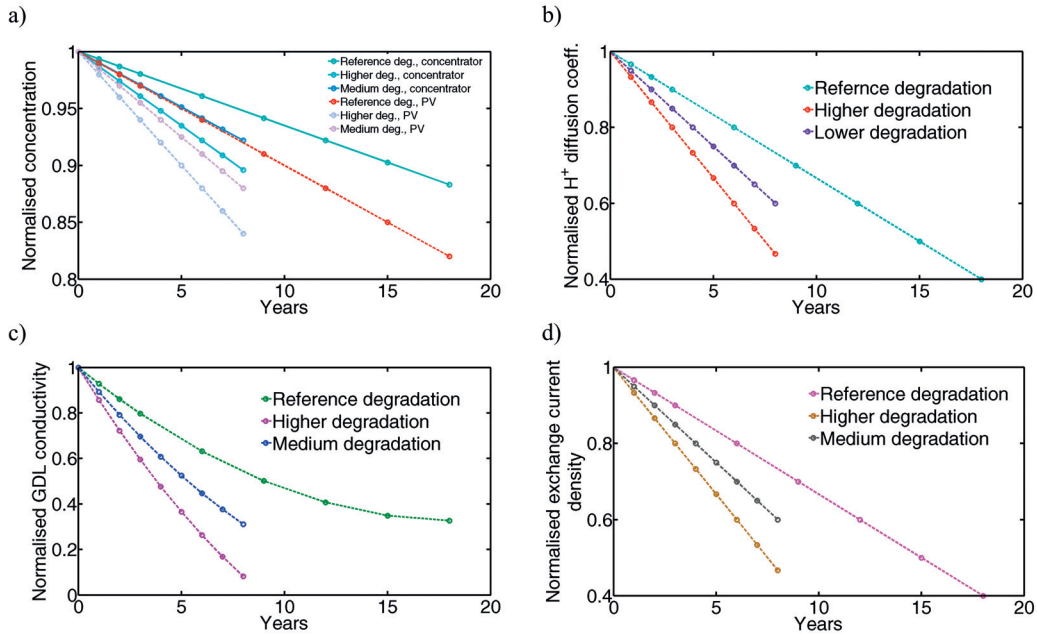
Fig. 3.3 Degradation rate profiles of (a) the effective concentration of the concentrator and of the PV, (b) the H⁺ diffusion coefficient in the electrolyte membrane, (c) the GDL conductivity, and (d) the anode-cathode exchange current densities, for the reference, medium, and high degradation cases.

For the EC component, the report by Fouda-Onana [87] was used to identify the main degradation phenomena and then three parameters from our model were chosen to mimic this degradation behavior. The H⁺ diffusion coefficient in the

electrolyte membrane was used to model the decrease in the EC's saturation current with time. The GDL's conductivity was used to model the increase in ohmic losses and specifically to capture the EC's efficiency losses at high current [87]. The variation of the EC $J\text{-}V$ curves with these parameters is shown in Fig. 3.4. Additionally, the exchange current densities of the anode and cathode (i.e. $IrRuO_2/Pt$) are used to model the increase in the activation over-potential with time. Combining these three parameters, a reference degradation profile, mimicking the realistic degradation behavior occurring in the EC component is generated and is used for the degradation analysis in this study. These three parameters' decrease with time is presented in Fig 3.3 and is given by $J^{ex}_{new} = J^{ex}(1\text{-}0.1years/3)$ (where J^{ex} is the exchange current density of the anode and cathode), $D_{new} = D(1\text{-}0.1years/3)$ (where D is the H^+ diffusion coefficient in the Nafion membrane) and $\sigma^{GDL}_{new} = \sigma^{GDL}(1\text{-}(\text{-}0.002years^2+0.0734years))$ (where σ is the GDL conductivity) for the reference case and these particular trends are chosen to mimic the realistic degradation phenomena presented in [87].
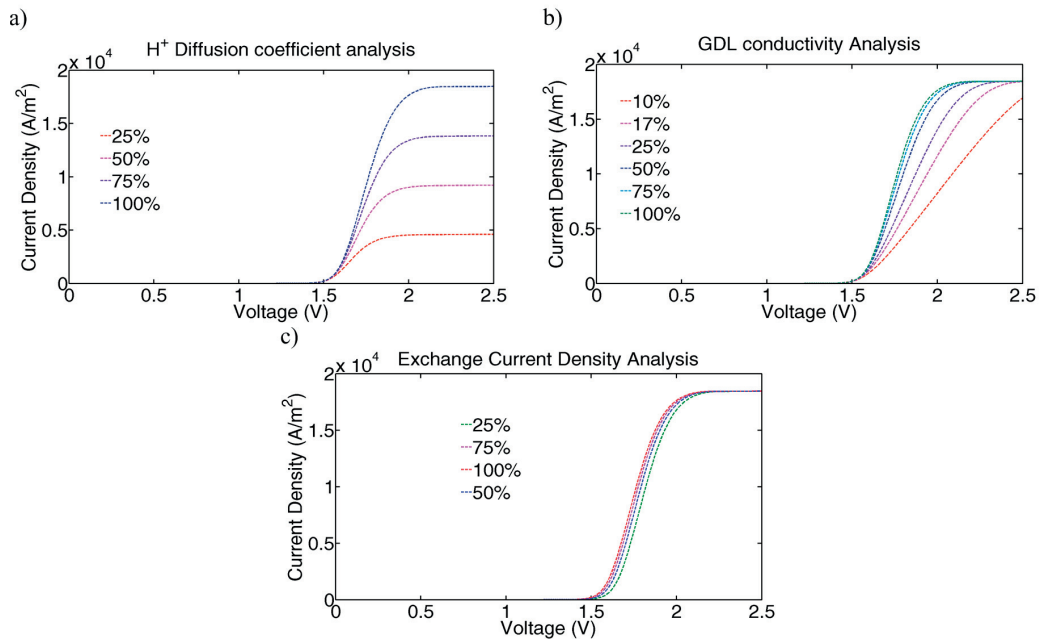
Fig. 3.4 The plot showing the effects of variations of (a) H^+ diffusion coefficient in the electrolyte membrane, (b) Gas diffusion layer (GDL) conductivity, and (c) Anode-Cathode exchange current densities on the $J\text{-}V$ characteristics of the electrolyzer component of the IPEC device.

The reference case degradation profiles of Fig. 3.3 are used for the analysis presented in the chapter, unless otherwise explicitly mentioned. Higher and medium degradation rate analysis are also presented which are based on the degradation profiles presented in Fig. 3.3. For the medium case, the degradation rates are slightly higher and for the higher case, they are significantly higher than the rates for the reference case. Table 3.1 shows the corresponding equations and comparisons between the reference, medium, and higher degradation profiles.

The value of D is $2.4 \cdot 10^{-5}$ [cm^2/s] , σ^{GDL} is 222 [S/m] and J^{ex} are $4.62 \times \exp(-48600/\bar{R}T)$ (anode-IrO$_2$), $142.02 \times \exp(-28900/\bar{R}T)$ (cathode-Pt) [A/m^2] respectively. Entire modeling framework was treated in non-isothermal way where variations of temperature-dependent parameters, coupling between different physical nodes and detailed simulation flow are discussed in Tembhurne et al. [78] and/or chapter 2.

Table 3.1 Description of the reference, medium and higher degradation profiles used for the degradation analysis.

Component Degradation	Degradataion modeling parameter	Parameter's equation	α		
			Reference degradation	Medium degradation	High degradation
Conc. Degradation	Concentration	$C_{new} = C(1-\alpha \cdot 0.0065 \text{ years})$	1	1.5	2
PV Degradation	Concentration	$C_{PV\_new} = C_{new}(1 - \alpha \cdot 0.01 \text{ years})$	1	1.5	2
EC Degradation	H$^+$ diff. coeff.	$D_{new} = D(1 - \alpha \cdot 0.1 \text{ years}/3)$	1	1.5	2
	GDL conductivity	$\sigma^{GDL}_{new} = \sigma^{GDL}(1 - \alpha \cdot (-0.002 \text{ years}^2 + 0.0734 \text{ years}))$	1	1.5	2
	Exchange current density.	$J^{ex}_{new} = J^{ex}(1 - \alpha \cdot 0.1 \text{ years}/3)$	1	1.5	2

3.3 Results and Discussion

Solar to hydrogen efficiency (STH) is defined as $\eta_{\text{STH}} = \dfrac{J_{\text{op}} \cdot E_{\text{eq}}^0}{C \cdot I_{\text{in}}}$, where Faradaic efficiencies of 1 and a negligible product crossover are assumed and where E_{eq}^0 is the equilibrium potential for neutral pH, $T = 25\,^{\circ}\text{C}$, and pressure of 1 atm and has the value 1.23 V. J_{op} [A/m^2] is the operating current density, C is the operating irradiation concentration and I_{in} [W/m^2] is the incident irradiation.

The results and discussions for sustained disturbances (lifetime degradation) analysis, frequent disturbances (daily and seasonal irradiation variation) analysis and the mass flow rate based control of the optimum power point of the IPEC are presented. The analysis presented here is for aSi-ucSi-ucSi triple junction Si PV based integrated photoelectrochemical device with $F\,(A_{\text{EC}}/A_{\text{PV}}) = 1$ unless stated otherwise.

3.3.1 Sustained disturbances: Example-degradation The device designed to operate at a particular operating point at the start of the life doesn't always operate at that designated point. In fact, the operating point changes as the different components degrade with time. For an IPEC device, the operating point is decided by the intersection of the photovoltaic and electrochemical component's *I-V* curves, i.e. where the potential provided by the PV can overcome all overpotentials in EC for the given current. A conservative approach could consist of designing the device in a way that it initially operates way inside the plateau region of the PV's *I-V*. This provides sufficient extra potential which can be accessed with the increasing operating potential given by the degradation and increased overpotentials. If the FF is high and the shunt resistance is not increasing with degradation, the performance will not significantly drop even when the overpotentials increase unless and until the operational voltage pushes above the voltage of the maximum power point (MPP). However to fully utilize the power achievable from the PV component for the EC component, one should design the device to operate at the MPP. And for these devices, it becomes extremely important that their performance is maintained, independent of the degree of degradation, as their operating point lies just on top of the falling edge of the PV's *I-V* curve. Here, a novel controlling approach for such devices is presented. This approach is based on (and only) the reactant flow rate in order to maintain, stabilize and optimise their performance.

The reference degradation profiles discussed earlier in section 3.2, are used for this analysis. The characteristics of the EC and PV components were simulated for operational years between 0 and 18. The Fig. 3.6(a) shows the *J-V* curves for the EC and PV components for increasing operational time and for a water inlet mass flow

velocity of 0.2 m/s. The irradiation concentration was $C = 450$. The J_{sc} and V_{oc} of the PV component decrease with degradation and operational years. The EC's saturation current decreases while the activation overpotentials and the ohmic losses increase. As discussed in detail in chapter 2 and alternatively in Tembhurne et al. [75], the variations of the mass flow rate of water cause the J-V curves of the EC to intersect in a small potential region which gives rise to two characteristic regions of operation, region I and II. These two distinctive zones and their formation is shown in Figs. 3.5(a)-(b) which shows the J-V curves for varying water flow velocities for aSi-ucSi-ucSi and GaInP-GaAs based devices.
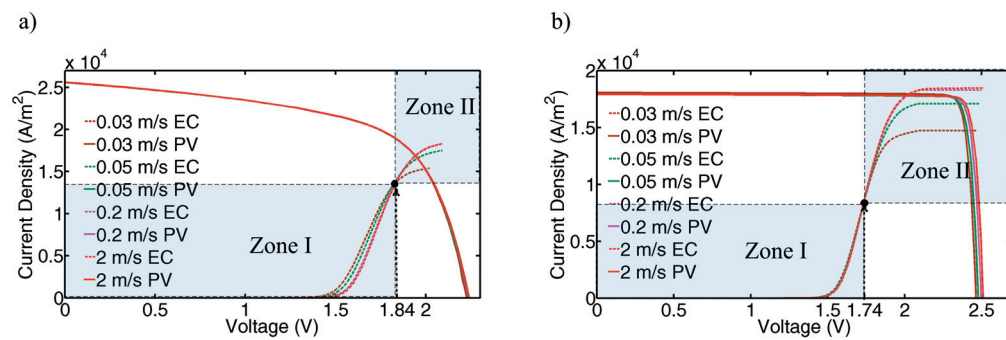
Fig. 3.5 The characteristic J-V curves for (a) aSi-ucSi-ucSi triple junction thin film Si based ($C = 450$), and (b) GaInP-GaAs dual junction III-V based ($C = 180$) integrated photoelectrochemical devices, with varying flow velocities of the water. The black dots show the intersection region of the EC curves, left of which lies the operating Zone I and right of which lies the operating Zone II.

For flow velocities below 0.2 m/s, one can see a noticeable difference in the temperature of the EC component of the device. Due to the higher temperature at low flow velocities, the J-V curves shift to left with decreasing flow rates leading to decreased overpotentials. However, zone II is not governed by the temperature effect but in turn by the mass transport limitation which is alleviated at higher flow rates. This causes the EC's saturation current to increase at high flow rates- a trend opposite than the one observed in zone I.

Figs. 3.6(b) and (c) show that when the water flow velocity is changed the performance of the device can be altered, in fact, a smart control of flow velocity allows noticeable performance enhancements. To understand the effects of the water flow rate control on the degradation alleviation, characteristic curves for 0.03 m/s and 0.2 m/s on top of each other are plotted; the zoomed plot is shown in Fig

3.6(b). At the start of the operation of the device, the operating points for both 0.03 m/s and 0.2 m/s lie in the operational zone II (refer Fig. 3.5).
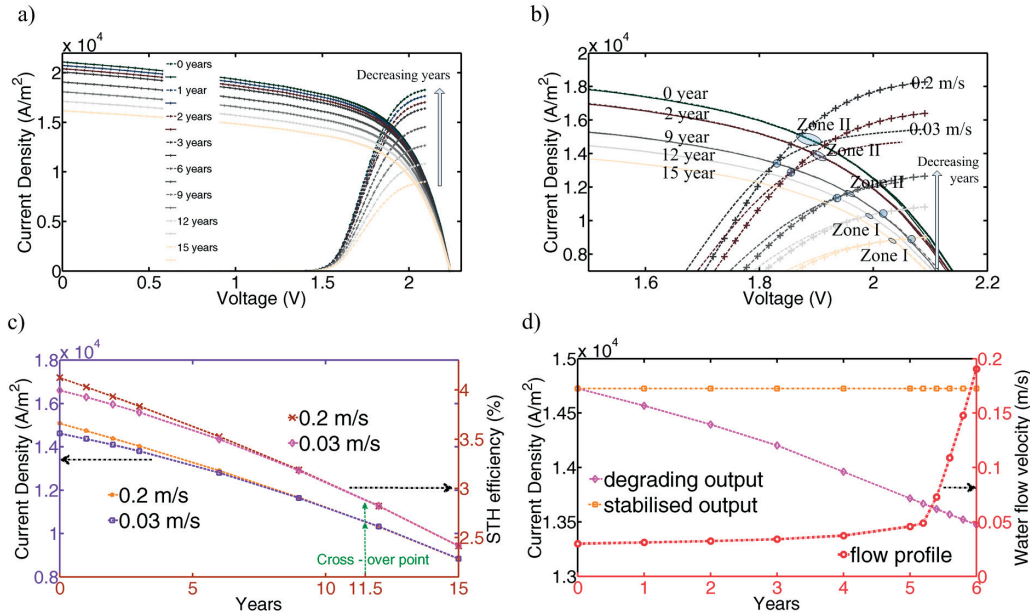
Fig. 3.6 (a) The characteristic *J-V* curves of the triple junction thin film Si triple junction based IPEC device (reference case I) at *C* = 450 for 0.2 m/s water flow inlet velocity and for different operational times. (b) Zoom into figure a) and with the EC component at 0.03 m/s inlet velocity (dotted line), visualizing the overlap between the 0.03 m/s and 0.2 m/s cases. (c) Variation of current density (left *y*-axis) and STH efficiency (right *y*-axis) with operational time for two different water flow inlet velocities. (d) Current density as a function of operational time with constant water flow inlet velocity of 0.3 m/s (pink line) and with varying water flow inlet velocity (yellow line) with respect to flow velocity profile (red, right *y*-axis) for III-V dual junction PV based IPEC device (reference case II) working at *C* = 180.

Two important observations are made in Fig. 3.6(b) as one goes to later operational years: *i*) the benefit of switching from one water flow rate to another (in this case going to higher flow velocity) keeps on decreasing with increasing operational year and degradation (shown by the decreasing size of the blue ellipse), and *ii*) with time the operational zone (shown by the blue ellipse) gets closer and closer to the crossover point of the EC (shown with the blue circle). After around 11 years (in this particular case) the operating points shift and lie in zone I. Both *i*) and *ii*) lead to this interesting device performance behavior. The variation of η_{STH} with time for the

two water flow velocities is shown in Fig. 3.6(c). The initial advantage of choosing a higher flow velocity soon starts diminishing and after ~11 years it is no longer beneficial to operate at a flow velocity of 0.2 m/s, instead, the device should be operated at 0.03 m/s. A similar trend is observed for the H_2 production depicted by the operating current density plotted in Fig. 3.6(c). The cross-over point depends on the device's material and operational choices. For example, the plots shown in Figs. 3.7(b) and 3.8(a) for the variation of η_{STH} with operational time for the GaInP-GaAs dual junction III-V PV based IPEC (reference case II) at $C = 180$ uncover that there is no crossover for the STH curves for the two water flow rates. This is because the operating points for this III-V based PV case always lie in operational zone II [75].

For the aSi-ucSi-ucSi based case the STH efficiency/operating current density curves for the high and low water flow velocities cross over after ~ 11 years. However, for the GaInP-GaAs based case, the crossover never happens due to no-shift of the location of the operating points as they always lie in operational zone II. This is evident from Fig. 3.7(a) where it is seen that the operating points never cross over to the other side of the zonal intersection point (black dot). However, for both the cases the distance between the two flow rate curves decreases (comparison showed in Fig. 3.7(b)) with time indicating the diminishing benefits of operating at a higher flow rate.
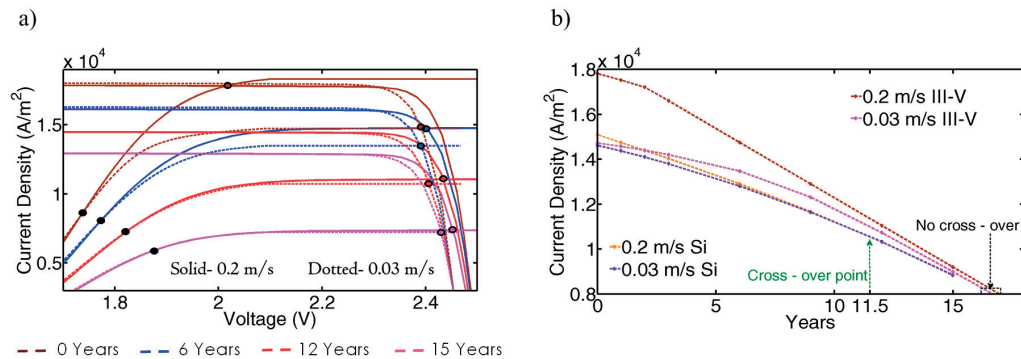
Fig. 3.7 The plots showing (a) characteristics curves for GaInP-GaAs dual junction PV based IPEC device at $C = 180$ for varying operational years, (b) current density profiles for III-V based device at $C = 180$ and thin film Si based device at $C = 450$ with increasing operational years.

The current density, as well as STH efficiency profiles with operational years for dual junction III-V based IPEC showing no cross-over till 18 years are shown in Fig. 3.8(a).
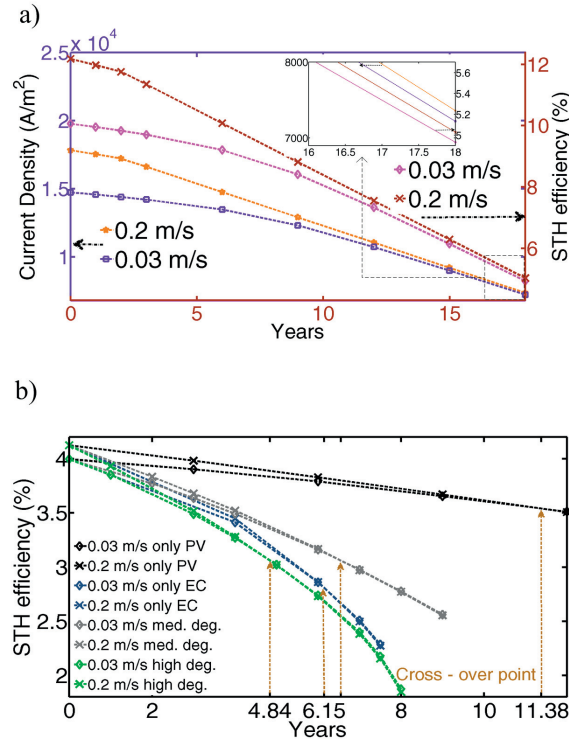
Fig. 3.8 (a) Operating current density (left *y*-axis) with increasing operational years and η_{STH} (right *y*-axis) for GaInP-GaAs dual junction PV based IPEC device (reference case II) at *C* = 180. The inset shows that the two mass flow rate curves never intersect. (b) η_{STH} with increasing operational years for the thin film Si based IPEC device (reference case I) at *C* = 450 for the cases where only PV degradation, only EC degradation, and medium and high degradation rates are considered. The cross-over points (shown by the vertical arrows) for the two flow rates are different for all cases.

Additionally, the points at which the two flow rates result in same operating current density (and STH efficiency) – termed here as the cross-over point – depend on the degradation mechanism and rates. In Fig. 3.8(b) the analysis' results, for the case where only the PV degradation (keeping all other components' degradation to zero) is considered, are shown. It is observed that the cross-over point lies at ~11.4 years. This is explained in Fig. 3.9(a), indicating that the PV's characteristic curves move over a single (nearly overlapping cluster of) EC curves and the cross-over point is decided by the time when the operating points shift from region II to I. A similar analysis has also been performed for the case where only EC component degradation

is taken into account. In Fig. 3.9(b), the shift of the operating points from zone II to I occurs just after 6 years and, hence, for this case the cross-over point lies at ~6.15 years; Very different from the only-PV degrading case. Changing the degradation rates also affects the crossover point. For example, the cross-over point is at 4.84 years for high rates compared to 6.5 years for the medium degradation rates (and ~11 years for the reference). The cross-over point is highly dependent on the degradation behavior and it is of prime importance to know the degradation rates apriori. The detailed knowledge of the degradation helps in better designing and operating the system.
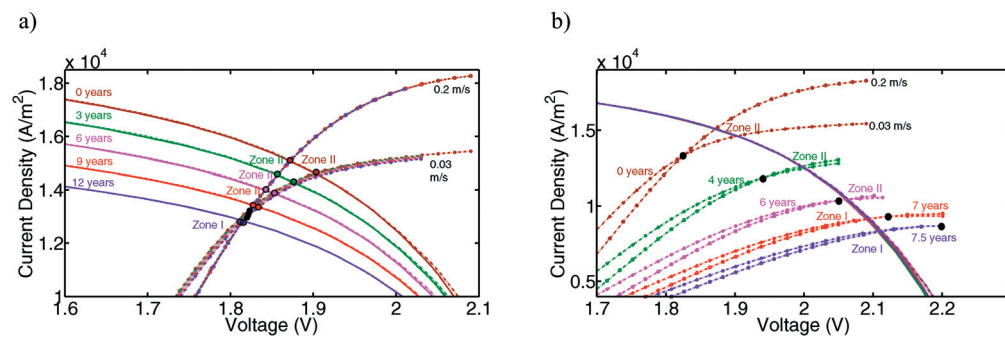
Fig. 3.9 The characteristics *J-V* curves for thin film Si PV based IPEC device (reference case I) at $C = 450$ for varying operational years for (a) the only-PV degradation case, and (b) the only-EC degradation case.

In Fig. 3.9(a) for the PV only degradation case, the EC *J-V* curves for different years more or less overlap on top of each other. Though for 0.03 m/s the noticeable temperature difference of the electrolyzer component still leads to a minimal separation of the *J-V* curves. The intersection points for low and high flow rate EC curves, which decide the demarcation of the zone I and II, are scattered around 1.82 V. All the operating points for the integrated device for the years between 0 to 9 lie on the right side i.e. operational zone II. It is only for the 12th year that the operating points shift to zone I, and this is where the cross-over takes place for the black curves (only-PV degradation case) in Fig. 3.8(b).

For the EC only degradation case, the shift of the operating points from zone II to zone I happens between years 6 and 7 and, hence, the cross-over point shown in Fig. 3.8(b) lies at 6.15 years. When only the EC components are allowed to degrade, the PV curves for varying years all lie on top of each other as shown in Fig. 3.9(b). The EC curves move to lower current densities on the PV curve, and the operating point (shown with black dots) smoothly shift from zone II to zone I.

A water flow rate based control can be deployed to stabilize the output of the IPEC device. Generally, an engineer chooses to design the device to operate at or close to the MPP (using the yearly-averaged irradiation) of the PV component and at the lowest possible water flow rate. For example, for the III-V PV based device (reference case II), an operation at 0.03 m/s water velocity for $C = 180$, and for an average day-light hour irradiation of 800 W/m^2 would result in operation at the MPP of the PV. However, as discussed previously (Fig. 3.7(a)), once the degradation starts, the operating current density of the device decreases.
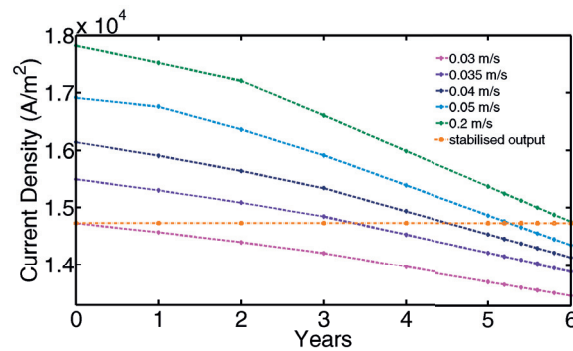
Fig. 3.10 The variation of the operating current density for GaInP-GaAs dual junction PV based IPEC device (reference case II) at C=180 for varying operational years and for different water flow velocities. The orange line shows the stabilised output which could be obtained by changing the water flow velocity.

It is also noted from Fig. 3.7(a) that the operation point of the 0.03 m/s case for the initial operation coincides with the 6 years degraded curves for 0.2 m/s, implying that by varying the flow velocity the initial operating current density for 0.03 m/s can be maintained constant at least for up to 6 years. For finding the appropriate flow controlling profile for stabilizing the output, the output variations for different flow rates for 6 years are plotted in Fig. 3.10. The required stabilized output (orange) curve is then used to find the appropriate flow rate to maintain the same current density. The resulting controlling profile is presented in the Fig. 3.6(d). 2-axis interpolation (current versus years for different flow rates, and current versus flow rates for different years) is used to obtain this controlling flow profile to achieve a stabilized output.

With the flow rate based control, the output production can be kept exactly constant for the 6 consecutive operational years. The controlling profile of the water velocity (red curve) for the decreasing output (pink) curve of the device to achieve a stabilized (orange) output is presented in Fig. 3.6(d). The cumulated hydrogen production for 6 years (apart from being very stable) is increased by 5% with this flow controlling profile. Though, it should also be noted that the case of always operating at maximum flow velocity of 0.2 m/s would lead to 10.1% higher cumulated production for 6 years but it would be a decreasing (not stable) production.

The above-discussed behavior has been experimentally verified with our implemented concentrated integrated photoelectrochemical device (Fig. 3.1, details presented in chapter 4). A 27 W output power IPEC hydrogen generating device is designed, fabricated, implemented and demonstrated at an electrochemical current density of 0.88 A/cm$_{EC}^2$ with an effective irradiation concentration of 474 (Tembhurne et. al. [86]). A thermal analysis has been performed by measuring the device's operating point (potential and output H_2 production flow) for varying input reactant velocities and at different irradiation concentrations. The flow rate is decreased within a reasonable limit so as to still maintain the operating temperatures below 80°C. The water mass flow rate variability analysis has been performed for C = 150 for which a total overpotential drop of 0.25 V was recorded when the flow rates were decreased from 3.8 l/min to 0.34 l/min for which the EC temperature (measured at cathode plate) increased from ~25°C to 60°C. Similar significant overpotential drops were recorded for C = 250 (~0.3 V drop) and C = 411 (~0.4 V drop) when the water flow rates were reduced from 4 l/min to ~0.3 l/min. For these tests, the output hydrogen flow rate was found to be constant, independent of the water flow rate, given by the high FF of the III-V PV based triple junction solar cell component and the sustained location of the operating point in the plateau region of this PV's I-V (V_{oc} = 2.6-3 V for C = 100-400). Thus, it is shown that for a particular concentration and decreasing reactant (DI water) flow rate, the electrochemical component's temperature increased, causing a reduction in the EC components overpotentials' and generally in the device's operating voltage. This demonstration confirms the numerical predictions in terms of I-V trends (shown in Fig. 3.5) and temperature effect domination in zone I. It also confirms the importance of the reactant flow rate as an integral way for thermal management and, in turn, performance optimization parameter.

The degradation analysis highlights that the operational parameter such as input water flow rate plays a significant role in the device's operation. Operational parameters should not be kept constant during the lifetime of the device. In fact, a smart control of the water flow rate allows efficiency as well H_2 production enhancement during the lifetime of the device. For example, operating at an

optimum [75] flow rate of 0.2 m/s, an increase in efficiency between 3-21% is achieved (Figs. 3.6(c) and 3.7(b)) at the start of the operational life of the device. After 6 years of operation, this enhancement decreases to 0.5-9.5% signifying it may no longer be beneficial to deploy extra energy in going to high flow rates. After 11 years and for the aSi-ucSi-ucSi case, it is beneficial to switch to lower flow rates. Generally, water flow based control of the operating point allows achieving very stable output production of the device.

3.3.2 High frequency disturbances: Example-Daily irradiation variation The sun being an intermittent source of energy, the irradiation received during the day is never constant. In fact, the irradiation received at a particular location depends on the sun's path relative to that location, as well as majorly on local weather conditions such as cloud cover. Hence, the optimum operating point during the peak irradiation hour may not be the optimum during the non-peak irradiation hours, implying tracking of the optimum power point during the day is needed. In fact, this can be done with an external dc-dc conversion based maximum power point tracking (as discussed in the introductory section), though deploying extra money and energy for external power electronics may not be a good option compared to our novel water mass flow rate based tracking of the optimum power point. To show the significance of the water flow rate controlling for stabilising the daily production output and efficiency from the system, the characteristic performance curves of the IPEC device are simulated with varying daily irradiation levels (ranging from 20% - 140%, where levels from 20-130% are realistic and 140% is included to account for minor concentrating effects), and are shown in Figs. 3.11(a)-(b). Here an example of the IPEC device is taken which is designed to be working with 0.03 m/s at the start of the life and for which the operating point lies at the MPP of the PV component at an average irradiation of 800 W/m^2.

The *J-V* curves of EC for the 0.03 m/s case show clear separation from each other as the operating temperatures are different for all irradiation levels for this low flow velocity. However, the higher flow velocity of 0.2 m/s ensures proper heat removal making the device temperature independent of the irradiation levels and, hence, no separation of the EC curves is observed. The comparison of the operating current and η_{STH} for the two flow rates depicts the crossover happens after around 80% irradiation level (Fig. 3.11(c)). The operating current increases with increasing irradiation levels, however (Fig. 3.11(c)) η_{STH} decreases (due to the slope in the plateau region of the PV, i.e. the existence of the shunt resistance). The crossover implies that it is beneficial to operate at a lower flow velocity of 0.03 m/s for 0-80% irradiation levels and at 0.2 m/s for the rest of the day.
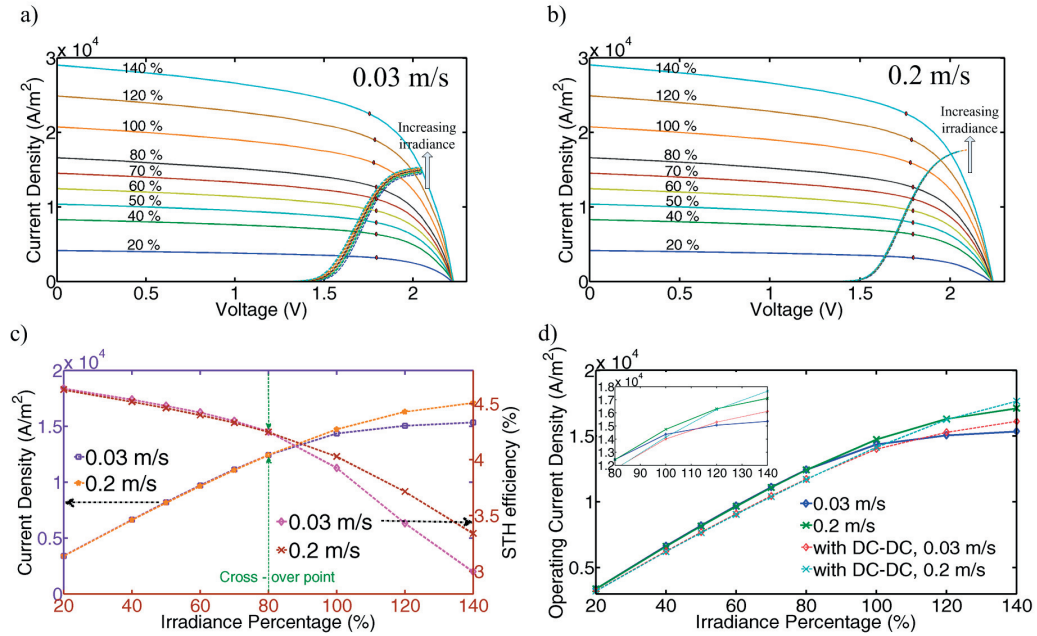
Fig. 3.11 The characteristic *J-V* curves for the thin film Si based IPEC device (reference case I) with varying irradiation levels for (a) 0.03 m/s and (b) 0.2 m/s water flow inlet velocity with $C = 450$ and $F = 1$. The MPP of the PV component is shown by red circles. (c) The variation of operating current density and STH efficiency with irradiation. (d) The operating current density comparisons for non dc-dc and dc-dc based maximum/optimum power point tracker.

If a comparison is to be made among the dc-dc based MPP tracking with overall 93% efficiency and our water flow rate based optimum power point tracking, it is found that the dc-dc based approach underperforms in most of the cases. Fig. 3.11(d) highlights that the operating current density obtained with an external MPPT is always lower (except for >110% irradiation levels) than the output achieved without it. This effect is more pronounced for the cases with low FF PVs (as is for aSi-ucSi-ucSi shown in Fig. 3.11(d)). If the operating power (supplied PV power) is greater than the 93% of the maximum power achievable, the use of an external MPPT is not justified. Only for cases where the integrated operating point lies far away from the MPP (difference >7% of MPP for 93% efficient dc-dc approach), the external MPPT should be used. However, this case is expected to happen rarely in realistic situations and well-designed devices. In fact, the benefits expected for the dc-dc based MPPT (in Fig. 3.11(d) for 0.03 m/s case red (dc-dc) curve is higher than blue curve for >110% irradiation level)) can be obtained with the flow rate control

based tracking (inset of Fig. 3.11(d)) ; that is the green curve for 0.2 m/s case is higher than the MPP tracker (red) for 0.03 m/s. The output hydrogen generation rate maximisation can be achieved more efficiently with internal mass flow controller rather than an external power-electronics (MPPT) component. This shows that the water flow rate control can act as an efficient internal optimum power point tracker. Though it should be noted that the increase of operating current with the flow velocity has a saturating trend [75] and normally the benefits of mass control are limited to the flow rates per length of 40 g/s/m (~ flow velocity of 2 m/s).

To understand the benefits of the water flow rate based controlling approach for a realistic daily irradiation variation, the flow controlling profile to be adopted for different irradiation profiles and the percentage increase as well as stabilizing effect on the device's output is shown in Fig. 3.12.
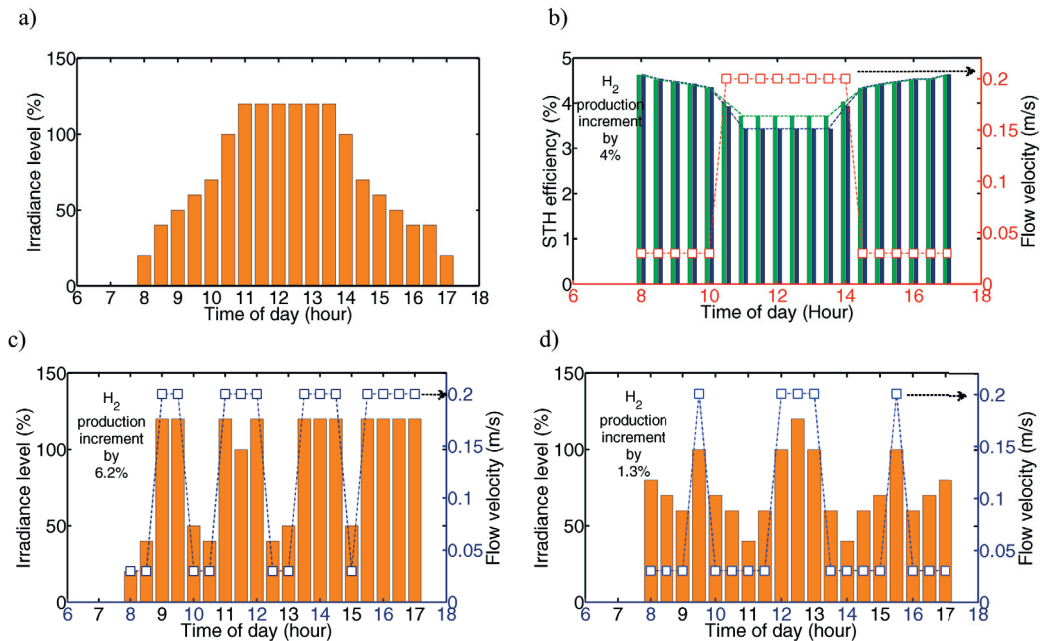
Fig. 3.12 Three different daily irradiation profiles are shown in (a), (c), and (d). (b) Variations in η_{STH} for the irradiation profile (a) for the flow velocities 0.2 m/s (green bars) and 0.03 m/s (blue bars). The respective flow velocity controlling profiles are shown in red for (b) and in blue for (c) and (d) on the right y-axis. The increase in the daily hydrogen production is also indicated.

For the example irradiation profile of Fig. 3.12(a), η_{STH} for 0.2 m/s (green bars) and 0.03 m/s (blue bars) are plotted in Fig. 3.12(b). It can be seen that for the irradiation levels <80% the 0.03 m/s or the blue bars are higher than the green (0.2 m/s) bars. Hence by varying the water flow velocity during the day (as per the profile shown in Fig. 3.12(b), red curve on right y-axis), the efficiency and output is stabilized and a daily increment of 4% in the H_2 production or the average operating current density (increases from 10734 to 11167 A/m^2) is achieved. The increment obtained with the flow rate controlling profile depends on the irradiation profile itself. Two additional examples of daily irradiation profiles are presented in Figs. 3.12(c)-(d) along with the respective best flow velocity variation. The output production increment was as high as 6.2% (Fig. 3.12(c)) and as low as 1.3% (Fig. 3.12(d)). In fact, the benefit is directly proportional to the number of times the irradiation switches from below 80% to above and for how long it stays there. A fully flat irradiation profile (with no variation from under 80% to above) would indicate that flow rate based controlling is of no use, though such irradiation cases are very rare. Additionally, the benefits are smaller (though still noticeable) if the device is already operating at 0.2 m/s rather than the currently assumed operation of 0.03 m/s. It should also be understood that the controlling approach depends on the exact nature of the characteristic curves of the PV and EC components of the device, implying the deciding level of 80% would be different for different material based devices. Hence, it is recommended to conduct this type of analysis before the physical installation of the device and once the material choices are fixed.

3.4 Conclusion

The dynamic controlling of the input parameters (particularly reactant flow rate) in response to the sustained (degradation) and fluctuating (irradiation changes) disturbances for producing a stable, reliable, durable and robust supply of solar fuels, is presented. The deployment of the earlier developed 2-dimensional multi-physics model for photoelectrochemical solar fuel production to further incorporate the realistic degradation phenomena of its various components is discussed. The study focusses on the use of concentrated irradiation for achieving cost-effective efficient hydrogen production. The photoactive and the concentrator components' degradation has been modeled using the effective concentrator factor, whereas the electrochemical component's degradation is realized using the parameter's like diffusion coefficient in the electrolyte, the ohmic conductivity of gas diffusion layers and the exchange current densities of the catalysts. The detailed model proves to be a valuable tool for the design, operation, and optimization of photoelectrochemical devices.

The effect of reactant (water) flow rate in a thermally and electronically integrated photoelectrochemical device has been shown to be paramount in developing device/system operating or controlling strategies which help in efficient operation and degradation effects alleviation. Yearly degradation analysis has been performed showing the need for controlling of operational parameters, particularly the reactant flow rate, rather than keeping them at the same values as designed at the start of the operational life of the device. It is shown that the smart controlling of the flow rate can allow to achieve a very stable output from the device for an elongated period of years despite device degradations. For dual III-V based PEC the degradation in performance of 5% in 6 years has been compensated by deploying water flow rate controlling profile allowing constant output for first 6 years. The benefits of one (higher) flow rate over the other (lower) start decreasing with operational years and after some time there is a reversal suggesting the switchover of the flow rates' benefits. The crossover point (time at which reversal happens) is shown to be dependent on each of the component's degradation rates with high rates causing the fastest reversal. The high output power (27 W) and high efficient (17.2% solar-to-hydrogen) concentrated integrated photoelectrochemical demonstrator has experimentally verified the importance of the reactant flow rate as an integral thermal management and in turn as a performance optimization parameter showing overpotential decrease as high as 0.4 V when the flow rates are changed from 4 l/min to 0.3 l/min for a III-V PV based IPEC.

The controlling approach has also been shown to reduce the effects of daily and seasonal irradiation variations. The method to deduce the flow rate controlling profile which allows the daily output production increment in the range of 1-6% for

exemplary daily irradiations has been presented. The reactant flow rate has been shown to act as an internal power point tracker eliminating the need for external and additional cost inducing dc-dc based power electronic components. In fact, the flow based control allowed better performance than external dc-dc based trackers, and only when the integrated operating power point lied far away (difference greater than 100 minus efficiency of external tracker) from the maximum power point, the use of external trackers was justified.

The periodic operational control of the photoelectrochemical devices proves to be strongly aiding to the efforts of making such devices more efficient and cost-effective as well as being able to supply stably. Reactant mass flow based controller opens new pathways for achieving efficient device operation and degradation alleviation in a more simplistic way.

Experimental Demonstration[4]

Introduction

Functional PEC devices are composed of i) a photoabsorber, that is responsible for solar radiation absorption, and charge generation, separation and transport to the active sites where the electrochemical reactions take place (the photoabsorber is often covered with co-catalyst particles in order to increase the reactions kinetics and selectivity), and ii) an electrolyte that transports the ions between the oxidizing and reducing electrodes, thereby closing the electrical circuit. The most technologically mature and stable PEC design concepts separate the photoabsorber from the electrolyte using conducting (passivation and protection) layers while keeping them in close vicinity to each other (nm to µm range) [69], [89]. As highlighted earlier, these closely integrated device types are called 'integrated photoelectrochemical (IPEC) devices' [21], [75]. This approach allows one to bypass many challenges imposed by the direct semiconductor-electrolyte interfaces present in traditional PEC devices [90], [91]. It additionally omits the losses and lack of thermal integration inherent to completely separated, externally wired (non-integrated) photovoltaic plus electrochemical devices [19], [92].

Increasing the operating current density in IPEC devices reduces the mass and surface area of the active components, and leads to a higher power density. Achieving high conversion efficiency at high operating current densities is challenging due to increased electrochemical overpotentials (reaction related and ohmic losses), and due to increased photoabsorber losses (ohmic losses), and further results in higher wear on the various components. Additionally, high current density operation is usually accompanied by higher temperature operation, inducing losses in the photoabsorber (recombination), as well as the possibility of membrane dry-

---

[4] Material from this chapter is submitted for publication in following article,
S. Tembhurne, F. Nandjou, S. Haussener, "Experimental demonstration of an efficient and scalable integrated photoelectrochemical hydrogen generation device operating under concentrated solar irradiation" (2017)

out (for polymer membrane-based electrolytes), leading to low membrane conductivity.

Concentrating solar irradiation for use in IPEC devices provides a pathway for increasing the current density, resulting in competitive hydrogen generation devices [21], [93]. If high efficiency can be maintained, these concentrated integrated photoelectrochemical (CIPEC) devices can prove to be economically competitive, through incorporating the best performing (though rare or expensive) materials in reduced amounts [21]. Further, because the concentrated photovoltaic sustains operation at much higher current densities than the electrochemical component, a current dilution factor, F (= A_{EC}/A_{PV}), can be introduced, which equals the ratio of catalytic active area to photoactive area. With concentrated irradiation, $F > 1$ allows matching of the difference in the nominal current densities of the photoabsorber to the electrochemical components ($J_{PV} = F \cdot J_{EC}$). $F < 1$ does the same for non-concentrated irradiation and photoabsorber technologies (e.g. thin film Si based photovoltaics). Previous demonstrations of integrated [14], [81] or non-integrated [68], [69], [77], [83], [94] (few also using power electronics [80]) PEC approaches have shown that promising solar-to-fuel conversion efficiencies can be achieved. Some non-integrated demonstrations include systems using multiple in-series-connected photovoltaics (PVs) and electrolyzers (ECs) [68], [94], [95]. However, none of these efforts demonstrated high efficiency while pushing current densities above 0.12 A/cm$_{EC}^2$, with one very recent exception (by Fallisch et al. at 0.80 A/cm$_{EC}^2$). Typical current densities in industrially relevant systems are in the order of 1-2 A/cm$_{EC}^2$. With increasing irradiation concentration one expects, if the electrochemically active area is not changed, an increasing operating current density, however, this is at the expense of significant increases in the over-potentials in the electrochemical component and increasing losses in the PV component. It becomes challenging to design dual or triple junction photovoltaic components which provide the over-potentials required for an operational PEC device [68]. A closely integrated PEC device design, as presented here, provides a unique opportunity to minimize the connection losses, and to optimize heat transfer, surpassing the previous designs in terms of performance. A close electronic integration, as well as smart thermal management with water flow rate-based control, allows the device to operate with high efficiency at high electrochemical current density.

One additional driver for aiming at high operating current densities is economic viability. 0-dimensional PEC device modeling coupled to economic and sustainability analyses have illustrated that devices made of rare materials, and operated at $C > 400$ and $F = 6.86$, are among the most efficient and competitive [21]. A detailed degradation analysis has equally shown that under such conditions, CIPEC devices operate with a reasonable lifetime [15].

For practical implementation, heat transfer and thermal management become essential when concentrating solar irradiation in PECs [22], [96], [97]. 2-dimensional multi-physics modeling has highlighted the feasibility of utilizing concentrated radiation in PEC devices while ensuring high performance [78]. Heat and mass transfer in the CIPEC has been shown to be responsible for the appearance of two competing operational regions [75]: i) thermal effects enhance the performance in the zone of low to intermediate operational current densities, and ii) mass transport limits dominate the zone of high to very high operational current densities (saturation current of the electrochemical component). These competing effects lead to quantifiable tradeoffs between device efficiency and hydrogen evolution rate. It is argued that the operational flexibility of an integrated device by proper heat and mass transport management reduces or counteracts the increasing "mismatch" between the performance of the photovoltaic and electrochemical components with component degradation, allowing effective optimal tracking of the operating point.

The chapter presents the design and fabrication of a fully integrated CIPEC device. Irradiation concentration is used onto the photoabsorber (up to 474 kW/m^2 demonstrated here) to achieve high current densities, combined with current dilution in the electrochemical component ($F = 6.86$) and smart thermal management, to ensure a valuable energy conversion efficiency. The device consists of a "buried" [16] photovoltaic component (dual/triple junction PV) directly integrated onto an anodic flow plate, then covered by a thin reactant channel — acting to remove excess heat and preheat the reactant. The anodic and cathodic flow plates sandwich the electrochemical component comprised of a catalyst coated solid ionic conductor and gas diffusion layers. The design incorporates an electronic conductor for the charge transfer between the photoabsorber and the reaction site, as contrasted with devices designed with an ionic conductor, in order to reduce the overpotentials and to profit from larger conductivities [76]. The device is designed to operate at irradiation concentrations above 1000 kW/m^2.

In the following, a detailed description of the device design, fabrication methods, and techniques and tools used for the characterization is given. Then our device is compared to the previous PEC demonstrations, i.e. benchmarked, in terms of design, solar-to-hydrogen (STH) efficiency, and current density. Finally, detailed test results for efficiency, performance, and stability are presented.

4.2 Experimental methodology

Figure 1 shows the design of the integrated photoelectrochemical device. The device is comprised of a PV component and an EC component in direct contact with each other. The EC component is comprised of a membrane coated with catalysts, gas diffusion layers, and anodic and cathodic flow plates. Table 1 summarizes the properties of the PV component (4 triple junction solar cells arranged in parallel), and the EC component (a polymer electrolyte membrane-electrode assembly with platinized titanium gas diffusion layers and titanium current collectors). The device incorporates a reactant delivery channel assembly on top of the PV component through which the inflowing reactant (water via inlets) and the concentrated solar irradiation (via solar glass) is fed to the device.
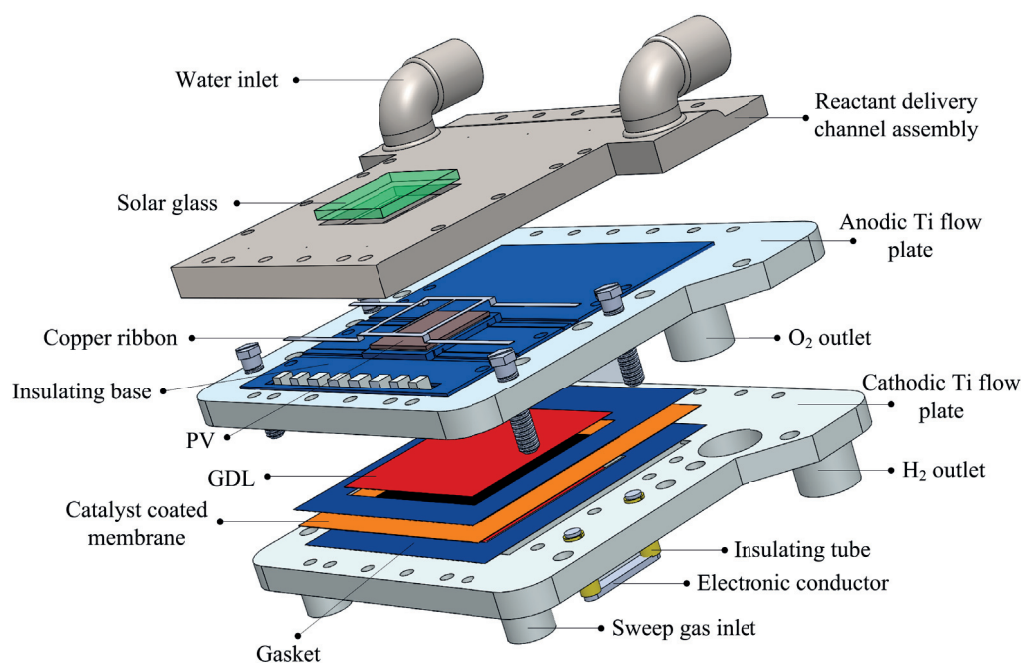
Fig. 4.1 Illustration of the integrated photoelectrochemical device including a reactant delivery channel assembly consisting of a solar glass window, beneath which lies the photoactive component. The photoactive component is in direct contact with the anodic titanium flow/collector plate. The anodic and cathodic titanium plates sandwich the catalyst coated membrane, porous gas diffusion layers, and gaskets, forming the electrochemical component where water splitting takes place. The coolant/reactant enters the delivery channel assembly and directly flows over the photoactive components, removing excess heat and transferring it to the catalytic area.

Table 4.1 summarizes the properties of the photoabsorbing component (4 triple junction solar cells arranged in parallel), and the electrochemical component (a polymer electrolyte membrane-electrode assembly with gas diffusion layers and metal current collectors).

Table 4.1 Properties of the photovoltaic and electrochemical components used for the IPEC device implementation.

Photovoltaic component	Material	InGaP-GaAs-Ge
	Active area (effective)	1 cm^2 (91%)
	Number	4 (in parallel)
	Total surface area (effective)	4 cm^2 (91%)
	Cell open circuit voltage at 500 kW/m^{2*}	3.1 V
	Cell short circuit current at 500 kW/m^{2*}	7.3 A
	Fill factor at 500 kW/m^2 for one cell*	86.5%
Electrochemical component	Type	Proton exchange membrane
	Active area	25 cm^2
	Catalysts (potential at 1 A/cm^2)	IrRuOx/Pt (1.7 V)
	Electrolyte	Nafion$^®$ 115
	Porous transport layers	Platinized titanium screens
	Bipolar plates	Titanium

The 4 cells used to make the photovoltaic component (provided by CESI SpA) are measured by the manufacturer using a Pasan BV-81 AM1.5D concentration cell tester at 25°C temperature and at 500 kW/m^2 irradiation intensity.

The reference PV component is made of triple junction InGaP-InGaAs-Ge cells unless otherwise stated. A dual junction InGaP-InGaAs cell is also used, particularly for the stability testing presented in section 4.2.1. The properties of the dual junction cells are presented in Table 4.2b.

4.2.1 Design, fabrication and stability of the photovoltaic component The PV component incorporated III-V material-based triple junction InGaP-InGaAs-Ge solar cells from CESI SpA. These cells were designed for terrestrial CPV applications and produced with MOCVD technique. They have the polarity of n over p. Our device design included a photoactive area of 4 cm^2, hence 4 cells of 1 cm^2 each in parallel are utilized to prepare our photovoltaic component. A single cell of 4 cm^2 could have also been equally used. Each cell was 10.06 mm in width and 10.92 mm in length, with two 0.4 mm busbars/metal contacts made of silver, and coated with a flash of gold to avoid oxidation.

A 2 mm thick titanium square stage (as can be seen in Fig. 4.1) of dimension 2.2 cm was designed for integrating the photovoltaic component directly on the anodic flow plate. The back side of the four solar cells was conductively glued on the titanium stage using the EPO-TEK H20E-FC epoxy. The top n-side of the solar cells was connected to the cathodic plate via the combination of copper ribbon and electrically masked steel screws. In an earlier version of the device, the four cells were glued on a square copper plate of 2.2 cm edge length, which was then glued on the titanium stage. However, this approach involves using the epoxy twice (between the solar cells and copper plate and between the copper plate and titanium stage) which introduced higher electrical as well as thermal resistances. In order to minimize these losses, design approaches reducing the number of layers of the EPO-TEK epoxy should be used.

The process of conductive glue application is critical as earlier attempts showed increased resistance (in the rage of 0.01-0.02 Ω) between the PV p-type contact and anodic plate leading to large voltage losses (in the range of 0.4-0.8 V at 40A current). The improved attempts comprised of mechanical polishing of the Ti square stage (the surface where solar cells are to be glued) to ensure surface flatness as well removal of any oxide layer. Further a small quantity of EPO-TEK H20E-FC was first applied with a needle on the stage and then spread evenly to make a visibly thin layer on top of which the solar cells were appropriately positioned. This epoxy allows enough working time before it starts solidifying and its curing requires heat treatment in an oven. The solar cells are then gently pressed against the glue layer to ensure full area contact. The EPO-TEK H20E-FC was cured for 90 minutes at 80°C in an electric oven, followed by natural convection cooling for 90 minutes before any further use. The PV cells on the titanium stage were then wire-bonded to each other in order to create the parallel connection. Aluminum wires of 33 µm diameter with wedge-wedge wire bonding technique were used. An example of photovoltaic component (on the copper plate) is shown in Fig. 4.2(a). 60 wires were used for the wire-bonds between the cell-to-cell-horizontal (central busbars) connections, and 24 wires per connection were used between the busbar-to-busbar-vertical connections.

Overall, this allowed a good homogeneity of current distribution over the entire PV component. The most important parameter governing the overall IPEC performance is the number of wire-bonds (or equivalently the resistance) between the PV components and the specially designed copper ribbon. This number was kept at 60 bonds from each external busbar-to-copper and 24 bonds between each central busbar-to-copper, in order to maintain PV-Copper contact resistance below 0.5 mΩ. The prepared PV component on Ti stage with PV-copper wire bonding is shown in Fig. 4.2(b). The copper ribbons (or paths) were 0.5 mm thick and 0.5 cm wide, with an average charge transfer length — from the PV to the cathode's electronic conductor — of 4.6 cm, giving a copper resistance of 0.31 mΩ for each ribbon (out of four).
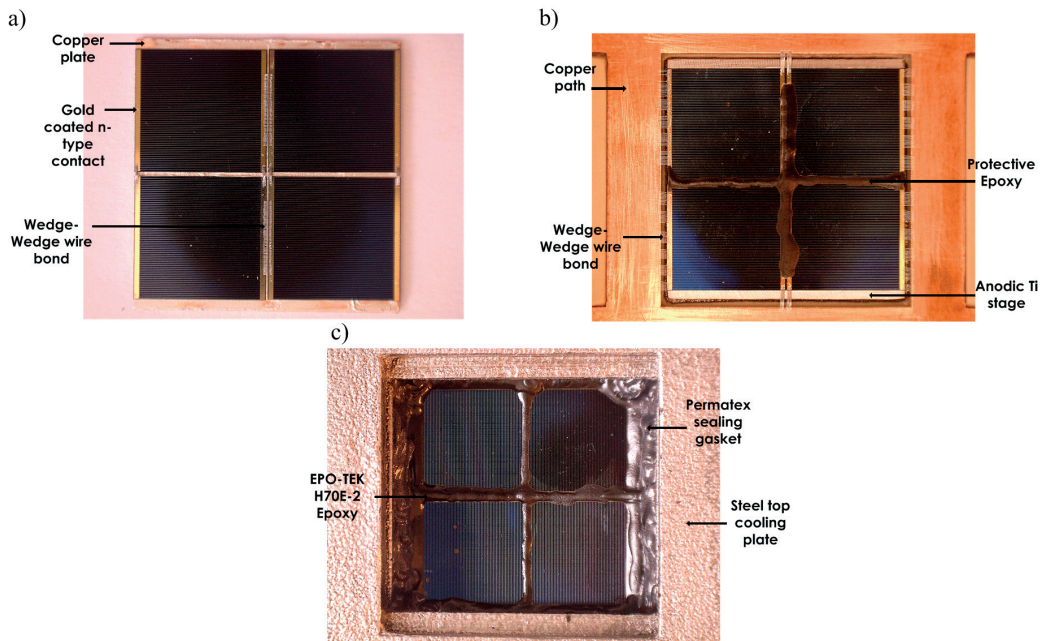
Fig. 4.2 A typical example of the prepared PV component (on the copper plate) with wedge-wedge bonding incorporating aluminum 33 µm diameter wire is shown in (a). The prepared PV component on Ti stage with PV-copper wire bonding is shown in (b). The fully protected module conductively glued on the anodic Ti plate and surrounded with steel cooling plate is shown in (c).

The different stages of PV component preparation of the integrated photoelectrochemical (IPEC) device are presented in Fig. 4.2. The actual irradiated/active area of the photovoltaic component is calculated taking into

account the over-spreading of the epoxy and it is found to be 91% of the designed photoactive (4 cm^2) area. The implemented protected PV component in its final stage is shown in Fig. 4.2(c).

The triple junction (reference case) InGaP-GaAs-Ge and dual junction InGaP-InGaAs cells are provided by CESI SpA, and in the table below the electrical performances of these solar cells are reported. Data were measured using a Pasan BV-81 AM1.5D concentration cell tester at 25°C temperature and at 500 kW/m^2 intensity. All the results presented in this chapter are with respect to the triple junction cell, unless otherwise explicitly mentioned.

Table 4.2a Measured performance parameters of the 4 triple junction InGaP-InGaAs-Ge cells (active area 1 cm^2) used to make the PV component.

Cell no.	I_{sc} [A]	V_{oc} [V]	MPP [W]	I@MPP [A]	V@MPP [V]	FF [%]	Eff. [%]	Mean Irradiation [W/m^2]
1	7.285	3.101	19.58	7.095	2.759	86.64	39.15	500000
2	7.334	3.097	19.56	7.090	2.759	86.14	39.12	500000
3	7.331	3.099	19.56	7.075	2.764	86.07	39.11	500000
4	7.327	3.097	19.55	7.110	2.749	86.14	39.09	500000

Table 4.2b Measured performance parameters of the 4 dual junction InGaP-InGaAs cells (active area 1 cm^2) used to make the PV component for stability testing.

Cell no.	I_{sc} [A]	V_{oc} [V]	MPP [W]	I@MPP [A]	V@MPP [V]	FF [%]	Eff. [%]	Mean Irradiation [W/m^2]
1	7.311	2.681	16.90	7.100	2.380	86.21	33.80	500000.0
2	7.321	2.680	16.89	7.066	2.390	86.07	33.78	500004.5
3	7.339	2.676	16.87	7.105	2.375	85.93	33.75	500002.3
4	7.314	2.678	16.87	7.119	2.370	86.14	33.74	500002.3

An integral part of the thermal management in our design is that the reactant, which is the de-ionized (DI) water in this particular demonstration, flows directly over the bare PV component and is in "fluidic connection" with the anodic channels. This allows the excess heat produced in the PV to be managed, removed, and utilized by

the electrochemical component. The direct contact of the reactant and the PV component potentially enhances degradation, leading to instability in performance. Tests were performed to study the stability of the bare PV component (without any protection) under varying conductivities of DI water. Performance degraded rapidly (~50% reduction in V_{oc} and FF in ~5 minutes) when immersed in DI water with conductivities varied between 0.01-10 µS/cm, higher conductivities sustaining the most severe performance degradation. This resulted from the PV cells' internal resistance (shunt resistance of around 1 MΩ), requiring a lower water conductivity (e.g. ~ 0.0005 uS/cm). Consequently, either the conductivity of the DI water should be extremely low (<0.0005 µS/cm), or the PV's n and p contacts should be protected from direct contact with water. The latter option was adopted using a water resistant epoxy resin EPO-TEK H70E-2 (Fig. 4.2(c)) and thus removed any possibility of leaking current paths. With this protection, the component stability was ensured (see Fig. 4.3). Stable output currents were observed for the PV immersed in DI water (conductivity of 0.01 µS/cm) for more than 9 hours (at a selected voltage bias of 1.55 V) for varying irradiation conditions (on, off, and oscillations with 0.67 Hz). The bias voltage of 1.55 V ensured that the operating point remained close to (but still less than) the maximum power point of 1.7 V.
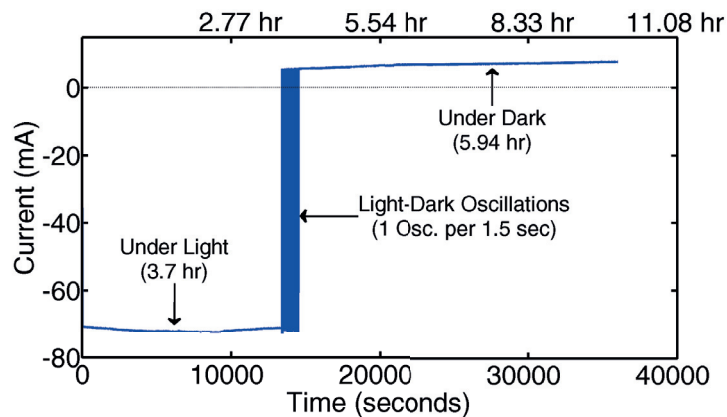
Fig. 4.3 The dual junction PV component's performance under DI water (conductivity 0.01 µS/cm) at a operating voltage of 1.55 V. The PV was exposed to the 1.5 AM solar spectrum (VeraSol-2 LED class AAA solar simulator) with an effective irradiation concentration of 1.5 with on-off light modulation (at an oscillation of 0.67 Hz). The PV component tested here was prepared on top of a ceramic plate.

The stability testing was performed for a dual junction PV component which was prepared on a ceramic plate. The adhesion of the epoxy on the ceramic plate was weaker than on the Ti. This allowed for a small seepage of water from the top of the PV to the back through the epoxy-ceramic interface. The small variation in the stable output current under light was in the range of 1-1.7% around the average value (71.9 mA), and this same variation under dark was in the range of 12-17% around the average value (6.9 mA). This increase in the variation with continued immersion in water was attributed to the leaking of water through the epoxy-ceramic interface. Similar stability was observed when the DI water's conductivity was increased from 0.01 to 10 µS/cm, implying that the removal of any conducting path between the n and p-type contacts of the PV was the only requirement for long-term under-water operation and that the bare exposed surface of the PV cells was not affected by the DI water. However, it should be noted that the EPO-TEK H70E-2 resin used for protection of the wire-bonds and contacts does absorb and retain small quantities of DI water (weight gain of ~0.7% when immersed in water for 10 days). The amount was too small to cause any immediate negative impacts. However, for practical implementation, this might mean that a replacement of the protection after about 2 years of continuous under-water operation might be required, or an alternative protection material or strategy may need to be found.

4.2.2 Design and preparation of electrochemical component The EC is composed of one 25 cm^2 (active area) membrane-electrode-assembly (MEA), sandwiched between two gas diffusion layers (GDL) and two bipolar flow plates (BP). The MEA represents the core of the electrochemical component. It consists of a proton exchange nano-porous solid conductor and semipermeable membrane, coated with catalyst particles on each side. The choice of the solid ionic conductor, i.e. the polymeric electrolyte membrane, allowed for: i) the achievment of very high electrochemical current densities, ii) efficient operation at moderate temperatures (between 40-80°C), and iii) use of a neutral pH reactant in the delivery channel assembly and the reaction channels. The membrane has the function of conducting the protons and separating the produced gases. The catalyst layers catalyze the reactions, transport the electrons and holes to the active sites, and allow the reactant and products to be distributed and evacuated through its porous structure. An MEA from Fuel Cells Etc is used. The proton exchange membrane was a 127 µm thick perfluorosulfonic acid polymer (Nafion® 115) known to have a good proton conductivity, limited gas crossover (therefore ensuring high purity), and good mechanical, chemical, and thermal stability (up to 280°C [98]. In order to limit hydrothermal stresses (exacerbated above 120°C [99]) and to guard against membrane dry out [27], our EC operation is limited to temperatures below 80°C. The anode catalyst coating consisted of iridium-ruthenium oxide nanoparticles, with

a loading of 3 mg/cm² (exchange current density of $\sim 10^{-6}$ A/cm² [100]). This noble-metal oxide was chosen in order to ensure high activity at high current densities because the relatively sluggish kinetics of the OER can be a limiting parameter for the global performance of electrolyzers [101]. This rare material also shows good stability at a high anodic electrical potential and at a low pH, conditions under which non-noble materials typically corrode [102]. The cathode catalyst coating consisted of platinum black, with a loading of 3 mg/cm² (exchange current density of $\sim 10^{-3}$ A/cm² [103]).

GDLs are multifunctional components which guarantee a good electrical connection between the MEA and the BP ribs, ensure a good mass transport of fluids between the BP channels and the MEA, and provide a certain mechanical stability to the MEA. The GDL used in this study for both anode and cathode compartments were ultra-thin (102 μm) platinized titanium screens, provided by Fuel Cell Store. These GDL usually exhibit a good resistance to corrosion and erosion. The titanium screens were platinized in order to avoid their oxidation into titanium oxide at the anode compartment (due to the presence of oxygen), which is known to highly increase the electrical resistance of the cell [61].

BPs have multiple roles: i) they ensure a proper supply of water to the GDL and removal of produced gases via the integrated channels, ii) they act as current collectors and distributors, collecting the charges generated in the PV component, distributing them over the larger area electrolyzer through in-plane conduction, and transferring them to the GDL via the ribs, and iii) they guarantee the mechanical stability and tightness of the device. Additionally, BPs provide a simple way to connect the device to a power supply via a ring style blade connector in order to characterize and test the cell in the isolated electrolyzer mode. The BPs are designed in-house and are 3D printed (3D precision SA). Given that the anode plate is vulnerable to corrosion due to the presence of oxygen and a high operating potential, the plates were made of titanium. For both of the anode and cathode BPs, the flow fields were designed following a straight channel pattern, with rectangular channels having a width of 4 mm and a depth of 5 mm, ribs having a width of 4 mm, with a total thickness of 7 mm.

The components were assembled by positioning the MEA and GDL in the center of the BP. For tightness, Teflon® gaskets (cut following the geometry of the cell by water jet machining) were positioned around the MEA and GDLs and clamped with 8 bolts at a torque of 2 Nm.

The *I-V* characteristics of the typical electrolyzer assembly, measured at a flow rate of 400 ml/min for temperatures between 16-53°C, are presented in Fig. 4.4 (right *y*-

axis). The spread between the curves shows the positive effect of increasing the temperature on the electrolyzer performance in the low current density operational region [78].

It is observed in our previous modeling work [78] that changing the flow rates for the electrolyzer leads to the formation of two distinct regions of operation. Region I is characterized by temperature effects (low flow rates require less over-potential for the same current), and region II is characterized by mass transport limitations (high flow rates require less over-potentials for the same current). Here, this behavior is experimentally confirmed. Mass transport limitations occurred at current densities of 0.5 A/cm^2_{EC} and very low water flow rates of around 50-70 ml/min (*I-V* curves shown in Fig. 4.4, left *y*-axis), while for higher flow rates (1-4 l/min) the mass transport limitations were not observed, even at current densities as high as 2 A/cm^2_{EC} (refer to Fig. 4.12(b) corresponding to a different electrolyzer assembly used for the integrated operation testing).
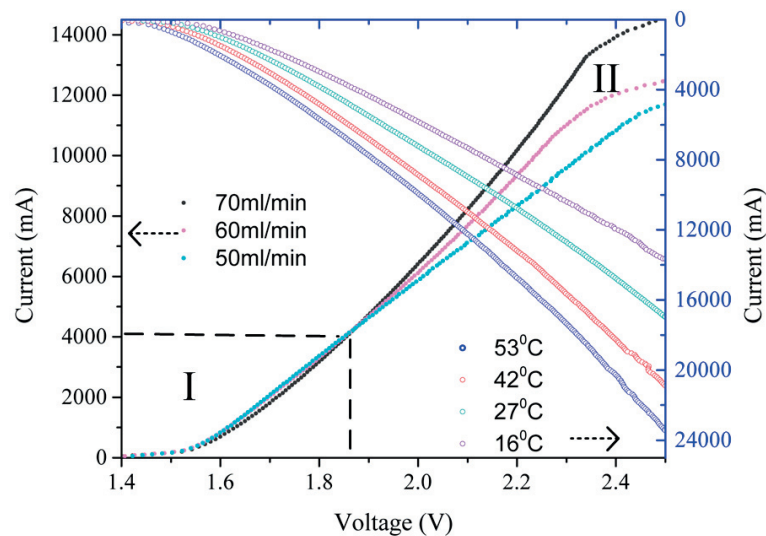
Fig. 4.4 Characteristic I-V curves of a typical electrolyzer assembly measured at 400 ml/min and temperatures varying between 16, 27, 42, and 53°C (right y-axis), and at varying flow rates between 50(19°C)-70(23.5°C) ml/min (left y-axis). The three curves for varying flow rates show the formation of two distinct operating regions (I and II) caused by the intersection of the curves in a small potential region (around 1.87V).

The dynamic response of the EC and the test-bench (discussed in section 4.2.4) is presented in Fig. 4.5(a). It should be noted that measured H_2 mass flow presented in Fig. 4.5 is actually the cathode side output gas stream flow and this flow not only contains H_2 but may also contain small quantities of water vapor (refer to section 4.2.4). An electrolyzer assembly was tested by enforcing varying constant currents of 30, 34, 38, 42, 46 and 50A (equivalently at current densities from 1.2-2 A/cm_{EC}^2) for around 1 min and the resulting output cathode gas stream's flow rate was measured. The blue curve in Fig. 4.5(a) shows the fast response of the EC and test-bench in response to the set current (or equivalently expected mass flow) as per the orange curve. It is noted that the difference between expected and measured mass flow rate increases with increasing operating current density and this is attributed to the increase in the device temperature leading to increased water vapor content in the output gas flow stream. Alternatively, the measured H_2 mass flow (red curve) is plotted in Fig. 4.5(b) for varying operating currents, along with the theoretically expected H_2 mass flow (black curve). This curve is generated while performing the *I-V* sweep (at a current sweep rate of 2 A/min). It is noted that the measured flow is in good agreement with the expected flow with only deviations observed at very low currents (<4 A or <0.16 A/cm_{EC}^2) attributed to small flows at these currents and the accuracy of the flowmeter. Deviations from expected flow rate are also observed at a high current density which is attributed again to the increased temperature and hence increased water vapor content in the output gas flow stream.

a)   b)
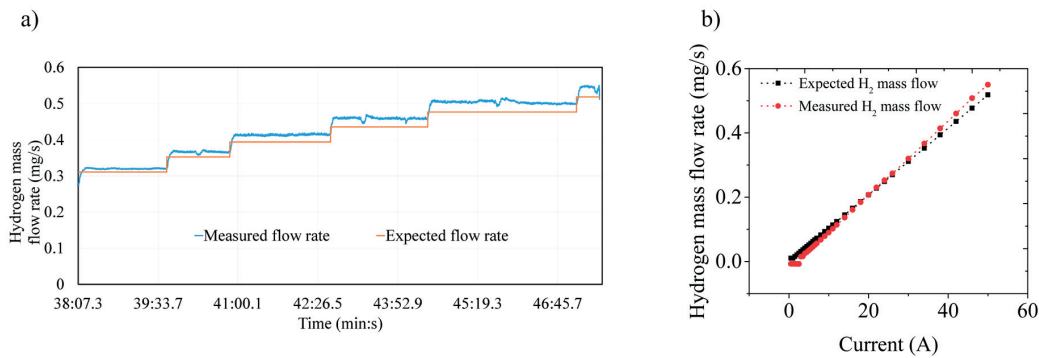
Fig. 4.5 (a) Variation of measured hydrogen mass flow rate with time, during the experiments when EC (in separated mode) is characterized with changing operating currents of 30, 34, 38, 42, 46 and 50 A. The orange curves show the expected mass flow rates theoretically calculated for each current. (b) The plot showing the relation between the measured hydrogen flow rate and the operating current when EC is characterized separately. Furthermore, the black curve shows the theoretically expected mass flow for each current.

4.2.3 Design of the IPEC device As illustrated in Fig. 4.1, the back side of the solar cells is in direct contact with the anodic bipolar plate through a conducting glue. On the n-side, the solar cells are connected in parallel and wire-bonded to the cathode plate through copper ribbons and conductive screws. The electrically conductive screws are cylindrically insulated, allowing charge transport only from the copper ribbons to the cathode plate. The photo-generated holes are transported from the backside of the solar cell to the anode plate, while the photo-generated electrons are transported from the top of the solar cells to the cathode plate.

The solar component is covered with a 3D printed stainless steel plate for cooling and reactant delivery (Fig. 4.1). The plate incorporates rectangular flow channels with the same width as the length of the PV component, fully immersing the PV component in the reactant (i.e. DI water). These channels directly communicate with the anodic channels allowing for the preheated water at the outlet of the plate to directly feed to the EC. The delivery plate is used to convectively remove a large portion of the thermalized energy in the solar cell. The remaining portion is removed by heat conduction to the anodic BP. This thermal management approach limits the operating temperature of the solar cell, which is known to have dramatic impacts on performance [26], [104], and enhances the kinetics of the electrochemical component. The delivery plate has two inlets in order to ensure a homogeneous water distribution and to allow for varying flow rates in the channels.

The radiation absorption in the top water layer is minimal in the absorption range of the photovoltaic component as the layer thickness is only 4 mm [78], [105]. A design variation could arrange the delivery channels around or beneath the PV component and, hence, not disturb the input light. However, the heat transfer is more efficient when the reactant flow is arranged directly on top of the PV [106]–[109].

An insulating layer made of PEEK material was sandwiched between the cooling plate and the anode plate in order to avoid parasitic charge transport to the delivery plate. In addition to the 8 bolts of 4 mm diameter used to tighten the EC plates, 16 more steel screws of 2 mm diameter were used to clamp together the Ti plates along with the top steel cooling plate. This further contributes to the overall tightness of the device. Additionally, Permatex 82180 gasket maker was used to cover the gaps and uneven surfaces which significantly helped in making the device water and gas leakage proof.

A solar glass with a transparency of 0.91 (for 320-1900 nm wavelengths) is mounted in the aperture. This CIPEC device design can be utilized to carry out photoinduced oxidation or reduction of any reactant, not being limited to the photoelectrochemical production of hydrogen. The CIPEC device in its testing stage is shown in Fig. 4.6.
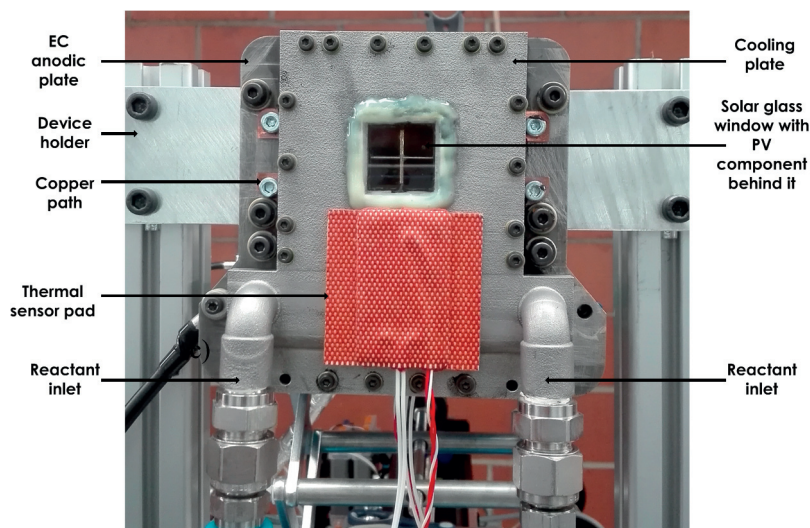
Fig. 4.6 Photo of the fabricated and tested concentrated IPEC device mounted vertically on the test-bench.

4.2.4 Testbench and characterization procedure The process and instrumentation diagram of the test bench used for the photoelectrochemical tests of the device is shown in Fig. 4.7 and implemented test bench is shown in Fig. 4.8(d). The two global inputs of the process are solar irradiation and water. Hydrogen, oxygen, and the over-stoichiometric water were collected at the device outlet. Tap water (at a pressure of about 3 bar) was used as feedstock. The input water flowed through a deionizer (Thermo Fisher Scientific Inc. Ion exchange cartridge DI 2800), reducing the water conductivities to 0.1 μS/cm. The DI water was supplied to the IPEC device at given flow rates, controlled by a programmable peristaltic pump (Baoding Shenchen Precision pump V6-12L/2-YZ35). At the outlet of the device, water traps were used to separate the produced oxygen and hydrogen from liquid water. Even if no water was supplied or produced at the cathode compartment, water was still collected on the cathodic side, since it crossed the membrane during electrolysis operation by molecular diffusion, permeation, and electro-osmotic drag [110]. While the trapped water was automatically drained, the dry gases streams were sent to high accuracy gas flow meters (Natec Sensors GmbH, Gas Mass flowmeter - type M), recording their flow rates. The flow meters also provided information about the temperature and pressure of the produced gases. Check valves were used in order to avoid any backflow from the ambient air towards the system.
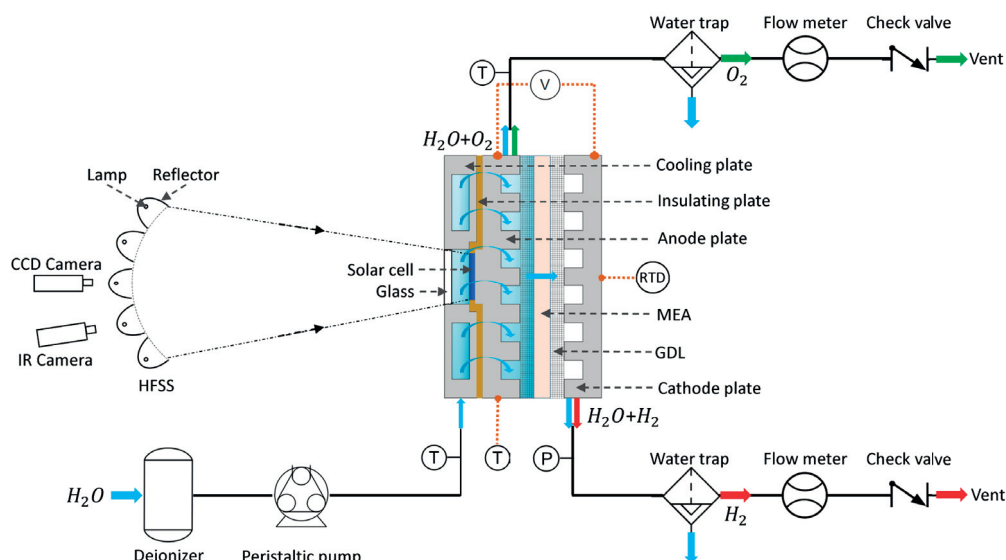
Fig. 4.7 Process and instrumentation diagram of the test bench. The output light of the xenon lamps is reflected from the ellipsoidal reflectors and concentrated on the CIPEC device. DI water flows to the anodic compartment of the device. The over-stoichiometric (anode) or crossed over (cathode) water was trapped/separated from the reaction products (anode: oxygen, cathode: hydrogen). The position of temperature, pressure, voltage, and output gas flow sensors/meter are also indicated.

In order to mimic the concentrated solar irradiation, a 45 kW$_{el}$ multisource high-flux solar simulator (HFSS) was used [111]. It is particularly challenging to demonstrate large PV area based operation at high irradiation concentrations, primarily because, as the active PV area increases it becomes increasingly difficult to have a uniform/homogenous irradiation distribution on the PV area. Our HFSS facility allows the utilization of a tailored combination of its eighteen 2.5 kW$_{el}$ xenon lamps to achieve uniform flux profiles on target areas as large as 4 cm^2. The HFSS comprises of eighteen 2.5 kW$_{el}$ radiation modules which are arranged over the surface of a virtual sphere whose radius is 1933 mm (measured from the lamp position). Each irradiation module is composed of one short-arc xenon lamp, coupled to one reflector (truncated ellipsoidal mirror of high-surface quality). A detailed description of the HFSS can be found in Leveque et al. [111]. A picture of the integrated photoelectrochemical device exposed to the HFSS is shown in Fig. 4.8(b). The spectrum of the lamp plus reflector system is not identical to the ASTM G173-03 AM1.5G solar terrestrial spectrum hence the I_{sc} of the reference III-V cell (measured under AM1.5G spectrum, see Fig. 4.9) was used to calibrate the grayscale

maps obtained with the CCD camera (Basler scA 1400-17 gm, 1.5 MP, 12 bit pixel depth) for varying lamp configurations (giving varying irradiation concentrations) of HFSS. A typical irradiation map in the focal spot at a concentration of 411 is presented in Fig. 4.8(a), confirming high uniformity. The maps for the other irradiation concentrations are shown in section 4.2.5.

For homogeneity purposes, the concentrated irradiation was distributed on an area much larger than the solar cell. In order to protect the zones of the device that were not supposed to be irradiated, an in-house designed protective shield (see Fig. 4.8(b)) was used in front of the device. The protective shield is made up of Aluminium and is also 3D printed (by 3D Precision SA). A square window was provided at the center of the protective shield, in front of the PV component. Given the high irradiation concentrations on the protective shield, it was water cooled.

A network of thermocouples was used to record the inlet and outlet temperatures of water and of the anodic plate. A resistive temperature detector (RTD-PT100) was stuck on the backside of the cathode plate in order to measure operating temperatures inside the cell. A pressure transducer (Omega Engineering, Digital pressure transducer PXM409) was installed at the outlet of the cathode plate, in order to measure the pressure of the produced hydrogen. Both anode and cathode plates were connected to a voltmeter, in order to measure the operating potential of the cell. Gantner Q.bloxx A101 was used as the data acquisition board for thermocouples (along with Omega TC-08). A combination of CCD camera (Basler scA 1400-17 gm, 1.5 MP, 12 bit pixel depth), a Lambertian target, and reference III-V solar cell were used to calibrate the radiative flux distribution before starting the tests. An IR camera (FLIR A655sc) was used to measure the temperature distribution over the surface of the reactor during operation.
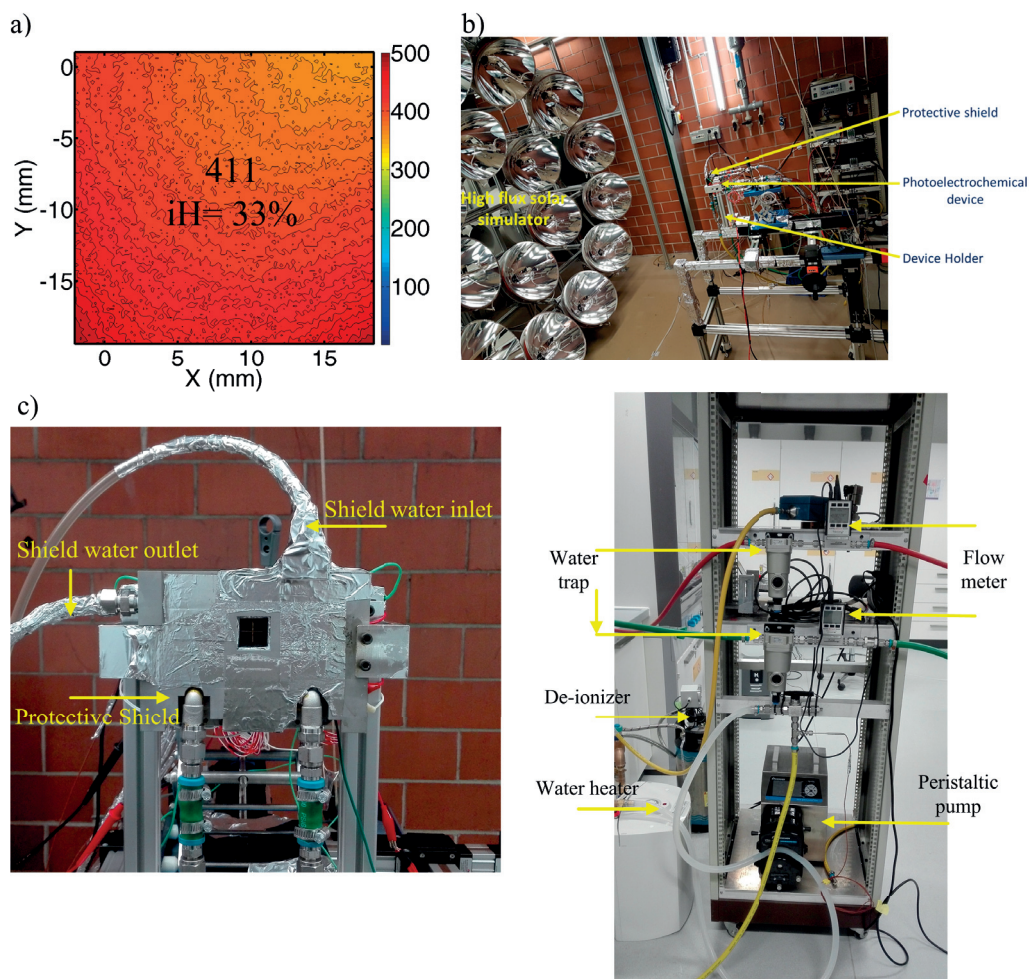
Fig. 4.8 (a) Irradiation flux profile for an average concentration of 411 as received by the IPCE device's photoactive area (20 mm by 20 mm) measured using a combination of Lambertian target, CCD camera and reference III-V PV solar cell for average concentrations of 411. The iH (inhomogeneity) factor (=max-min/avg. conc.) is 33%. (b) Photo of the test bench with the integrated photoelectrochemical device mounted on an adjustable chassis via a device holder. HFSS with its 18 lamps is on the left and the IPEC device on the chassis is on the right side of the photo. The protective shield shown in (c) is used to protect the zones of the devices that are not supposed to be irradiated. Top right corner of the photo (b), has the vertical cabinet housing the power source and loads, water traps, flow-meters, peristaltic pump. The implemented test bench showing different components like flow meters, water traps, peristaltic pump, de-ionizer, water heater (only used for EC testing at varying temperatures) is presented in (d).

For the isolated individual PV and EC characterizations, a high precision potentiostats (BioLogic VSP300 and Biologic HCP-803), a power source (EA-PS 8080-60 DT), and a power load (EL3160-60) were used. A four-point probe method was used for carrying out current versus voltage measurements, particularly at high currents. The effective operating irradiation concentration was defined with respect to the measured short circuit current (I_{sc}) of the reference solar cell. The reference cell was first characterized (see Fig. 4.9) under Wacom WXS-220S-L2 class $A^+A^+A^+$ solar simulator under standard test conditions (AM1.5G, 100 mW/cm^2, 25°C) at CSEM, Neuchatel. The I_{sc} from the reference cell characterization was then used to calibrate the grayscale maps obtained with the CCD camera for varying lamp configurations of the high flux-solar simulator. It should be noted that the short circuit current density for the cell is 140 A/m^2. The flux maps showing the distribution of irradiation on the PV area as well as the average concentration received by the PV are shown in Fig. 4.10.
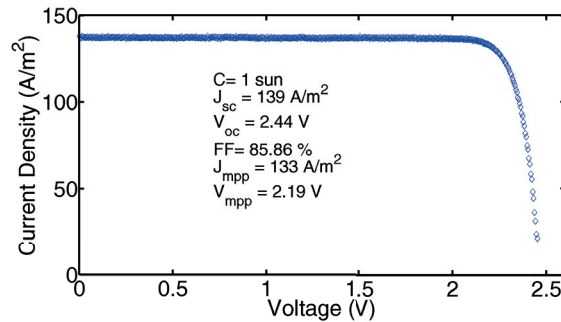
Fig. 4.9 Reference III-V cell characterization curve under 1 sun. (Note: Using Wacom WXS-220S-L2 class $A^+A^+A^+$ solar simulator under standard test conditions (AM1.5G, 100 mW/cm^2, 25°C)).

The testing protocol for the system was as follows: the anode compartment was swept with de-ionized water at room temperature at a constant flow rate of ~ 1 l/min for about 4 hours in order to fully hydrate the Nafion$^\circledR$ membrane. During the last 15 minutes of the hydration period, the cathode compartment was swept with nitrogen at a constant flow rate of 5 mg/s, in order to completely remove all air, specifically the oxygen. At the end of the hydration period, the operating mass flow rate of water was set using the peristaltic pump and the irradiation concentration was progressively increased using the HFSS with a continuous measurement of all relevant parameters (flow rates, temperatures, pressure, and electric potential) through data acquisition boards connected to a computer.

4.2.5 Irradiation flux characterization under HFSS The exact irradiation flux falling at the photo-active area of the device can be measured and visualized using the Lambertian target, CCD camera, and reference III-V cell. The measured flux maps' inhomogeneity can be quantified by defining an inhomogeneity factor, iH. iH is the ratio of the difference between the highest and lowest concentration in the relevant area of the measured profile to the average concentration. The iH for different profiles is less than 33% for higher concentrations and was as low as 10% for lower irradiation concentration. It should be noted that even better homogeneity configurations (iH <10% for C = 411) can be chosen, though, this would require centering the IPEC device to a different in-plane location (each time for each concentration change). Figure 4.10 shows the flux profiles for various concentrations. It should also be noted that for an average concentration of 474 (Fig. 4.10(j)), the inhomogeneity is very high (iH = 88%). This high inhomogeneity is detrimental to the device, the device at this concentration and with this flux map showed physical damage as the solar glass as well as its supporting epoxy glue on the left bottom corner broke after ~3 minutes of operation. The breakage at left bottom corner is aligning with the flux map and its local hot spot at that position.

It should be noted that the operation at higher concentrations (i.e. >474) is not limited by the device itself but by the current setup of the high flux solar simulator (HFSS). In fact, the 18 lamps of our HFSS can be individually positioned to achieve more homogenous flux maps even at concentrations as high as 1000 on a 20 mm by 20 mm target area. However, this would require manual positioning of each lamp and scouting for a lamp configuration which gives homogenous fluxes at these high concentrations; and hence was not attempted for this experimental campaign.

It should also be noted that the spectrum from the HFSS' short-arc xenon lamps (Osram XBO 6500W) is not exactly similar to the ASTM G173-03 AM1.5G solar terrestrial spectrum, the exact comparison is plotted in [112]. Additionally, the spectrum coming from the ellipsoidal reflector will be different than the source lamp spectrum and to avoid any discrepancy in the measurement due to spectral mismatch, I_{sc} measured under $A^+A^+A^+$ solar simulator for reference solar cell was used to calibrate the HFSS lamps. The top cell i.e. the InGaP is the limiting cell in our triple junction cells provided by CESI SpA, and hence a spectral mismatch between a xenon lamp and actual solar irradiation will cause slight overestimation of the current for the xenon lamp as shown by Doscher et al. [74]. However, the approach of using the I_{sc} of the reference cell measured under an $A^+A^+A^+$ solar simulator having spectrum identical to the real solar spectrum for calibrating the grayscale maps of HFSS allows avoiding any overestimation.
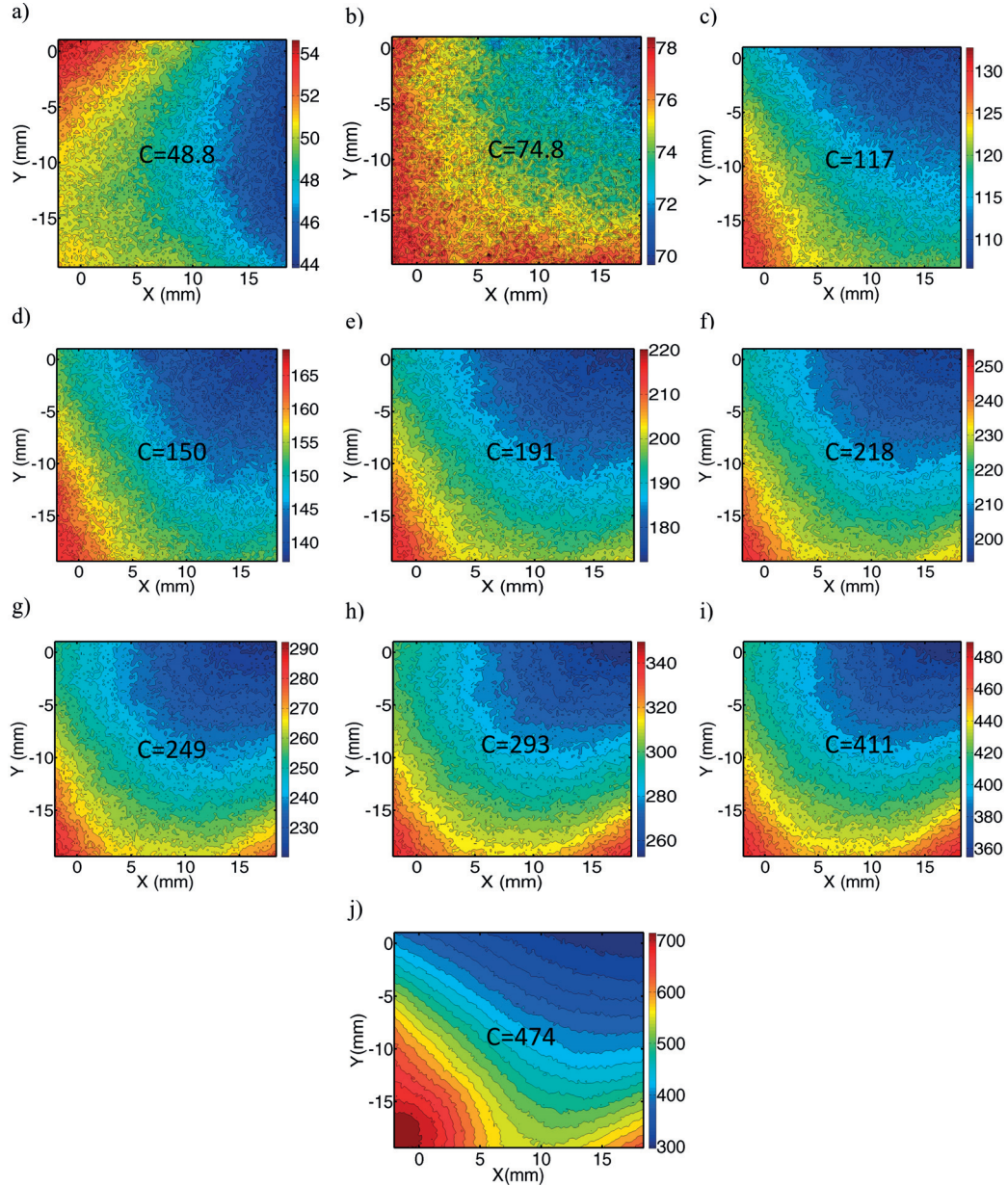
Fig. 4.10 Irradiation flux profiles as received on the integrated photoelectrochemical device's photoactive area (20mm by 20 mm) measured using a combination of lambertian target, CCD camera and reference III-V PV solar cell for average concentrations of (a) 48.8, (b) 74.8, (c) 117, (d) 150, (e) 191, (f) 218, (g) 249, (h) 293, (i) 411 suns, (j) 474. The iH factor are (a) 22%, (b) 11.7%, (c) 22%, (d) 21%, (e) 25%, (f) 28%, (g) 29%, (h) 33%, (i) 33%, (j) 88% respectively.

4.3	**Results and Discussion**

Several approaches for the definition of STH efficiency were introduced during the last years [113], [114], in order to benchmark the different demonstrations. Here,

$$\eta_{\mathrm{STH}} = \frac{n \cdot F \cdot \dot{m} \cdot E_{\mathrm{eq}}^0}{M \cdot P_{\mathrm{in}}}, \tag{4.1}$$

is used where n is the number of participating electrons and equals 2 for hydrogen evolution, F is the Faradays constant, M [g/mol] is the molar mass of hydrogen, $\dot{m}$ [g/sec] is the mass flow rate of produced hydrogen, E_{eq}^0 (~1.229 V) is the equilibrium potential at standard conditions (neutral pH, $T = 25^{\circ}C$ and $p = 1$ atm), and P_{in} [W] is the incident irradiated power. The irradiated power equals the global horizontal irradiation (GHI) as no tracking is considered. An alternative and equivalent definition is

$$\eta_{\mathrm{STH}} = \frac{I_{\mathrm{op}} \cdot E_{\mathrm{eq}}^0 \cdot \eta_F}{P_{\mathrm{in}}}, \tag{4.2}$$

where η_F is the faradaic efficiencies and I_{op} [A] is the operating current. For the case of concentrated irradiation, P_{in} is given by $C.I_{\mathrm{in}}.A_{\mathrm{PV}}$ where C is the irradiation concentration, defined as the ratio of the power incident on the concentrator area to the effective power received on the photoactive area, I_{in} [W/m²] is the incident irradiation intensity, and A_{PV} is the photoactive area. STH efficiency can further include an index which represents the averaging time considered for the efficiency measurement [114]. In our case, a test over 2 hours (~10^4 seconds) is performed, so the reported solar-to-hydrogen efficiency corresponds to η_{STH}^4. The STH efficiency can also be defined using high heating values of hydrogen in the numerator, and/or using the direct normal irradiance (DNI) instead of global horizontal irradiance (GHI) in the denominator (for concentrated applications). A compilation of various ways of defining and using STH efficiency is presented in section 4.3.1 and in this chapter, standard equilibrium potential and GHI values are used for fair and realistic comparisons.

4.3.1 Discussion about the definition of Solar to hydrogen efficiency

The solar-to-hydrogen efficiency, which is defined using solar energy as the input and produced hydrogen's chemical energy as the output, is the most widely used parameter to quantify the performance of this energy conversion process.

Alternative methods for defining solar-to-hydrogen efficiencies were introduced during the last years [113], [114], in order to benchmark the different reported efficiencies. Globally, the STH can be quantified as:

$$\eta_{STH} = \frac{\dot{n}_{H_2} \, \Delta E}{I_{in}} \qquad (4.3)$$

Where $\dot{n}_{H_2}$ is the molar flow rate of the produced hydrogen, ΔE is the specific energy of hydrogen, and I_{in} is the total solar irradiation incident on the device. For proper benchmarking and comparison purposes, here different parameters included in the formulation are defined.

a. Definition of the hydrogen molar flow rate $\dot{n}_{H_2}$

For the produced hydrogen, the most realistic approach is to use the measured flow of the dry and pure hydrogen at the output of the process. Note that the produced hydrogen always contains a certain amount of water vapor and oxygen, due to their transport across the separator by diffusion, permeation and electro-osmotic drag. A proper gas composition analysis should be performed in order to quantify the purity of the produced hydrogen. Given that this approach requires not only an appropriate gas dehumidification and purification process (in order to completely remove water vapor and oxygen from the produced hydrogen) but also a high accuracy gas flowmeter, many studies calculate the hydrogen flow using directly the operating current of the device (giving equivalent equation as 4.2):

$$\dot{n}_{H_2} = \frac{I_{op}}{2F} \eta_F \qquad (4.4)$$

where I_{op} is the operating current, F is the Faraday constant and η_F is the Faradaic efficiency of the device. This latter should be used in order to take into account the competitive reactions occurring in the electrodes (a part of the current is used to drive those competitive reactions instead of the water splitting reaction) and the hydrogen crossover across the separator (a part of the produced hydrogen is lost due to crossover across the separator, and which depends on the separator material and the operating conditions). Generally, the crossover is lower for solid acid electrolytes than alkaline separators and is only important at low current densities.

b. Definition of hydrogen's specific energy ΔE

The definition of hydrogen's specific energy depends on the hydrogen energy conversion process and the form in which one consumes that energy. For the

process where hydrogen is converted in a fuel cell, water is generally produced in vapor phase through an electrochemical reaction with oxygen. In this particular case, the enthalpy of water formation in vapor phase should be considered as the reference. Regarding the form in which energy is consumed, one can distinguish the conversion into electrical energy or into heat. Obviously, not all the chemical energy of hydrogen can be converted into electrical energy, whatever the conversion process. The Gibbs free energy $\Delta G = \Delta H - T\Delta S$ should be used in order to consider the maximal reversible work that can be obtained from the thermodynamic system. The different thermodynamic potentials that can be used, as well as the corresponding thermoneutral voltages, are summarized in Table 4.3.

Table 4.3 Reference thermodynamic potentials of hydrogen, and corresponding thermoneutral voltages.

Thermodynamic potential considered for ΔE	Value [kJ/mol$_{H2}$]	Thermoneutral voltage [V] ($\Delta E / 2F$)
Total enthalpy, vapor phase ($\Delta H_{H_2O_{(v)}}$)	241.8	1.253
Total enthalpy, liquid phase ($\Delta H_{H_2O_{(l)}}$)	285.8	1.481
Gibbs free energy, vapor phase ($\Delta G_{H_2O_{(v)}}$)	228.6	1.184
Gibbs free energy, liquid phase ($\Delta G_{H_2O_{(l)}}$)	237.1	1.229

It should be noted that the natural phase of water in standard conditions is liquid. That is the reason why the enthalpy of water formation in the liquid phase is generally used, considering that latent heat of water condensation can be recovered [114]. Regarding the form of energy, while some authors consider only the maximal reversible work (Gibbs free energy) (e.g. Nakamura et al. [68], J.William et al. [82], Bonke et al. [77]), others consider all the reaction enthalpy, taking into account the reaction entropy (e.g. Peharz et al. [69]). As a global reference for benchmarking, the Gibbs free energy of hydrogen with water production in the liquid phase can be considered, which corresponds to a thermoneutral potential of 1.23 V for the efficiency calculation.

c. Definition of the total solar irradiation I_{in}

I_{in} is the total equivalent solar irradiation incident on the device. It can be directly measured outside using a pyranometer (given the photoactive area) if the solar irradiation is used as the input. The diffuse and diffracted part of that incident irradiation are not exploitable in concentrated devices (they use only direct irradiation as non-direct part can't be focussed), and this represents a technical limitation which should be taken into account while benchmarking the devices. Furthermore, the spectrum differences between the solar simulator (if used) and the real solar irradiation should be considered because they can induce non-negligible performance differences. The total equivalent solar irradiation can be calculated as:

$$I_{in} = \frac{I^{sc}_{in}}{F_{DST} F_{GSI} F_{SSS}} \tag{4.5}$$

where I^{sc}_{in} is the total irradiation measured at the solar cell position, F_{DST} is device solar transmission factor, F_{GSI} is the global solar irradiation factor, and F_{SSS} is the solar simulator's spectrum factor.

- Device solar transmission factor F_{DST}

The device solar transmission factor is the ratio between the irradiation that really reaches the surface of the solar cell and the incoming solar flux on the device. Depending on the design, a part of irradiation can be lost due to scattering in the solar glass, cooling water, catalyst particles etc. The global irradiation can be considerably higher than the incident irradiation on the solar cell.

- Global solar irradiation factor F_{GSI}

This global solar irradiation factor represents the ratio between DNI and GHI. In concentrated PEC devices, a first and direct limitation is the fact that only the direct part of the irradiation (~85%) is exploitable [115]. This technical limitation should be considered while benchmarking the devices performances. For devices without any irradiation concentration, F_{GSI} is equal to 1.

- Solar simulator's spectrum factor F_{SSS}

F_{SSS} factor is the ratio between the total energy output of the system obtained using solar irradiation and the total energy obtained using an equivalent solar simulator, for the same total irradiation intensity. Indeed, even if the flux is the same, the spectrum is slightly different [74], and this can considerably impact the performance of the device.

In our reported values, the flux map characterization and calibration with reference cell's I_{sc} under AM1.5G spectrum eliminated further incorporating of the F_{SSS} and F_{GSI}. And our STH efficiency with F_{DST} of 0.91 is 15.6%.

4.3.2 Efficiency and performance of CIPEC device η_{STH} = 17.2% is measured utilizing the measured incident irradiation on the photovoltaic component as P_{in}, and the measured mass flow rate of dry hydrogen as $\dot{m}$. The corresponding measured operating current was 22 A, i.e. a current density of 0.88 A/cm$_{EC}^2$ and 6.04 A/cm$_{PV}^2$. The *I-V* characteristics of the individual components (measured separately) at the operating concentration of *C* = 474 are shown in Fig. 4.13.

At 474 kW/m^2, the characteristic curve of the photovoltaic component crosses the electrolyzer's curve at a voltage of about 2.03 V, the operating voltage of the CIPEC. The device was operating in the plateau region of the photovoltaic component. Thus, the operating current was very close to the maximum achievable current (short circuit current). Given that the hydrogen production rate is proportional to the operating current, it can be stated that the device was performing close to its maximum production point. It is also worth noting that the CIPEC is designed to operate at concentrations which can reach 1000 kW/m^2, but the experiments were stopped at 474 kW/m^2 due to experimental challenges related to stray radiation on the protective shield and the corners of the solar glass, both increasing as we moved the device closer to the focal plane in order to reach higher concentrations. Eventually, the glass and the epoxy glue broke at the corners (see section 4.2.5)). The driving force for high irradiation concentrations is related to cost: at 1000 kW/m^2 the estimated cost of production for hydrogen is predicted to be 32% lower than the cost at 474 kW/m^2, based on a techno-economic analysis performed by Dumortier et al. [21].

Our measured efficiency drops to η_{STH} = 15.6% if the solar input generated from the solar simulator is considered (instead of the irradiation that really reaches the surface of the solar cell). This ~10% difference is due to irradiation extinction in the solar glass and in the reactant water on the top of the solar cell.

For a comparison with other demonstrations, it should be noted that the same irradiation should be utilized, i.e. all demonstrations – independent of whether they use concentrated irradiation or not – should use GHI instead of DNI. This reduces the efficiency of demonstrations using concentrated irradiation (usually based on DNI) as only direct irradiation is useful [115]. Hence appropriate correction factors should be used for the reported efficiencies, defined based on DNI [68], [69], [84]

and compared with GHI-based efficiencies. Correction factors are also needed for efficiencies reported based on the thermoneutral voltage (i.e. 1.48 V) instead of the standard equilibrium voltage, i.e. Gibbs free energy [69], [84]. Ager et al. [79] compiled a list of the major PEC demonstrations up to 2015. This list is further extended, making it consistent with our efficiency definition according to Eq. (4.1), and included demonstrations after 2015 [68], [80]–[82], [77], [84], [94]. Here, the STH efficiency for the various PEC device demonstrations is compared with respect to the objective functions of *i*) output power (Fig. 4.12), and *ii*) operating electrochemical current density (Fig. 4.11). In addition, the photovoltaic and catalyst materials are categorized into inexpensive (lighter color = more inexpensive) and expensive (darker color = more expensive) categories, and the degree of integration of the photovoltaic and catalysts is categorized: from integrated and partially integrated (wired catalyst), to non-integrated PV plus EC configurations. This further allowed to separate demonstrations employing a different number of series-connected PV to EC ratios.

Figure 4.11 shows that the highest electrochemical current densities together with high STH efficiencies were generally achieved using a combination of expensive photovoltaics (III-V based) and expensive catalysts (rare metal based). It also shows that CIPEC devices generally show higher operating current densities compared to non-concentrated devices. Our demonstration at $C = 474$ showed the highest reported electrochemical (0.88 A/cm_{EC}^2) as well as photovoltaic (6.04 A/cm_{PV}^2) current density while maintaining a high efficiency (17.2%). Additionally, Fig. 4.11 demonstrates that integrated devices operate at better performance than non-integrated or series-connected devices. This leads us to argue that thermal and electronic management (as achieved in our device) is a good rationale for the integration of photoabsorber (such as PV) and catalyst (such as complete EC) components.

It should be noted that the output power and current density in Fig. 4.12 and Fig. 4.11 are in logarithmic scale. Our output power of 27 W is at least 27 times higher than the second-best output power demonstrated for a single PEC cell [69], and around two orders of magnitude higher than most other demonstrations. Even the recent advancement by Fallisch et al. [84] (based on the work of Peharz et al. [69]), in which they combined 8 PEC cells in parallel to make a mini-module, showed a total power of only 9W, and with a hydrogen production rate three times lower (i.e. 274 mg/hr) than what is demonstrate here with a single cell (821 mg/hr). This large output power at high efficiency, and for a predicted cost-competitive device [21], opens a pathway for device scalability towards the large-scale deployment of photoelectrochemical water splitting.
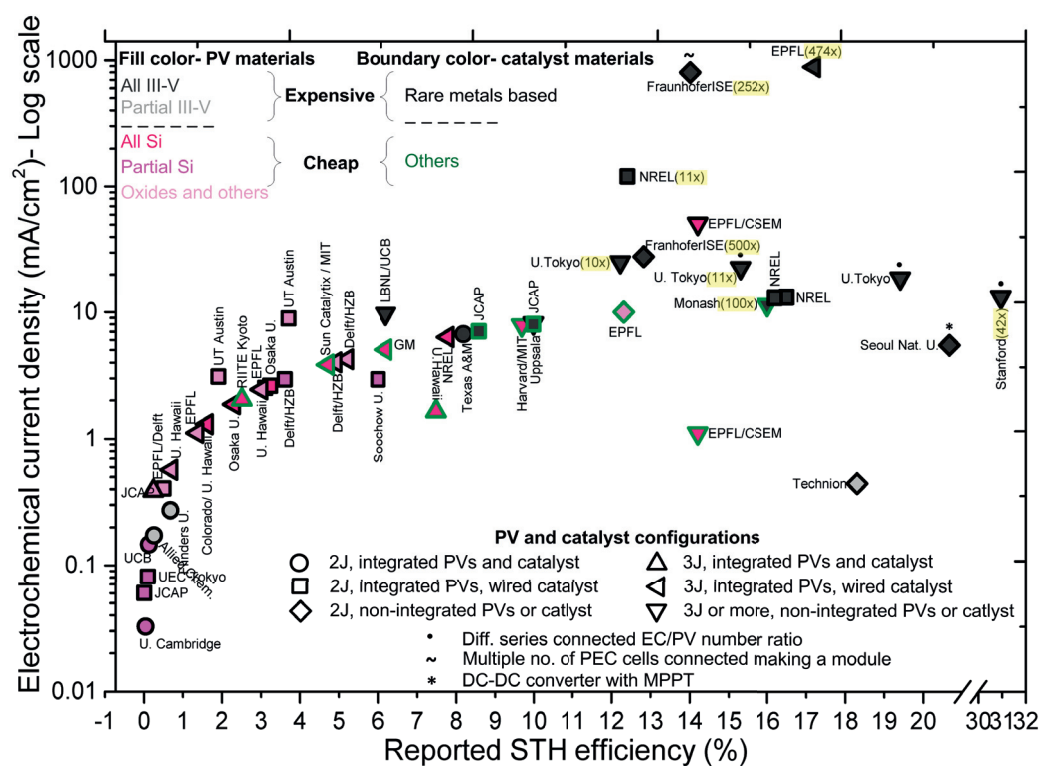
Fig. 4.11 Reported STH efficiencies and reported, or derived (from the reported STH, P_{in} and EC area), operating electrochemical current densities for different demonstrations (references and details can be found in table 4.4 and section 4.3.3). The shape of the points shows the photovoltaic and catalyst configuration (whether 2J/3J PVs or integrated/non-integrated device designs). The fill color shows the type of the photovoltaic material used along with cost, being inexpensive (lighter color), or expensive (dark color). The boundary color shows the type of the catalyst material along with cost: inexpensive (green), or expensive (black). The symbol with the single dot on top represents a configuration which has multiple series-connected ECs per PV. The symbol with the tilde on top represents a configuration having multiple PEC units or cells "fluidically" connected in series or parallel. The symbol with a star represents a configuration deployed with external dc-dc based maximum power point tracking for power matching. The number in the brackets next to the symbol represents the demonstrated irradiation concentrations. If no number is indicated, then no concentration is used or no concentration data were reported or derivable.

The three demonstrations with higher efficiencies than ours [68], [80], [94] can be categorized into two types. One being demonstrators which employ a different

number of ECs (in series) for one single PV component [68], [94] and the other being a demonstration which deploys an external dc-dc converter for power matching between the PV and EC [80]. Connecting PV components or EC components in parallel is similar to increasing the PV and EC active areas. Connecting PV components and EC components in series, however, can open new ways to achieve higher STH efficiencies. This is what is shown by Nakamura et al. [68] (3 series-connected PVs with 5 series-connected ECs), and by Jia et al. [94](1 PV with 2 series-connected ECs), who employ multiple ECs per PV, which has the potential to boost the STH efficiencies by the ratio of series-connected ECs to PV. It is claimed that one of the strengths of our device design is that it can employ close thermal and electronic integration, together with the possibility of having a different number of series-connected PV and ECs. It is predicted that our device STH efficiency will increase to 34% (according to Eq. (4.1)) if we deploy a 2/1 EC/PV ratio at the operating EC current density of 13.6 mA/cm^2. This is the same J_{opEC} that was demonstrated by Jia et al. at an efficiency of 31%. It is predicted that the STH efficiency of our device will increase to 28.7% if we deploy a 5/3 EC/PV ratio at J_{opEC} of 18.8 mA/cm^2 (demonstrated by Nakamura et al. [68] at an efficiency of 19.4%).

However, simply aiming for record STH efficiencies at the expense of low current densities is not meaningful for practical and competitive implementation. The pressing issue now is to achieve high operating current densities at high efficiency, and this is particularly important for the devices made of expensive and high performing PV and EC materials (as used in all these devices). As shown in our earlier modeling work [75], there exists a tradeoff between these two objective functions, leading to the formation of a Pareto front, implying that STH efficiency and EC operating current density cannot be maximized at the same time. But, in fact, the product of efficiency and operating current density must be maximized for an optimal and cost-effective performance. A simple maximization of $\eta_{STH} \times J_{op}$ predicts that our demonstrated device should be at least 50 times more cost-effective than the high efficiency and low current density demonstrations reported previously [68], [94].

The different ratios of series-connected EC/PV can be deployed only when the operating point of the PEC device is not at the maximum power point of the PV component, this is a way of power matching the PV and EC components. The same aim is achieved by using an external dc-dc converter, as done and shown by Chang et al. [80]. They started with a non-optimal design and operation of the PEC device, where the gap between the operating power and the maximum power delivered by the PV components was very large (even larger than the losses in the external power electronics components), and the device had a low operating current density of 5.6

mA/cm_{EC}^2. For their configuration, they showed that the efficiency can be boosted from 18.4% to 20.6% when using the dc-dc converter. The efficiency in a well-designed device is only limited by the J_{sc} of the PV at 1 sun under standard conditions.

The only other demonstration showing higher STH efficiency (without employing any external converters or series-connected PV/EC) was by Licht et al. [85], and resulted from a higher PV J_{sc} (14.9 mA/cm^2 under std. conditions) given by the dual junction. It should be noted that the typically achieved J_{sc} for dual junction III-V cells is higher than that of triple junction cells, and hence, normally, dual junction III-V cells will lead to higher STH efficiency. But, they are also limited by the lower V_{oc}, and consequently their potential to reach higher electrochemical current densities is limited.

4.3.3 Photoelectrochemical demonstration review All major experimental photoelectrochemical hydrogen generation demonstrators and their corresponding STH efficiency, electrochemical and photovoltaic current density, output (hydrogen equivalent) power (i.e. $I_{op} \cdot E^0_{eq}$), and the underlying integration method (integrated/semi-integrated/non-integrated) and the incorporated catalyst and PV materials are compiled here. The list of major demonstrators till 2015 are taken from Ager et al. [79], and the list is further extended to include recent demonstrators till 2017 ([68], [80]–[82], [77], [84], [94]). PV component involving full or partial III-V material is categorized as expensive, and similarly, EC components involving full or partial rare earth elements (Pt, Ru, Ir, Pd etc.) or their oxides are categorized as expensive. There are three modes of integration; i) fully integrated implying no wired catalyst, ii) partial integrated implying at most one wired connection between PV and catalytic part (gray highlighted), and iii) non-integrated approaches where the PV is macroscopically wired to the EC.

It should be noted that standard equilibrium potential (corresponding to the Gibbs free energy) and GHI should be used for a fair comparison among different demonstrators and hence appropriate adjustments are made to the values which do not follow this convention [68], [69], [77]. Additionally, a simple estimation of the best possible efficiency with III-V based photovoltaic (without dc-dc converter) can be obtained from the I_{sc} (assuming PV has high enough V_{oc} and fill factor, FF, such that the operating point lies in the plateau region of PV and hence assuming $I_{op} \sim I_{sc}$) under no concentration. Care should be taken in interpreting the cases where the STH efficiency is much higher than those allowable from the PV's I_{sc} [77].
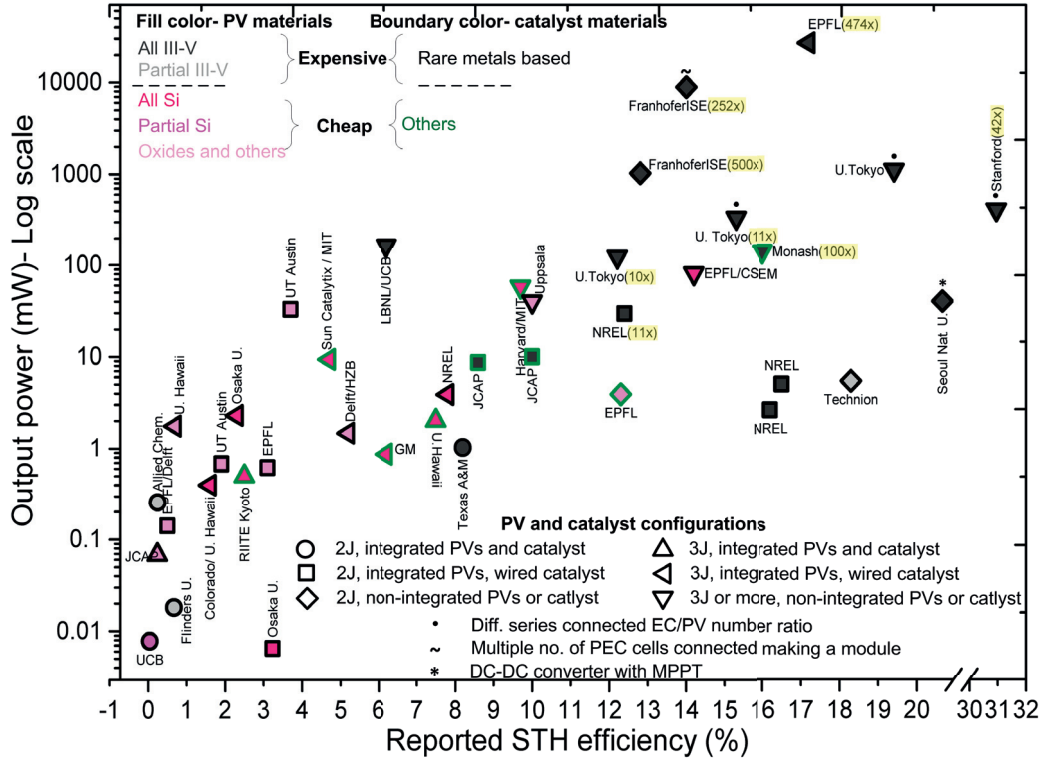
Fig. 4.12 Reported STH efficiencies and reported/derived (from the reported STH, P_{in} and EC area) output power for different demonstrations (references and details can be found in Table 4.4). The shape of the points shows the photovoltaic and catalyst configuration (whether 2J/3J PVs or integrated/non-integrated device designs). The fill color shows the type of the photovoltaic material used along with it being cheap (lighter color) or expensive (dark color). The boundary color shows the type of the catalyst material along with it being cheap (green) or expensive (black). The symbol with the single dot on top represents a configuration having multiple numbers of series-connected ECs per PV. The symbol with the ~ on top represents a configuration having multiple numbers of PEC units or cells "fluidically" connected in series or parallel. The symbol with a star represents a configuration deployed with an external dc-dc based MPP tracking for power matching. The number in the brackets next to the symbol represents the demonstrated irradiation concentrations, if no number is indicated then no concentration is used or no concentration data was reported or derivable.

The demonstrator's review plot showing the output power and STH efficiency along with various material/device configurations (presented in Fig. 4.12) re-iterates that high performance/ (here) high output power is normally achieved with expensive but best performing PV and catalyst materials (same behavior was noticed for current density comparison plot).

Table 4.4 Review of demonstrators for photoelectrochemical production of hydrogen. The gray underlay represents partial integrated device configuration implying at most one wired connection between PV and catalytic part

No.	Year	Institute	Inventors	Output power [mW]	STH eff. (%)	EC current density [mA/cm²]	PV current density [mA/cm²]	EC material	PV material	Input irradiation [mW/cm²]	Integration mode
1	2014	EPFL/ Delft U.	Bornoz et al. [116]	0.1415	0.50	0.4065	0.4065	Expensive	Cheap	100	Integrated
2	2014	BNU/C AS/Sooc how U.	Wang et al. [117]	-	6	2.93	2.93	Expensive	Cheap	60	Integrated
3	2014	JCAP	Shaner et al. [118]	-	0.0068	0.06	0.06	Expensive	Cheap	1080	Integrated
4	2013	UC Berkeley	Liu et al. [119]	-	0.12	0.15	0.15	Expensive	Cheap	150	Integrated
5	2013	Delft U./ HZB	Abdi et al. [120]	-	3.6	2.93	2.93	Expensive	Cheap	100	Integrated
6	2012	EPFL	Brillet et al. [121]	0.62	3.10	2.52	2.52	Expensive	Cheap	100	Integrated
7	2012	Univ. of Cambridge	Lin et al. [122]	0.0078	0.04	0.033	0.033	Expensive	Cheap	100	Integrated
8	2006	UT Austin	Park and Bard [123]	0.68	1.9	3.09	3.09	Expensive	Cheap	200	Integrated
9	1998	NREL	Khaselev and Turner [14]	29.51	12.4	120	120	Expensive	Expensive	1190	Integrated
10	1987	Texas A&M	Kainthla et al. [124]	1.025	8.2	6.67	6.67	Expensive	Expensive	100	Integrated
11	1981	UC Berkeley	Mettee et al. [125]	-	0.10	0.081	0.81	Expensive	Expensive	100	Integrated

4: Experimental Demonstration

#	Year	Institution	Reference								
12	1977	Flinders U.	Ohashi et al. [126]	0.018	0.67	0.27	0.27	Expensive	Expensive	50	Integrated
13	1976	U. of Elec-commun.	Morisaki et al. [127]	-	0.10	0.08	0.08	Expensive	Cheap	100	Integrated
14	1976	Allied Chem.	Nozik [128]	0.255	0.25	0.173	0.173	Expensive	Expensive	85	Integrated
15	2014	EPFL	Luo et al. [83]	3.91	12.3	10	10	Cheap	Cheap	100	PV+EC
16	2007	ISE Fraunhofer	Peharz* et al. [69]	1024	12.81	27.76	4421.4	Expensive	Expensive	70.9(DNI)@500	PV+EC
17	2001	NREL	Khaselev et al. [129]	4.95	16.5	13.4	13.4	Expensive	Expensive	100	Integrated
18	2000	Technion	Licht et al. [85]	5.41	18.3	0.44	20.1	Expensive	Expensive	135	PV+EC
19	1988	Osaka U.	Sakai et al. [130]	0.0065	3.23	2.62	2.62	Expensive	Cheap	100	Integrated
20	2015	LBNL/JCAP	Walczak et al. [131]	0.068	0.25	0.39	0.39	Expensive	Cheap	200	Integrated
21	2014	Delft U./HZB	Han et al. [132]	1.47	5.2	4.23	4.23	Expensive	Cheap	100	Integrated
22	2013	Delft U./HZB	Abdi et al. [120]	-	4.9	3.98	3.98	Expensive	Cheap	100	Integrated
23	2010	U. Hawaii	Gaillard et al. [133]	-	3	2.44	2.44	Expensive	Cheap	100	Integrated
24	2010	U. Hawaii/NREL	Zhu et al. [134]	0.4	1.6	1.3	1.3	Expensive	Cheap	100	Integrated
25	2010	EPFL	Brillet et al. [135]	-	1.36	1.11	1.11	Expensive	Cheap	100	Integrated
26	2005	U. Hawaii	Miller et al. [136]	1.75	0.70	0.57	0.57	Expensive	Cheap	100	Integrated

27	2014	Harvard/ MIT	Cox et al. [137]	58.2	9.7	7.89	7.89	Cheap	Cheap	100	PV+EC
28	2014	UC Berkeley / LBNL	Modestino et al. [138]	165.8	6.2	9.7	5.07	Expensive	Expensive	100	PV+EC
29	2013	Uppsala	Jacobsson et al. [139]	40	10	8.13	8.13	Expensive	Expensive	100	PV+EC
30	2013	U. Tokyo	Fuji et al. [95]	121.44	12	24.7	100.5	Expensive	Expensive	1012	PV+EC
30a	2013	U. Tokyo	Fuji et al. [95]	335.42	15.3	7.57	45.45	Expensive	Expensive	1095	PV+EC
31	2011	Sun-Catalytix / MIT	Reece et al. [140]	9.4	4.7	3.82	3.82	Cheap	Cheap	100	Integrated
32	2009	Osaka U.	Yamane et al. [141]	2.3	2.3	1.87	1.87	Expensive	Expensive	100	Integrated
33	2006	Gen. Motors	Kelly and Gibson [142]	0.868	6.2	5.04	5.04	Cheap	Cheap	100	Integrated
34	2005	UT Austin	Park and Bard [143]	32.8	3.7	8.8	8.9	Expensive	Expensive	100	Integrated
35	2003	RIITE Kyoto	Yamada et al. [144]	0.5	2.5	2.03	2.03	Cheap	Cheap	100	Integrated
36	2001	NREL	Khaselev et al. [129]	3.9	7.8	6.34	6.34	Expensive	Expensive	100	Integrated
37	1998	U. Hawaii	Rocheleau et al. [145]	2.03	7.5	1.64	6.1	Cheap	Cheap	100	Integrated
38	2015	U. Tokyo	Nakamura** et al. [68]	1107	19.41	18.75	-	Expensive	Expensive		PV+EC
39	2015	Monash U.	Bonke*** et al. [77]	143.9	16	11.7	1300	Expensive	Expensive	99.5*100x	PV+EC

40	2017	EPFL	Tembhurne et al. [86]	27060	17.20	880	6040	Expensive	Expensive	474*100x	Integrated
41	2016	CSEM/EPFL	J.Willem et al. [82]	81.3	14.2	50.86	11.6	Expensive	Cheap	100	PV+EC
41a	2016	CSEM/EPFL	J.Willem et al. [82]	81.3	14.2	1.102	11.6	Cheap	Cheap	100	PV+EC
42	2015	JCAP	E. Verlage et al. [146]	8.66	8.6	7.04	7.04	Cheap	Expensive	100	Integrated
43	2016	JCAP	K. Sun et al. [147]	10	10	8	8	Cheap	Expensive	100	Integrated
44	2017	Seoul Nat. U.	Chang et al. [80]	41.33	20.66	5.6	16.81	Expensive	Expensive	100	PV+EC
45	2017	NREL	Young et al. [81]	2.6	16.2	13.2	13.2	Expensive	Expensive	100	Integrated
46	2017	Fraunhofer	Fallisch# et al. [84]	8900	14	800	2511	Expensive	Expensive	75 (DNI) @252x	PV+EC
47	2016	Stanford	Jia et al. [94]	411	31	13.4	528.6	Expensive	Expensive	100 @ 42x	PV+EC

*Pebarz, et al. [69]: Efficiency value is adjusted (after taking Gibbs free energy and equivalent GHI number) from the reported one. The new value is obtained by multiplication of 1.23/1.48 and further multiplication of 1/1.174 (which is average ratio between direct normal irradiation (DNI) and global horizontal irradiation GHI (direct+diffuse) for Freiburg region for all hour having DNI>700 W/m^2 obtained using NREL's SAM)

**Nakamura et al. [68]: Efficiency value is adjusted (after taking equivalent GHI and corrected ratio of P_{ϕ}/P_{max}) from the reported one. The new value is obtained by multiplication of 1/1.153 (which is the average ratio between DNI and GHI (direct+diffuse) for Miyazaki region for all hours having DNI>700 W/m^2 obtained using NREL's SAM). This value is further corrected for the ratio of P_{ϕ} (operating point power) and P_{max} (max power from PV) which is reported to be 1.09 but in theory, P_{ϕ} can have the best value of P_{max} and hence this ratio can't be greater than 1. Taking the optimistic value of 1 for P_{ϕ}/P_{max} the corrected STH efficiency turns out to be 19.4%. The PV current density

calculated using their reported light receiving area per module of 57 mm² with PV cell area of 2.5 mm² and operating current of 0.3 A turns out to be 0.526 A/cm² @ 1x concentration which is theoretically not possible and hence there is a wrong reported area which makes PV current density not realistically calculable.

*** *Bonke et al.* [77]: *The reported STH efficiency value is adjusted to take into account the reported J$_{sc}$ (130 A/m²) at 1 sun. The reported J$_{sc}$ at 100x concentration is 182 kA/m² which is much more than the generally expected value of 130 kA/m² and hence a corrected factor of 130/182 has been multiplied to calculate the new STH efficiency. The operating current densities have also been adjusted accordingly.*

#*Fallisch et al.* [84]: *The reported STH efficiency values of 19.8% (with high beating value) is observed for their Hycon module (comprising 8 cells) at around 17h where their reported DNI is 750 W/m². This value is adjusted by multiplication of 1.23/1.48 (for accounting Gibbs free energy) and further multiplication of 1/1.174 (which is average ratio between DNI and GHI (direct+diffuse) for Freiburg region for all hour having DNI>700 W/m² obtained using NREL's SAM)*

4.3.4 Stability and dynamic response of CIPEC device The HFSS is used for providing varying irradiation concentrations with uniform (inhomogeneity, $iH = (C_{max}-C_{min})/C_{avg.}$, around 20%) irradiation profiles on the IPEC. The IPEC device is tested at concentrations varying between 117 and 474. The results of an 18 minute-test at each concentration are shown in Fig. 4.13(a). Each of the output mass flow profiles presented in Fig. 4.13(a) show a transient 'on' region (~200 sec.), a stable (~600 sec.) operating region, and a transient 'off' region (~300 sec.). The recorded flow rate profiles are for produced hydrogen with a small quantity of water vapor. This water vapor crossed over from the anodic channels via the Nafion® membrane to the cathodic channels. Any liquid water present in the cathodic side is collected in the water trap (installed just before the mass flow meter), so that only the water vapor could find its way to the flowmeter. An excess mass in the range of 13-20%, measured by the flowmeter, was attributed to water vapor. It is confirmed by gas chromatography that the produced gas was mainly composed of hydrogen. Theoretical calculations show that the specific humidity of saturated hydrogen is ~ 13% and ~ 22% respectively at 15 and 25°C. At a concentration of 411, a daily production of hydrogen of 4.255 g would be expected (with around 6 hours of operation).

The dynamic response of the system (i.e. the transient response at the light on and light off in the range of 100s of seconds) is governed by the switch on and off characteristics of the HFSS's xenon lamps and their fluctuations. Normally each lamp takes around 200 seconds to reach a stable output, correspondingly, on/off transients of the recorded output gas flow profiles (presented in Fig. 4.13(a)) recorded for the entire experimental setup (including a solar simulator, IPEC device, and measurement test-bench) are in the same range. The IPEC device showed stable output for varying concentrations, however, the small fluctuations around the average value in the steady operating regime are more dominant for higher concentrations (above $C = 150$). The standard deviation for each of the profiles (for the time range of 200-800 seconds for which the device is in steady state) increases from 0.002 to 0.004 mg/s (equivalently 1-3% variation around average) for concentrations of 117 to 411. These fluctuations are a direct result of the fluctuations in the Xe arc of the HFSS's Xe arc bulbs. For separately measured irradiation maps, where the time evolution of the maps was tested, it is confirmed that the lamps themselves produced an average concentration fluctuating within 1.25 – 3% (for low-high concentration), and increasing for higher concentrations. The temperature variations (measured at the cathode plate) for the 10 minutes at a steady state were less than 0.5°C, and hence these variations are not believed to cause noticeable fluctuations in the measured flow.
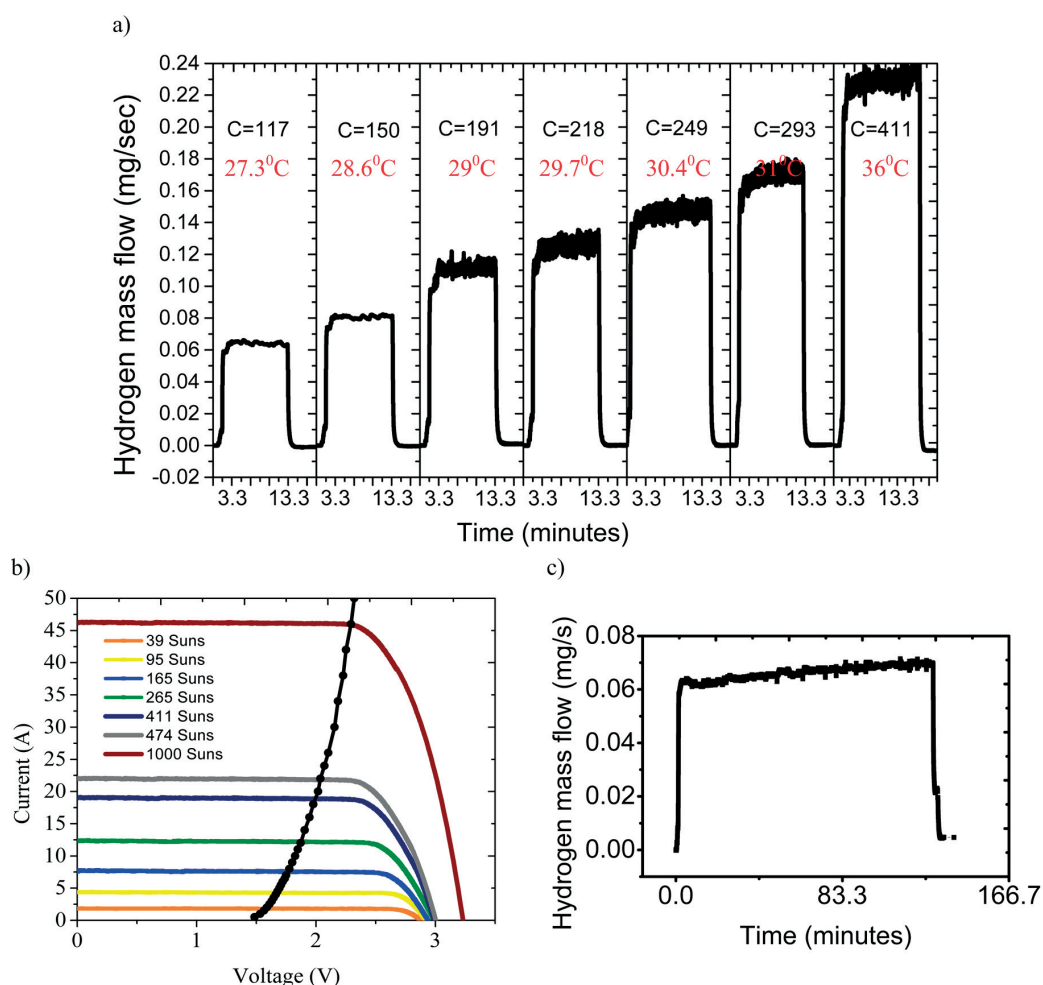
Fig. 4.13 (a) Measured hydrogen mass flow rate produced with changing irradiation concentration. Reactant flow rate is 4 l/min. Each ~18 minutes of the experiment has a characteristic on and off transient (in the range of 200-300 seconds) and a steady operation of about 10 minutes. The on/off transients and the fluctuations in the steady operating range resulted from the time characteristics of the HFSS and its Xe arc bulbs. The steady state temperatures recorded at the back of the cathode plate with a thermal pad sensor are shown in red. (b) Measured characteristic curves of the PV and EC components (measured separately) of the IPEC device at varying irradiation concentrations. The PV curves at $C = 411$, 474, and 1000 were extrapolated from the measured parameters at $C = 265$. The EC curve was measured at an input DI water flow rate of 4 l/min. (c) Stable output hydrogen flow rate at $C=117$ for a total time of around 2 hours.

For all the concentrations tested, the operating points lied in the plateau region (i.e. $I_{op} \sim I_{sc}$) of the PV, as the operating voltages are all less than 2.04 V (for the input liquid water flow rate of 4 l/min).

The system is designed to be operated at an irradiation concentrations of ~1000 suns, however, due to the technical limitations imposed by the high flux solar simulator (refer to section 4.2.5) the tests were concluded only till 474 suns. For higher concentrations, the uniform flux on the IPEC can be achieved only by moving the device closer to the focal plane of the lamps and by using the inner ring lamps of the HFSS, however, this also increases the intensity in the surrounding area (non-PV area of the device). A water cooled aluminum protective shield is used to protect the device from this unwanted irradiation but the flux peaks on the shield as well as solar glass corners become increasingly strong limiting the current tests till 474 suns.

As discussed in section 4.2.5, the flux becomes quite heterogeneous at a concentration of 474 suns, which led to breaking of the solar glass forcing the experiments to be stopped under 8 minutes where only 1-2 minutes of device's steady state performance could be recorded.

The performance potential of the implemented device extrapolated to $C = 1000$ is presented in Fig. 4.13(b). The extrapolating is based on the separate I-V curves of the PV (extrapolated from measurements at $C = 265$) and EC (measured at input flow rate of 4 l/min) components. With the operating point at 2.3 V and 46 A (1.84 A/cm_{EC}^2, 11 A/cm_{PV}^2) the estimated STH efficiency is 17%, with the output power of 57 W having a hydrogen production capability of 1.77 g/hr.

An integral part of our IPEC device is the input reactant mass flow rate, which controls the individual components' temperature and mass transport of the EC and, consequently, the operating point of the device. The operating potential of the device is directly dependent on the input water flow rate and the input irradiation concentration. For a particular concentration, decreasing the water mass flow rate (within a reasonable limit, so as to still maintain the device temperatures below 80°C) increases the EC's temperature and causes the electrochemical overpotentials to be reduced (see Fig. 4.4); hence the device operates at lower operating voltage. For example, for a concentration of 150 suns, a total overpotential drop of 0.25 V was recorded when the flow rate was decreased from 3.8 l/min to 0.34 l/min. The temperature in the EC component (measured with the surface thermal pad sensor at the back of cathode plate) was found to increase from ~25 °C to 60 °C. Similar significant overpotential drops were recorded for $C = 250$ (~0.3 V drop) and $C = 411$ (~0.4 V drop) when the water flow rates were reduced from 4 l/min to ~0.3

l/min. However, for safety reasons, it is decided to operate the system at a high flow rate of 4 l/min. This behavior reversed when device is operated at very high concentrations or very low flow rates (Fig. 4.4), where the performance is limited by mass transport in the device.

It should be noted that a setup allowing uniform fluxes on the PV area without causing intense stray radiation on other parts of the device could be safely operated at low flow rates of 0.3 l/min even at high C, and this would allow the device's operating potential at, for example, 1000 concentration to be even lower than 2.3 V.

Furthermore, to verify the reproducibility of the performance, the IPEC device was characterized on many different days while keeping the experimental conditions similar. For the analyzed case where the input irradiation concentration was 117x, a variation of ~3.4% was noticed in the measured output H_2 flow rate, along with variation of ~2% in the measured (backside cathode thermal pad) temperature. This confirms the reproducibility of the IPEC device's performance. In fact, testing the reproducibility of the flux maps from the HFSS showed that the lamps themselves reproduce the flux maps with an accuracy of ~1-3% (for low to high concentrations).

The stability of the integrated device was confirmed by measuring a stable (non-decreasing) output gas flow rate for ~2 hours, shown in Fig. 4.13(c). The stable output hydrogen flow rate was measured for an irradiation concentration of 117. The output gas flow profile had a slightly increasing trend with time, which was attributed to the fact that the device temperature increased from 20°C to 32°C after 3000 seconds. Afterwards, the variation in the temperature was within 1 degree Celsius (i.e. 32-33ºC or ~3%), in a similar range as the variations of the output gas profile (within 5-7% around the average value of 0.068 mg/s).

4.4 Conclusion

An integrated photoelectrochemical hydrogen generation device was demonstrated, operating under concentrated irradiation. A record output power (27 W), and a record current density (0.88 A/cm_{EC}^2, 6.04 A/cm_{PV}^2) was achieved while maintaining a high efficiency (17.2%), all at an irradiation concentration up to 474 times. Irradiation concentration permits one to limit the active area, and thus to lower the cost of a device, making even rare and expensive components competitive. A III-V material based triple junction photovoltaic component was used. The photo-generated current was diluted (dilution factor of 0.15) in a larger active area (proton exchange membrane based) electrochemical component (with IrRuOx/Pt catalysts), in order to limit the potential losses. The device used several innovations in the design, consisting of an integrated reactant delivery/preheating flow field on the top of the photovoltaic component for smart thermal management, and custom designed conductive paths for close electronic integration. Thermal management proves to be a solid rationale for CIPEC devices, allowing significant improvement in operating potential with controlled reactant flow rates. Performance, dynamic response, and stability testing showed that the device has the ability to produce hydrogen flexibly, with high efficiency in different conditions, and over a long period of time.

From performance testing, it is understood that the electrolyzer's overpotential is a limiting factor for achieving higher current densities. If high performing electrolyzers which have lower activation overpotentials are used, the operating current density can be considerably enhanced. Lewinskia et al. [148] demonstrated a high efficiency electrolyzer that can reach current densities up to 18 A/cm^2 at a voltage lower than 2.8 V. Thus, this electrolyzer can be efficiently integrated into the PV component used in this study, which has an open circuit voltage of 3.1 V at 500 suns. This solution could be very interesting for PEC devices working under high irradiation concentration. The devices could operate at high current densities and at high efficiency without current dilution in a larger electrolyzer, and could also use dual junction solar cells, known to give higher efficiencies. Furthermore, incorporating different combinations of PV and electrolyzer components in series for the studied integrated device design is also a promising strategy for maximizing energy conversion efficiency while keeping acceptable current densities.

High current densities can be achieved by increasing irradiation concentration. Our device has the potential to operate at concentrations as high as 1000 while continuing to function in the plateau region of the photoabsorber. To be economically competitive, further research and development should focus on the development of less expensive solar cells and catalyst materials which can be operated in such a

device in an efficient way. The approach demonstrated here at high power and current densities has the potential to produce hydrogen with high performance, at a cost that appears competitive with conventional fuels, providing a promising pathway for a hydrogen-based renewable future.

Our device can be scaled by changing the irradiation concentration and by changing the active area of the concentrator. Alternatively, multiple concentrator-IPEC units can be connected in series/parallel to meet the increased workload. Furthermore, the device is expected to survive more than 30'000 hours with limited degradations, given the degradation characteristics of its individual components and by the potential for flow based control of operating conditions. With a demonstrated largest output power of 27W and predicted long-term stability, this CPEC approach opens a pathway for device scalability towards the large-scale deployment of photoelectrochemical water splitting.

It should be noted that the function of the demonstrated CIPEC device is not limited to the photoelectrochemical production of hydrogen, but in general extends to the photoelectrochemical production of any chemical commodity in liquid, gas, or solid form. For example, the CIPEC can also be deployed to reduce CO_2, for the electrochemical production of ammonia, to purify water, for the electrochemical production or purification of metals, etc. Our approach, as demonstrated, contributes to new pathways for renewable solar fuel production technology and begins to bridge the gap between academic research and the goal of industrial implementation.

Conclusions and Prospects 5

In this thesis, the direct conversion of solar energy and water into a storable fuel (hydrogen) was investigated via integrated photoelectrochemical (IPEC) devices. The thesis started with proving the economic viability and sustainability of the integrated photoelectrochemical devices working under concentrated irradiation with the help of a quasi-transient techno-economic and environmental model, the results of which were briefed in the introduction of the thesis and are detailed elsewhere [21]. Further, a highly coupled multi-physics 2-dimensional non-isothermal model applicable for integrated PEC devices (with or without irradiation concentration) was developed and validated. Based on this model, heat transfer was studied in detail for such devices and thermal management strategies were developed. The model confirmed the importance of reactant mass flow rate as an important operational parameter whose control allows optimum power point operation of the device. Finally, the thesis utilizes all the guidelines formulated during the modeling work in the development of a CIPEC device not only proving the concept but demonstrating one of the highest photoelectrochemical current density (0.88 A/cm_{EC}^2, 6.04 A/cm_{PV}^2) operation at high conversion efficiency (17.2% STH).

In *chapter 1*, the focus was on the modeling of a device design which uses concentrated solar irradiation to reduce the use of rare and expensive components (i.e. light absorbers and catalysts). A 2-dimensional coupled multi-physics model was presented, which uses finite element and finite volume methods to predict the performance of the IPEC device. Then performance optimization strategies were developed utilizing device design, component and material choice, and adaptation of operational conditions. The model accounted for charge generation and transport in the photoabsorber, charge transport in the membrane-separated catalysts, electrochemical reaction at the catalytic sites, fluid flow and species transport in the porous charge collectors and channels, radiation absorption in semiconductor (and water), and heat transfer for all components. The model predicted that operation under high irradiation is possible and that dedicated thermal management can ensure high performant operation. The model showed to be a valuable tool for the design

of IPEC cells under concentrated irradiation at elevated temperatures. To the best of the knowledge, it is the most detailed yet computationally economic model of an integrated photoelectrochemical device ever reported. In summary, the multi-dimensional multi-physics model allows for in-depth physical understanding providing insights and guidance for the development of efficient, cost-competitive and practical PEC devices.

In *chapter 2*, the focus was on the heat transfer and thermal management which were shown in chapter 1 to be crucial for devices operating under large irradiation concentrations. With dedicated thermal management, detailed 2-dimensional multi-physics modeling predicted high performance. Changing the flow rate of the IPEC device lead to the formation of two distinct regions of operation of the device. Two competing operational parameter spaces were observed: i) thermal effects enhance performance in the zone of low operational current density, and ii) mass transport limits dominate in the zone of high operational current density (saturation current of the electrolyzer component). These competing effects lead to tradeoffs between device efficiency and hydrogen evolution rate, which were quantified using Pareto frontiers. The effects of various operational (irradiation concentration, reactant flow rate), material (catalytic exchange current density, active specific surface area), and dimensional (membrane/separator thickness, gas diffusion layer thickness, catalyst layer thickness) parameters on the objective functions of the STH efficiency and the output production rate were quantified. The performance was found to be quite sensitive to the parameters of irradiation concentration, reactant flow rate, membrane thickness, and exchange current density and not very sensitive to all the rest parameters analyzed. Smart thermal management – only possible through integrated device design – helped in achieving efficient and low-cost production of solar fuels, and could further alleviate degradation-related performance decreases over the lifetime of the device. IPEC device designs combined with smart thermal management proved to be a practical and economically feasible approach to solar fuel processing, and allow circumventing limitations imposed by materials. The work opens new pathways for smart application of thermal management in photoelectrochemical devices providing guidance towards practical realization of high performant PECs.

In *chapter 3*, the conversion of solar energy into chemical fuels via IPEC devices is further numerically investigated by assessing their reaction to time-dependent changes in the operating conditions and the material properties. This is achieved by deploying the model developed in chapter 1 and 2 to further include the degradation of various components. The degradation of the materials over the lifetime of the device as well as the daily and seasonal changes in incoming irradiation pose a challenge for the stable and secure supply of fuel from such devices. To tackle these

issues, performance optimization strategies were developed utilizing adaptation of operational conditions. The water mass flow controller is shown to act as an optimum power point tracker for the IPEC device. This helped in achieving stabilized efficiency and production during the daily irradiation variations where production increase in the range of 1-8% is shown to be achieved using just a mass flow rate controlling profile. The developed strategies highlight that the operation of the IPEC during the complete lifetime should be considered in addition to the initial design point of the device. The developed strategies show that mass flow control is a powerful tool for efficient device operation and degradation alleviation, allowing to exclude any external power electronics and providing an opportunity for the dynamic response of PEC devices. The work enables PEC devices to produce in a stable, reliable, durable and robust way in spite of sustained/fluctuating disturbances.

In *chapter* 4, the learnings from the previous chapters have been implemented to realize a lab-scale prototype with 4 cm^2 photoactive area and 25 cm^2 electrochemical active area working under concentrated irradiation. Achieving high current densities while keeping a good energy conversion efficiency is one of the main challenges to enhance the competitiveness of photoelectrochemical devices for solar fuels production. In this chapter, a CIPEC water splitting device was demonstrated that can reach current densities higher than 0.88 A/cm$_{EC}^2$, with an STH conversion efficiency of 17.2 % (based on Gibb's free energy). That high current density, which was reached thanks to irradiation concentration (up to 474, realized with good homogeneity through high flux solar simulator) combined with a patented innovative smart thermal management concept, is the highest reported for an integrated photoelectrochemical device to the best of the knowledge and is in industrially relevant magnitude. The photoabsorber and electrocatalysts were implemented in direct contact where an innovative design approach allowed for active thermal management between them, and for close electronic integration which limited overall connection resistance to few milliohms. Thermal management is shown to reduce the losses in an intermediate-high current density range and enables operation at even larger concentrations. Performance, dynamic response, and stability testing (> 2 hours) for the device was presented, demonstrating the device's ability to produce hydrogen with high efficiency in varying conditions, and over a long period of time. The device operates at the largest demonstrated output power of 27 W, opening a pathway towards scalable and large-scale deployment of PEC water splitting. The prototype design, implementation-testing approach and fast prototyping methods disclosed here would benefit the community in studying various other photoelectrochemical approaches. The demonstrated approach has the potential to produce solar-fuel with performance better than other concentrated/non-concentrated approaches and at costs competitive to those of

conventional fossil fuels, providing promising pathways for a hydrogen-based renewable future.

Some suggestions for the future work are presented herewith. Though, the model developed and detailed in the thesis is one of the most complete yet computationally economic, there are certain physical phenomena which could be included in the model to make it even more complete.

One suggestion is to incorporate the multi-phase mass transfer modeling, including bubble evolution and transport. The evolution of hydrogen and oxygen leads to bubble creation (with liquid water as input). This is critical specifically for the oxygen evolution on the anode side as it contains liquid water in the anodic chamber and hence has two-phase flow. Due to this evolution of the bubbles, the over-potential for the electrochemical reaction may increase and would demand more driving force to carry out the reaction. The bubbles may also lead to blocking of active electrocatalytic sites [149], [150]. Hence it is of much importance to study the effects of bubble formation and transport. These phenomena can be modeled in COMSOL® by laminar two-phase flow and phase fields which describes the two-phase flow dynamics using a Cahn- Hilliard equation [151].

The model currently doesn't account for optical simulation in the concentrator and hence to optimize the concentrator by reducing the optical losses as well as by increasing the range of the spectrum going to the PV, it is proposed to develop a coupled ray-tracing model for concentrator using Monte Carlo method. This implementation could be based on the VEGAS 2011 platform which is a MC ray tracing code developed at ETH Zurich [152].

Our integrated solar driven water splitting demonstrator can even use water in gas phase i.e. water vapor as the reactant. The humid air's content of water vapor (under normal temperature and humidity conditions) is significant enough to provide the needed water flux. In fact, using water vapor instead of liquid reactant as the input has several potential advantages. Blocking of active electrocatalytic sites [14], [149], [150], as well as other adverse effects (mentioned previously) which are associated with bubble formation, are alleviated by using water vapor as the feedstock. An additional benefit comes from the less driving force required for the gaseous water than for the liquid water reaction [49]. However, feeding $H_2O(g)$ to the integrated photoelectrolysis system presents challenges with respect to ionic transport, and reactant and product gas transport. In this regard, the model could be extended (including vapor's temperature dependent properties and updated diffusivities) and used to analyze device's performance when fed with vapor. Based on the modeling work the updates could be made to the demonstrator prototype which could be used

to carry out experiments proving the concept. Though it should be noted that operating with air based water vapor would have much lower saturation current of the electrochemical component thus limiting the overall operating current density of the device. This approach could be practically viable only for cheaper photo-active/catalyst materials and for applications which do not require high photoelectrochemical current density operation.

The thesis has led the way towards the development of a scalable prototype for solar based hydrogen as well as on-site power and heat generation. The said prototype's development work is in progress. Two of the most important results of the thesis' work, which led to the invention of a cost-effective efficient H_2 generation pathway, are the development of thermal management strategies (smartly taking heat from electrolyzer and supplying it to the photoactive part) at high concentration of light that result in efficiency enhancements; and the design and development of controller/controlling strategies utilizing only water mass flow controlling to actively track the optimum power point of the system during the day and in turn counteract the adverse effects of device degradation. My aim is to take the lab-scale demonstration and proof-of-principle and develop a technology which can be scaled into a real product. The integrated design allowing smart thermal management for optimized efficiency and the mass flow based controller for optimum power point tracking has been patented under the international patent application no. PCT/IB2017/055019 filed on August 18, 2017 claiming priority of the "Provisional" European Patent Application no. EP16020308.9 filed on August 19, 2016 and the US provisional patent Application no. 62/376,923 filed on August 19, 2016.

Following the promising results of the lab-scale prototype, I started working towards the scaled-up prototype whose design is shown in Fig 5.1. The prototype is planned to have a collector (parabolic concentrator) area of 40 m^2, with the potential to produce 12 kW of electrical power along with ~16 kW of heat. The prototype's H_2 generation potential is 2 kg/day (fully solar, only day operation) and more for combined off-peak grid electricity based operation. At current Swiss electricity prices and consumption, the prototype could power 5 average Swiss households. With this prototype, my aim is to achieve a full-fledged co-generation system capable of producing heat, electricity, and fuel, for which a system level design is already in place. Furthermore, it is of prime importance and challenging for the photovoltaic component to receive homogenous/uniform light flux from the parabolic dish collector for which the work on developing a novel homogenizer is ongoing.

Product ratios among heat, fuel and electricity can be freely tuned depending on the needs of consumer. Though this flexibilszation would require modeling and

development of a smart switch (to be integrated at photovoltaic-catalyst interface) and the aperture controller (to be integrated in the flux homogenizer). Research work is planned to explore and quantify these co-generation abilities of the system which is expected to push the efficiency up to 70%. My aim is to connect the prototype to a compressed hydrogen storage facility, integrate it in a complete energy generation-distribution-utilization simulator system (i.e. EPFL's Distributed Electrical Systems Laboratory's smart grid system simulating large-scale integration of renewable's into grid infrastructures), and test it for an elongated time under realistic on-sun conditions gathering extensive diagnostics data.
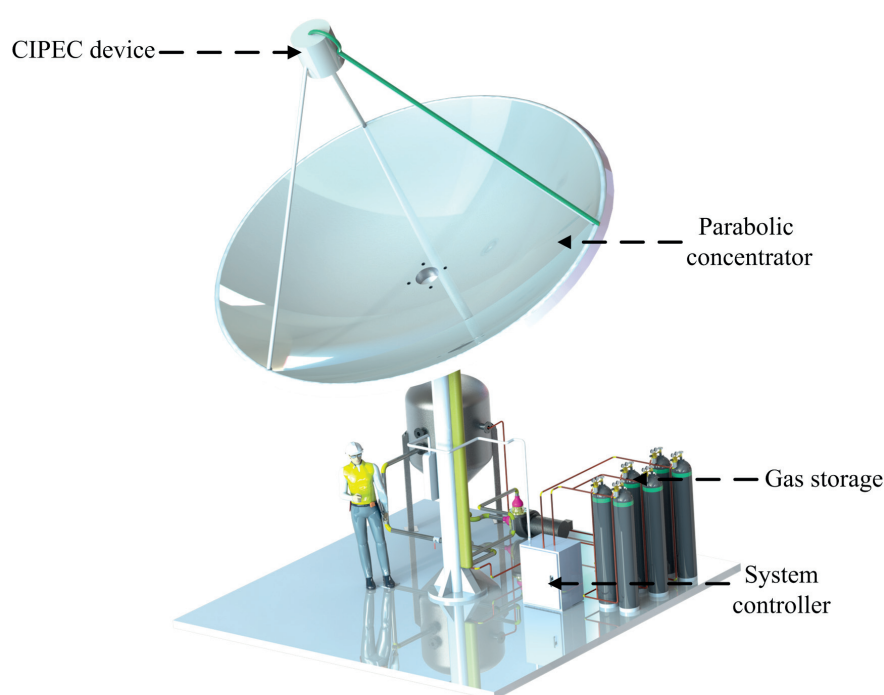
Fig. 5.1 The schematic showing the design of the product-scale prototype incorporating a parabolic concentrator with the patented concentrated integrated photoelectrochemical device and system controller.

In summary, the thesis provided detailed model to analyse and design a PEC, presented deployment of thermal management smartly to improve and optimize performance, provided reactant flow based innovative controlling method to tackle the inherent disturbances and disclosed the recipe for fast prototyping of high efficient high current density PECs which could be used in the community for not

only researching solar-driven production of hydrogen but photoeectrochemical genration of any chemical. The thesis provides a pathway towards practical implementation of solar fuel generation approaches and helps in bridging the current gap between PEC research and its industrial realization.

Bibliography

[1]   S. Solomon, "Climate change 2007-the physical science basis: Working group I contribution to the fourth assessment report of the IPCC," Cambridge University Press, 2007.

[2]   C. von S. O. Edenhofer, R. Pichs-Madruga, Y. Sokona, K. Seyboth, P. Matschoss, S. Kadner, T. Zwickel, P. Eickemeier, G. Hansen, S. Schlömer and O. Edenhofer, "IPCC special report on renewable energy sources and climate change mitigation," Cambridge University Press, Cambridge, United Kingdom and New York, NY, USA, 2011.

[3]   N. S. Lewis and D. G. Nocera, "Powering the planet: chemical challenges in solar energy utilization.," *Proc. Natl. Acad. Sci. U. S. A.*, vol. 103, no. 43, pp. 15729–35, Oct. 2006.

[4]   N. S. Lewis, G. Crabtree, A. J. Nozik, M. R. Wasielewski, P. Alivisatos, H. Kung, J. Tsao, E. Chandler, W. Walukiewicz, M. Spitler, R. Ellingson, R. Overend, J. Mazer, M. Gress, J. Horwitz, C. Ashton, B. Herndon, L. Shapard, and R. M. Nault, "Basic Research Needs for Solar Energy Utilization. Report of the Basic Energy Sciences Workshop on Solar Energy Utilization, April 18-21, 2005," US Department of Energy, Office of Basic Energy Science, 2005.

[5]   B. C. R. Ewan and R. W. K. Allen, "A figure of merit assessment of the routes to hydrogen," *Int. J. Hydrogen Energy*, vol. 30, no. 8, pp. 809–819, Jul. 2005.

[6]   J. Turner, G. Sverdrup, M. K. Mann, P. Maness, B. Kroposki, M. Ghirardi, R. J. Evans, and D. Blake, "Renewable hydrogen production," *Int. J. Energy Res.*, vol. 32, no. 5, pp. 379–407, 2008.

[7]   J. A. Turner, "A Realizable Renewable Energy Future," *Science (80-.).*, vol.

285, no. 5428, pp. 687–689, Jul. 1999.

[8]   J. A. Turner, "Sustainable hydrogen production," *Science (80-.).*, vol. 305, no. 5686, pp. 972–974, 2004.

[9]   M. A. Rosen, "Advances in hydrogen production by thermochemical water decomposition: a review," *Energy*, vol. 35, no. 2, pp. 1068–1076, 2010.

[10]   P. C. Hallenbeck and J. R. Benemann, "Biological hydrogen production; fundamentals and limiting processes," *Int. J. Hydrogen Energy*, vol. 27, no. 11, pp. 1185–1193, 2002.

[11]   K. Nath and D. Das, "Improvement of fermentative hydrogen production: various approaches," *Appl. Microbiol. Biotechnol.*, vol. 65, no. 5, pp. 520–529, 2004.

[12]   R. C. Prince and H. S. Kheshgi, "The photobiological production of hydrogen: potential efficiency and effectiveness as a renewable fuel," *Crit. Rev. Microbiol.*, vol. 31, no. 1, pp. 19–31, 2005.

[13]   K. T. Fountaine, H. J. Lewerenz, and H. A. Atwater, "Efficiency limits for photoelectrochemical water-splitting," *Nat. Commun.*, vol. 7, 2016.

[14]   O. Khaselev and J. A. Turner, "A Monolithic Photovoltaic-Photoelectrochemical Device for Hydrogen Production via Water Splitting," *Science (80-.).*, vol. 280, no. 5362, pp. 425–427, Apr. 1998.

[15]   F. Nandjou and S. Haussener, "Degradation in photoelectrochemical devices: review with an illustrative case study," *J. Phys. D. Appl. Phys.*, vol. 50, no. 12, p. 124002, Mar. 2017.

[16]   M. G. Walter, E. L. Warren, J. R. McKone, S. W. Boettcher, Q. Mi, E. A. Santori, and N. S. Lewis, "Solar water splitting cells," *Chem. Rev.*, vol. 110, no. 11, pp. 6446–6473, 2010.

[17]   L. Zhou, Q. Yan, A. Shinde, D. Guevarra, P. F. Newhouse, N. Becerra-Stasiewicz, S. M. Chatman, J. A. Haber, J. B. Neaton, and J. M. Gregoire, "High Throughput Discovery of Solar Fuels Photoanodes in the CuO-V$_2$O$_5$ System," *Adv. Energy Mater.*, vol. 5, no. 22, p. 1500968, Nov. 2015.

[18]   U. S. E. I. Administration, "A n n u a l n e r g y Ou t l o o k."

[19]   T. J. Jacobsson, V. Fjällström, M. Edoff, and T. Edvinsson, "Sustainable solar hydrogen production: from photoelectrochemical cells to PV-electrolyzers and back again," *Energy Environ. Sci.*, vol. 7, no. 7, pp. 2056–2070, 2014.

[20]   B. A. Pinaud, J. D. Benck, L. C. Seitz, A. J. Forman, Z. Chen, T. G. Deutsch, B. D. James, K. N. Baum, G. N. Baum, S. Ardo, H. Wang, E. Miller, and T. F. Jaramillo, "Technical and economic feasibility of centralized facilities for solar hydrogen production via photocatalysis and photoelectrochemistry," *Energy Environ. Sci.*, vol. 6, no. 7, p. 1983, 2013.

[21]   M. Dumortier, S. Tembhurne, and S. Haussener, "Holistic design guidelines for solar hydrogen production by photo-electrochemical routes," *Energy Environ. Sci.*, vol. 8, no. 12, pp. 3614–3628, 2015.

[22]   S. Haussener, S. Hu, C. Xiang, A. Z. Weber, and N. S. Lewis, "Simulations of the irradiation and temperature dependence of the efficiency of tandem photoelectrochemical water-splitting systems," *Energy Environ. Sci.*, vol. 6, no. 12, p. 3605, 2013.

[23]   M. A. Modestino and S. Haussener, "An Integrated Device View on Photo-Electrochemical Solar-Hydrogen Generation," *Annu. Rev. Chem. Biomol. Eng.*, vol. 6, no. 1, pp. 13–34, Jul. 2015.

[24]   M. Dumortier and S. Haussener, "Design guidelines for concentrated photo-electrochemical water splitting devices based on energy and greenhouse gas yield ratios," *Energy Environ. Sci.*, vol. 8, no. 11, pp. 3069–3082, 2015.

[25]   E. B. Fox and H. R. Colon-Mercado, "Mass Transport Limitations in Proton Exchange Membrane Fuel Cells and Electrolyzers," in *Mass Transfer - Advanced Aspects*, InTech, 2011.

[26]   P. Singh and N. M. Ravindra, "Temperature dependence of solar cell performance—an analysis," *Sol. Energy Mater. Sol. Cells*, vol. 101, pp. 36–45, 2012.

[27]   Y. Sone, P. Ekdunge, and D. Simonsson, "Proton Conductivity of Nafion 117 as Measured by a Four-Electrode AC Impedance Method," *J. Electrochem. Soc.*, vol. 143, no. 4, p. 1254, 1996.

[28]   R. E. Rocheleau and E. L. Miller, "Photoelectrochemical production of hydrogen: Engineering loss analysis," *Int. J. Hydrogen Energy*, vol. 22, no. 8, pp. 771–782, Aug. 1997.

[29]   A. Berger and J. Newman, "An Integrated 1-Dimensional Model of a Photoelectrochemical Cell for Water Splitting," *J. Electrochem. Soc.*, vol. 161, no. 8, pp. E3328–E3340, Jun. 2014.

[30]   Y. K. Gaudy and S. Haussener, "Utilizing modeling, experiments, and statistics for the analysis of water-splitting photoelectrodes," *J. Mater. Chem. A*, vol. 4, no. 8, pp. 3100–3114, 2016.

[31]   S. Haussener, C. Xiang, J. M. Spurgeon, S. Ardo, N. S. Lewis, and A. Z. Weber, "Modeling, simulation, and design criteria for photoelectrochemical water-splitting systems," *Energy Environ. Sci.*, vol. 5, no. 12, p. 9922, 2012.

[32]   V. Zagolla, E. Tremblay, and C. Moser, "Proof of principle demonstration of a self-tracking concentrator," *Opt. Express*, vol. 22, no. 102, pp. A498–A510, 2014.

[33]   R. Manual, "Comsol Multiphysics®v. 4.3b, www.comsol.com," *Comsol Multiphysics®v. 4.3b, www.comsol.com*, p. COMSOL AB,Stockholm, Sweden.

[34]   Y. Liu, Y. Sun, and A. Rockett, "A new simulation software of solar cells—wxAMPS," *Sol. Energy Mater. Sol. Cells*, vol. 98, pp. 124–128, 2012.

[35]   R. K. Shevgaonkar, *Electromagnetic waves*. Tata McGraw-Hill, 2006.

[36]   M. Schubert, V. Gottschalch, C. M. Herzinger, H. Yao, P. G. Snyder, and J. A. Woollam, "Optical constants of GaxIn1-xP lattice matched to GaAs," *J. Appl. Phys.*, vol. 77, no. 7, pp. 3416–3419, Apr. 1995.

[37]   E. D. Palik, *Handbook of optical constants of solids*. Academic Press, 1998.

[38]   R. W. Collins and K. Vedam, "Optical properties of solids," *Encycl. Appl. Phys.*, vol. 12, p. 285, 1995.

[39]   S. M. Sze and K. K. Ng, *Physics of Semiconductor Devices*, vol. 10. John Wiley & Sons, 2006.

[40]   U. Lindefelt, "Current-density relations for nonisothermal modeling of degenerate heterostructure devices," *J. Appl. Phys.*, vol. 75, no. 2, pp. 958–966, 1994.

[41]   E. A. Schiff, "Transport, Interfaces, and Modeling in Amorphous Silicon Based Solar Cells: Final Technical Report, 11 February 2002 - 30 September

2006," 2008.

[42]   A. Damjanovic, A. Dey, and J. O. Bockris, "Kinetics of oxygen evolution and dissolution on platinum electrodes," *Electrochim. Acta*, vol. 11, no. 7, pp. 791–814, Jul. 1966.

[43]   L. B. Kriksunov, L. V. Bunakova, S. E. Zabusova, and L. I. Krishtalik, "Anodic oxygen evolution reaction at high temperatures in acid solutions at platinum," *Electrochim. Acta*, vol. 39, no. 1, pp. 137–142, Jan. 1994.

[44]   K. (Kim) Kinoshita, *Electrochemical oxygen technology*. John Wiley & Sons, 1992.

[45]   N. M. Markovic, B. N. Grgur, and P. N. Ross, "Temperature-Dependent Hydrogen Electrochemistry on Platinum Low- Index Single-Crystal Surfaces in Acid Solutions," *J. Phys. Chem. B*, vol. 101, no. 27, pp. 5405–5413, 1997.

[46]   W. Sheng, H. A. Gasteiger, and Y. Shao-Horn, "Hydrogen Oxidation and Evolution Reaction Kinetics on Platinum: Acid vs Alkaline Electrolytes," *J. Electrochem. Soc.*, vol. 157, no. 11, p. B1529, Nov. 2010.

[47]   U. Lindefelt, "Heat generation in semiconductor devices," *J. Appl. Phys.*, vol. 75, no. 2, pp. 942–957, 1994.

[48]   J. Arch, J. Cuiffi, J. Hou, W. Howland, A. Moquin, M. Rogosky, and T. Tran, "AMPS-1D Manual."

[49]   A. J. Bard and L. R. Faulkner, *Electrochemical methods : fundamentals and applications*. Wiley New York, 2001.

[50]   D. A. Nield and A. Bejan, *Convection in porous media*. Springer, 2013.

[51]   M. Le Bars, M. G. Worster, M. Le Bars, and M. G. Worster, "Interfacial conditions between a pure fluid and a porous medium : implications for binary alloy solidification," *J. Fluid Mech.*, vol. 550, pp. 149–173, 2006.

[52]   R. B. Bird, E. N. Lightfoot, and W. Stewart, *Transport phenomena*. John Wiley & Sons, 2007.

[53]   C. F. Curtiss and R. B. Bird, "Multicomponent Diffusion," *Ind. Eng. Chem. Res.*, vol. 38, no. 7, pp. 2515–2522, 1999.

[54]   F. P. Incropera, *Fundamentals of Heat and Mass Transfer, Seventh Edition*. John

Wiley and Sons, 2011.

[55]   J. R. Lloyd and W. R. Moran, "Natural Convection Adjacent to Horizontal Surface of Various Planforms," *J. Heat Transfer*, vol. 96, no. 4, pp. 443–447, Nov. 1974.

[56]   S. R. Kurtz, D. Myers, and J. M. Olson, "Projected performance of three- and four-junction devices using GaAs and GaInP," in *IEEE Photovoltaics Specialists Conference*, 1997, vol. 26, pp. 875–878.

[57]   A. W. Haas, J. R. Wilcox, J. L. Gray, and R. J. Schwartz, "Design of a GaInP/GaAs tandem solar cell for maximum daily, monthly, and yearly energy output," *J. Photonics Energy*, vol. 1, no. 1, p. 18001, Jan. 2011.

[58]   B. Van Zeghbroeck, *Principles of Semiconductor Devices*. Colorado University, 2011.

[59]   A. (Adolfas) Dargys and J. (Jurgis) Kundrotas, *Handbook on physical properties of Ge, Si, GaAs and InP*. Science and Encyclopedia Publishers, 1994.

[60]   M. Levinshtein, S. Rumyantsev, and M. Shur, *Handbook Series on Semiconductor Parameters*, vol. 1. WORLD SCIENTIFIC, 1996.

[61]   M. Carmo, D. L. Fritz, J. Rgen Mergel, and D. Stolten, "A comprehensive review on PEM water electrolysis," *Int. J. Hydrogen Energy*, vol. 38, pp. 4901–4934, 2013.

[62]   H. Ito, T. Maeda, A. Nakano, and H. Takenaka, "Properties of Nafion membranes under PEM water electrolysis conditions," *Int. J. Hydrogen Energy*, vol. 36, no. 17, pp. 10527–10540, Aug. 2011.

[63]   E. W. Lemmon, M. O. McLinden, D. G. Friend, P. Linstrom, and W. Mallard, "NIST chemistry webbook," *NIST Stand. Ref. database*, vol. 69, 2005.

[64]   R. W. Powell, R. P. Tye, and M. J. Woodman, "The thermal conductivity and electrical resistivity of polycrystalline metals of the platinum group and of single crystals of ruthenium," *J. Less Common Met.*, vol. 12, no. 1, pp. 1–10, 1967.

[65]   D. Qingwen, W. Xiaoliang, X. Hongling, M. Zeyu, Z. Xiaobin, H. Qifeng, L. Jinmin, and W. Zhanguo, "Theoretical investigation of efficiency of a pa-SiC: H/ia-Si: H/n-μc-Si solar cell," *J. Semicond.*, vol. 31, no. 10, p. 103003, 2010.

[66]   A. Belfar and R. Mostefaoui, "Simulation of n1-p2 Microcrystalline Silicon Tunnel Junction with AMPS-1D in a-Si :H/μc-Si :H Tandem Solar Cells," *J. Appl. Sci.*, vol. 11, no. 16, pp. 2932–2939, Dec. 2011.

[67]   M. Sugiyama, A. Nakamura, K. Watanabe, Y. Ota, K. Nishioka, Y. Nakano, and K. Fujii, "Concentrated photovoltaic electrochemical cell (CPEC): A route toward high-efficiency, cost-effective solar hydrogen production," in *2015 IEEE 42nd Photovoltaic Specialist Conference (PVSC)*, 2015, pp. 1–4.

[68]   A. Nakamura, Y. Ota, K. Koike, Y. Hidaka, K. Nishioka, M. Sugiyama, and K. Fujii, "A 24.4% solar to hydrogen energy conversion efficiency by combining concentrator photovoltaic modules and electrochemical cells," *Appl. Phys. Express*, vol. 8, no. 10, p. 107101, Oct. 2015.

[69]   G. Peharz, F. Dimroth, and U. Wittstadt, "Solar hydrogen production by water splitting with a conversion efficiency of 18%," *Int. J. Hydrogen Energy*, vol. 32, no. 15, pp. 3248–3252, Oct. 2007.

[70]   M. R. Lueck, C. L. Andre, A. J. Pitera, M. L. Lee, E. A. Fitzgerald, and S. A. Ringel, "Dual Junction GaInP / GaAs Solar Cells Grown on Metamorphic SiGe / Si Substrates With High Open Circuit Voltage," *IEEE Electron Device Lett.*, vol. 27, no. 3, pp. 142–144, 2006.

[71]   K. E. Ayers, E. B. Anderson, C. B. Capuano, B. D. Carter, L. T. Dalton, G. Hanlon, J. Manco, and M. Niedzwiecki, "Research Advances Towards Low Cost, High Efficiency PEM Electrolysis," in *ECS Transactions*, 2010, vol. 33, no. 1, pp. 3–15.

[72]   J. Kim, S. Lee, S. Srinivasan, and C. E. Chamberlin, "Modeling of Proton Exchange Membrane Fuel Cell Performance with an Empirical Equation," *J. Electrochem. Soc.*, vol. 142, no. 8, p. 2670, 1995.

[73]   M. A. Green, "Solar cell fill factors: General graph and empirical expressions," *Solid State Electron.*, vol. 24, no. 8, pp. 788–789, Aug. 1981.

[74]   H. Döscher, J. L. Young, J. F. Geisz, J. A. Turner, and T. G. Deutsch, "Solar-to-hydrogen efficiency: shining light on photoelectrochemical device performance," *Energy Environ. Sci.*, vol. 9, no. 1, pp. 74–80, 2016.

[75]   S. Tembhurne and S. Haussener, "Integrated Photo-Electrochemical Solar Fuel Generators under Concentrated Irradiation II. Thermal Management a Crucial Design Consideration," *J. Electrochem. Soc.*, vol. 163, no. 10, pp. 999–

1007, 2016.

[76] J. Newman, "Scaling with Ohm's Law; Wired vs. Wireless Photoelectrochemical Cells," *J. Electrochem. Soc.*, vol. 160, no. 3, pp. F309–F311, Jan. 2013.

[77] S. A. Bonke, M. Wiechen, D. R. MacFarlane, and L. Spiccia, "Renewable fuels from concentrated solar power: towards practical artificial photosynthesis," *Energy Environ. Sci.*, vol. 8, no. 9, pp. 2791–2796, 2015.

[78] S. Tembhurne and S. Haussener, "Integrated Photo-Electrochemical Solar Fuel Generators under Concentrated Irradiation I. 2-D Non-Isothermal Multi-Physics Modeling," *J. Electrochem. Soc.*, vol. 163, no. 10, pp. 988–998, 2016.

[79] J. W. Ager, M. R. Shaner, K. A. Walczak, I. D. Sharp, and S. Ardo, "Experimental demonstrations of spontaneous, solar-driven photoelectrochemical water splitting," *Energy Environ. Sci.*, vol. 8, no. 8, pp. 2811–2824, 2015.

[80] W. J. Chang, K.-H. Lee, H. Ha, K. Jin, G. Kim, S.-T. Hwang, H. Lee, S.-W. Ahn, W. Yoon, H. Seo, J. S. Hong, Y. K. Go, J.-I. Ha, and K. T. Nam, "Design Principle and Loss Engineering for Photovoltaic–Electrolysis Cell System," *ACS Omega*, vol. 2, no. 3, pp. 1009–1018, Mar. 2017.

[81] J. L. Young, M. A. Steiner, H. Döscher, R. M. France, J. A. Turner, and T. G. Deutsch, "Direct solar-to-hydrogen conversion via inverted metamorphic multi-junction semiconductor architectures," *Nat. Energy*, vol. 2, no. 4, 2017.

[82] J.-W. Schüttauf, M. A. Modestino, E. Chinello, D. Lambelet, A. Delfino, D. Dominé, A. Faes, M. Despeisse, J. Bailat, D. Psaltis, C. Moser, and C. Ballif, "Solar-to-Hydrogen Production at 14.2% Efficiency with Silicon Photovoltaics and Earth-Abundant Electrocatalysts," *J. Electrochem. Soc.*, vol. 163, no. 10, pp. F1177–F1181, Aug. 2016.

[83] J. Luo, J.-H. Im, M. T. Mayer, M. Schreier, M. K. Nazeeruddin, N.-G. Park, S. D. Tilley, H. J. Fan, and M. Grätzel, "Water photolysis at 12.3% efficiency via perovskite photovoltaics and Earth-abundant catalysts," *Science (80-.).*, vol. 345, no. 6204, pp. 1593–1596, 2014.

[84] A. Fallisch, L. Schellhase, J. Fresko, M. Zedda, J. Ohlmann, M. Steiner, A. Bösch, L. Zielke, S. Thiele, F. Dimroth, and T. Smolinka, "Hydrogen

concentrator demonstrator module with 19.8% solar-to-hydrogen conversion efficiency according to the higher heating value," *Int. J. Hydrogen Energy*, vol. 42, no. 43, pp. 26804–26815, 2017.

[85] S. Licht, B. Wang, S. Mukerji, T. Soga, M. Umeno, and H. Tributsch, "Efficient Solar Water Splitting, Exemplified by RuO 2 -Catalyzed AlGaAs/Si Photoelectrolysis," *J. Phys. Chem. B*, vol. 104, no. 38, pp. 8920–8924, 2000.

[86] S. Tembhurne, F. Nadjou, and S. Haussener, "Experimental demonstration of an efficient and scalable integrated photo-electrochemical hydrogen generation device operating under concentrated solar irradiation," 2018.

[87] F. Fouda-Onana, "AST Protocols for PEM Water Electrolyis: Insights on performances and components degradation," in *2nd international workshop on durabiltiy and degradation issues in PEM electrolysis cells and its components*, 2016.

[88] M. Chandesris, V. M. Edeau, N. Guillet, S. Chelghoum, D. Thoby, and F. Fouda-Onana, "Membrane degradation in PEM water electrolyzer: Numerical modeling and experimental evidence of the influence of temperature and current density," *Int. J. Hydrogen Energy*, vol. 40, pp. 1353–1366, 2015.

[89] A. Fallisch, L. Schellhase, J. Fresko, M. Zechmeister, M. Zedda, J. Ohlmann, L. Zielke, N. Paust, and T. Smolinka, "Investigation on PEM water electrolysis cell design and components for a HyCon solar hydrogen generator," *Int. J. Hydrogen Energy*, vol. 42, no. 19, pp. 13544–13553, 2017.

[90] T. Bak, J. Nowotny, M. Rekas, and C. C. Sorrell, "Photo-electrochemical hydrogen generation from water using solar energy. Materials-related aspects," *Int. J. Hydrogen Energy*, vol. 27, no. 27, pp. 991–1022, 2002.

[91] S. Chen and L. Wang, "Thermodynamic Oxidation and Reduction Potentials of Photocatalytic Semiconductors in Aqueous Solution Thermodynamic Oxidation and Reduction Potentials of Photocatalytic Semiconductors in Aqueous Solution," *Chem. Mater.*, vol. 3666, no. 1, pp. 1–5, 2012.

[92] M. Grätzel, "Photoelectrochemical cells," *Nature*, vol. 414, no. 6861, pp. 338–344, Nov. 2001.

[93] B. Coelho, a. C. Oliveira, and a. Mendes, "Concentrated solar power for renewable electricity and hydrogen production from water—a review," *Energy*

Environ. Sci., vol. 3, no. 10, p. 1398, 2010.

[94]   J. Jia, L. C. Seitz, J. D. Benck, Y. Huo, Y. Chen, J. Wei, D. Ng, T. Bilir, J. S. Harris, and T. F. Jaramillo, "ARTICLE Solar water splitting by photovoltaic-electrolysis with a solar-to-hydrogen efficiency over 30%," *Nat. Publ. Gr.*, vol. 7, 2016.

[95]   K. Fujii, S. Nakamura, M. Sugiyama, K. Watanabe, B. Bagheri, and Y. Nakano, "Characteristics of hydrogen generation from water splitting by polymer electrolyte electrochemical cell directly connected with concentrated photovoltaic cell," *Int. J. Hydrogen Energy*, vol. 38, pp. 14424–14432, 2013.

[96]   H. Cotal, C. Fetzer, J. Boisvert, G. Kinsey, R. King, P. Hebert, H. Yoon, and N. Karam, "III–V multijunction solar cells for concentrating photovoltaics," *Energy Environ. Sci.*, vol. 2, no. 2, pp. 174–192, 2009.

[97]   J. C. Stevens and A. Z. Weber, "A Computational Study of Optically Concentrating, Solar-Fuels Generators from Annual Thermal- and Fuel-Production Efficiency Perspectives," *J. Electrochem. Soc.*, vol. 163, no. 7, pp. H475–H484, 2016.

[98]   S. R. Samms, S. Wasmus, and R. F. Savinell, "Thermal Stability of Nafion® in Simulated Fuel Cell Environments," *J. Electrochem. Soc.*, vol. 143, no. 5, pp. 1498–1504, 1996.

[99]   J. Mali, P. Mazú, M. Paidar, T. Bystron, and K. Bouzek, "Nafion 117 stability under conditions of PEM water electrolysis at elevated temperature and pressure," 2016.

[100]   C. Rozain and P. Millet, "Electrochemical characterization of Polymer Electrolyte Membrane Water Electrolysis Cells," *Hamann, Carl H. Vielstich, Wolf*, vol. 4, pp. 160–167, 2005.

[101]   Y. Cheng and S. Ping Jiang, "Advances in electrocatalysts for oxygen evolution reaction of water electrolysis-from metal oxides to carbon nanotubes," *Prog. Nat. Sci. Mater. Int.*, vol. 25, pp. 545–553, 2015.

[102]   E. Fabbri, A. Habereder, K. Waltar, R. Kötz, and T. J. Schmidt, "Developments and perspectives of oxide-based catalysts for the oxygen evolution reaction," *Catal. Sci. Technol.*, vol. 4, no. 11, pp. 3800–3821, 2014.

[103]   F. M. Sapountzi, J. M. Gracia, K.-J. Weststrate, H. O. A. Fredriksson, and H.

Niemantsverdriet, "Electrocatalysts for the generation of hydrogen, oxygen and synthesis gas," *Prog. Energy Combust. Sci.*, vol. 58, pp. 1–35, 2017.

[104] G. Siefer and A. W. Bett, "Analysis of temperature coefficients for III-V multi-junction concentrator cells," *Prog. Photovoltaics Res. Appl.*, vol. 22, no. 5, pp. 515–524, May 2014.

[105] H. Döscher, J. F. Geisz, T. G. Deutsch, and J. A. Turner, "Sunlight absorption in water – efficiency and design implications for photoelectrochemical devices," *Energy Environ. Sci.*, vol. 7, no. 9, pp. 2951–2956, 2014.

[106] L. Zhu, R. F. Boehm, Y. Wang, C. Halford, and Y. Sun, "Water immersion cooling of PV cells in a high concentration system," *Sol. Energy Mater. Sol. Cells*, vol. 95, no. 2, pp. 538–545, 2011.

[107] Y. Wang, Z. Fang, L. Zhu, Q. Huang, Y. Zhang, and Z. Zhang, "The performance of silicon solar cells operated in liquids," *Appl. Energy*, vol. 86, no. 7–8, pp. 1037–1042, 2009.

[108] X. Han, Q. Wang, J. Zheng, and J. Qu, "Thermal analysis of direct liquid-immersed solar receiver for high concentrating photovoltaic system," *Int. J. Photoenergy*, vol. 2015, 2015.

[109] A. Royne, C. J. Dey, and D. R. Mills, "Cooling of photovoltaic cells under concentrated illumination: a critical review," *Sol. Energy Mater. Sol. Cells*, vol. 86, pp. 451–483, 2005.

[110] T. A. Zawodzinski, C. Derouin, S. Radzinski, R. J. Sherman, V. T. Smith, T. E. Springer, and S. Gottesfeld, "Water Uptake by and Transport Through Nafion® 117 Membranes," *J. Electrochem. Soc.*, vol. 140, no. 4, p. 1041, Apr. 1993.

[111] G. Levêque, R. Bader, W. Lipiński, and S. Haussener, "Experimental and numerical characterization of a new 45 kW$_{el}$ multisource high-flux solar simulator," *Opt. Express*, vol. 24, no. 22, p. A1360, Oct. 2016.

[112] R. Bader, S. Haussener, and W. Lipinski, "Optical Design of Multisource High-Flux Solar Simulators," *J. Sol. Energy Eng.*, vol. 137, no. 2, p. 21012, Oct. 2014.

[113] R. H. Coridan, A. C. Nielander, S. A. Francis, M. T. McDowell, V. Dix, S. M.

Chatman, and N. S. Lewis, "Methods for comparing the performance of energy-conversion systems for use in solar fuels and solar electricity generation," *Energy Environ. Sci.*, vol. 8, no. 10, pp. 2886–2901, 2015.

[114] M. M. May, D. Lackner, J. Ohlmann, F. Dimroth, R. van de Krol, T. Hannappel, and K. Schwarzburg, "On the benchmarking of multi-junction photoelectrochemical fuel generating devices," *Sustain. Energy Fuels*, vol. 1, no. 3, pp. 492–503, 2017.

[115] S. Dugaria, A. Padovan, V. Sabatelli, and D. Del Col, "Assessment of estimation methods of DNI resource in solar concentrating systems," *Sol. Energy*, vol. 121, pp. 103–115, 2015.

[116] P. Bornoz, F. F. Abdi, S. D. Tilley, B. Dam, R. Van De Krol, M. Graetzel, and K. Sivula, "A Bismuth Vanadate−Cuprous Oxide Tandem Cell for Overall Solar Water Splitting," *J. Phys. Chem. C*, vol. 118, no. 30, pp. 16959–16966, Jul. 2014.

[117] X. Wang, K.-Q. Peng, Y. Hu, F.-Q. Zhang, B. Hu, L. Li, M. Wang, X.-M. Meng, and S.-T. Lee, "Silicon/Hematite Core/Shell Nanowire Array Decorated with Gold Nanoparticles for Unbiased Solar Water Oxidation," *Nano Lett.*, vol. 14, no. 1, pp. 18–23, Jan. 2014.

[118] M. R. Shaner, K. T. Fountaine, S. Ardo, R. H. Coridan, H. A. Atwater Bc, and N. S. Lewis, "Photoelectrochemistry of core–shell tandem junction n–p + -Si/n-WO$_3$ microwire array photoelectrodes (O$_2$ /H$_2$O) and resulted in unassisted H 2 production during two-electrode measurements," *Energy Environ. Sci.*, vol. 7, pp. 779–790, 2014.

[119] C. Liu, J. Tang, H. M. Chen, B. Liu, and P. Yang, "A Fully Integrated Nanosystem of Semiconductor Nanowires for Direct Solar Water Splitting," *Nano Lett.*, vol. 13, pp. 2989–2992, 2013.

[120] F. F. Abdi, L. Han, A. H. M. Smets, M. Zeman, B. Dam, and R. Van De Krol, "Efficient solar water splitting by enhanced charge separation in a bismuth vanadate-silicon tandem photoelectrode," *Nat. Commun.*, vol. 4, p. 2195, 2013.

[121] J. Brillet, J.-H. Yum, M. Cornuz, T. Hisatomi, R. Solarska, J. Augustynski, M. Graetzel, and K. Sivula, "Highly efficient water splitting by a dual-absorber tandem cell," *Nat. Photonics*, vol. 6, no. 12, pp. 824–828, Nov. 2012.

[122] C.-Y. Lin, Y.-H. Lai, D. Mersch, and E. Reisner, "Cu$_2$O|NiOx

nanocomposite as an inexpensive photocathode in photoelectrochemical water splitting," *Chem. Sci.*, vol. 3, no. 12, p. 3482, Oct. 2012.

[123] J. H. Park and A. J. Bard, "Photoelectrochemical Tandem Cell with Bipolar Dye-Sensitized Electrodes for Vectorial Electron Transfer for Water Splitting," *Electrochem. Solid-State Lett.*, vol. 9, no. 2, pp. E5–E8, Feb. 2006.

[124] R. C. Kainthla, B. Zelenay, and J. O. Bockris, "Significant Efficiency Increase in Self-Driven Photoelectrochemical Cell for Water Photoelectrolysis," *J. Electrochem. Soc.*, vol. 134, no. 4, pp. 841–845, Apr. 1987.

[125] H. Mettee, J. W. Otvos, and M. Calvin, "Solar induced water splitting with p/n heterotype photochemical diodes: n-Fe$_2$O$_3$/p-GaP," *Sol. Energy Mater.*, vol. 4, pp. 443–453, 1981.

[126] K. Ohashi, J. Mccann, and J. O. Bockris, "Stable photoelectrochemical cells for the splitting of water," *Nature*, vol. 266, no. 5603, pp. 610–611, Apr. 1977.

[127] H. Morisaki, T. Watanabe, M. Iwase, and K. Yazawa, "Photoelectrolysis of water with TiO$_2$ -covered solar-cell electrodes," *Appl. Phys. Lett.*, vol. 29, no. 150, pp. 338–340, 1976.

[128] A. J. Nozik, "*p* - *n* photoelectrolysis cells," *Appl. Phys. Lett.*, vol. 29, no. 3, pp. 150–153, Aug. 1976.

[129] O. Khaselev, A. Bansal, and J. A. Turner, "High-efficiency integrated multijunction photovoltaic/electrolysis systems for hydrogen production," *Int. J. Hydrogen Energy*, vol. 26, no. 2, pp. 127–132, 2001.

[130] Y. Sakai, S. Sugahara, M. Matsumura, Y. Nakato, and H. Tsubomura, "Photoelectrochemical water splitting by tandem type and heterojunction an~orphous silicon electrodes," *CAN. J. CHEM.*, vol. 66, pp. 1853–1856, 1988.

[131] K. Walczak, Y. Chen, C. Karp, J. W. Beeman, M. Shaner, J. Spurgeon, I. D. Sharp, X. Amashukeli, W. West, J. Jin, N. S. Lewis, and C. Xiang, "Modeling, Simulation, and Fabrication of a Fully Integrated, Acid-stable, Scalable Solar-Driven Water-Splitting System," *ChemSusChem*, vol. 8, no. 3, pp. 544–551, Feb. 2015.

[132] L. Han, F. F. Abdi, R. van de Krol, R. Liu, Z. Huang, H.-J. Lewerenz, B. Dam, M. Zeman, and A. H. M. Smets, "Efficient Water-Splitting Device Based on

a Bismuth Vanadate Photoanode and Thin-Film Silicon Solar Cells," *ChemSusChem*, vol. 7, no. 10, pp. 2832–2838, Oct. 2014.

[133] N. Gaillard, Y. Chang, J. Kaneshiro, A. Deangelis, and E. L. Miller, "Status of research on tungsten oxide-based photoelectrochemical devices at the University of Hawaii," *Proc. SPIE*, vol. 7770, pp. 1–14, Aug. 2010.

[134] F. Zhu, J. Hu, I. Matulionis, T. Deutsch, N. Gaillard, A. Kunrath, E. Miller, and A. Madan, "Amorphous silicon carbide photoelectrode for hydrogen production directly from water using sunlight," *Philos. Mag.*, vol. 89, pp. 2723–2739, 2009.

[135] J. Brillet, M. Cornuz, F. Le Formal, J.-H. Yum, M. Grätzel, and K. Sivula, "Examining architectures of photoanode–photovoltaic tandem cells for solar water splitting," *J. Mater. Res.*, vol. 25, no. 1, pp. 17–24, Jan. 2010.

[136] E. L. Miller, D. Paluselli, B. Marsen, and R. E. Rocheleau, "Development of reactively sputtered metal oxide films for hydrogen-producing hybrid multijunction photoelectrodes," *Sol. Energy Mater. Sol. Cells*, vol. 88, no. 2, pp. 131–144, Jul. 2005.

[137] C. R. Cox, J. Z. Lee, D. G. Nocera, and T. Buonassisi, "Ten-percent solar-to-fuel conversion with nonprecious materials.," *Proc. Natl. Acad. Sci. U. S. A.*, vol. 111, no. 39, pp. 14057–61, Sep. 2014.

[138] M. A. Modestino, K. A. Walczak, A. Berger, C. M. Evans, S. Haussener, C. Koval, J. S. Newman, J. W. Ager, and R. A. Segalman, "Robust production of purified H_2 in a stable, self-regulating, and continuously operating solar fuel generator," *Energy Environ. Sci.*, vol. 7, no. 1, pp. 297–301, Dec. 2014.

[139] T. J. Jacobsson, V. Fjällström, M. Sahlberg, M. Edoff, and T. Edvinsson, "A monolithic device for solar water splitting based on series interconnected thin film absorbers reaching over 10% solar-to-hydrogen efficiency," *Energy Environ. Sci.*, vol. 6, p. 3676, 2013.

[140] S. Y. Reece, J. A. Hamel, K. Sung, T. D. Jarvi, A. J. Esswein, J. J. H. Pijpers, and D. G. Nocera, "Wireless Solar Water Splitting Using Silicon-Based Semiconductors and Earth-Abundant Catalysts," *Science (80-.).*, vol. 334, pp. 645–648, 2011.

[141] S. Yamane, N. Kato, S. Kojima, A. Imanishi, S. Ogawa, N. Yoshida, S. Nonomura, and Y. Nakato, "Efficient Solar Water Splitting with a Composite

' n -Si/ p -CuI/ n-i-p a-Si/ n-p GaP/RuO$_2$ ' Semiconductor Electrode," *J. Phys. Chem. C*, vol. 113, no. 32, pp. 14575–14581, Aug. 2009.

[142] N. A. Kelly and T. L. Gibson, "Design and characterization of a robust photoelectrochemical device to generate hydrogen using solar water splitting," *Int. J. Hydrogen Energy*, vol. 31, pp. 1658–1673, 2006.

[143] J. H. Park and A. J. Bard, "Unassisted Water Splitting from Bipolar Pt/Dye-Sensitized TiO$_2$ Photoelectrode Arrays," *Electrochem. Solid-State Lett.*, vol. 8, no. 12, p. G371, Dec. 2005.

[144] Y. Yamada, N. Matsuki, T. Ohmori, H. Mametsuka, M. Kondo, A. Matsuda, and E. Suzuki, "One chip photovoltaic water electrolysis device," *Int. J. Hydrogen Energy*, vol. 28, pp. 1167–1169, 2003.

[145] Richard E. Rocheleau, A. Eric L. Miller, and A. Misra, "High-Efficiency Photoelectrochemical Hydrogen Production Using Multijunction Amorphous Silicon Photoelectrodes," *Energy & Fuels*, vol. 12, pp. 3–10, 1998.

[146] E. Verlage, S. Hu, R. Liu, R. J. R. Jones, K. Sun, C. Xiang, N. S. Lewis, and H. A. Atwater, "A monolithically integrated, intrinsically safe, 10% efficient, solar-driven water-splitting system based on active, stable earth-abundant electrocatalysts in conjunction with tandem III–V light absorbers protected by amorphous TiO $_2$ films," *Energy Environ. Sci.*, vol. 8, no. 11, pp. 3166–3172, 2015.

[147] K. Sun, R. Liu, Y. Chen, E. Verlage, N. S. Lewis, and C. Xiang, "Solar-Driven Water Splitting: A Stabilized, Intrinsically Safe, 10% Efficient, Solar-Driven Water-Splitting Cell Incorporating Earth-Abundant Electrocatalysts with Steady-State pH Gradients and Product Separation Enabled by a Bipolar Membrane (Adv. Energy," *Adv. Energy Mater.*, vol. 6, no. 13, pp. 1–7, 2016.

[148] R. M. Krzysztof Lewinskia, Fuxia Suna, Sean Luopaa, Jiyoung Parka, "Operation of low-temp electrolyzers at very high current densities: A pipe dream or an opportunity?," in *1st International Conference on Electrolysis, Copenhagen*, 2017.

[149] M. Philippe, H. Jérôme, B. Sebastien, and P. Gérard, "Modelling and calculation of the current density distribution evolution at vertical gas-evolving electrodes," *Electrochim. Acta*, vol. 51, no. 6, pp. 1140–1156, 2005.

[150] J. Eigeldinger and H. Vogt, "The bubble coverage of gas-evolving electrodes

in a flowing electrolyte," *Electrochim. Acta*, vol. 45, no. 27, pp. 4449–4456, 2000.

[151] J. Kim, S. Lee, Y. Choi, S.-M. Lee, and D. Jeong, "Basic Principles and Practical Applications of the Cahn–Hilliard Equation," *Math. Probl. Eng.*, vol. 2016, no. 2, pp. 1–11, Oct. 2016.

[152] J. Petrasch, "A free and open source Monte Carlo ray tracing program for concentrating solar energy research," in *ASME 2010 4th International Conference on Energy Sustainability*, 2010, pp. 125–132.

CV

SAURABH TEMBHURNE

CONTACT
INFORMATION

Avenue des cerisiers 03
Crissier, 1023
Switzerland

Mobile:+41-779191294
saurabh.tembhurne@epfl.ch

EDUCATION

Swiss Federal Institute of Technology Lausanne (EPFL), Switzerland   **Sep. 2013-Feb. 2018**

Ph.D. in Energy

- Modeling, design, optimization and implementation of concentrated integrated photoelectrochemical devices for solar fuel generation

Indian Insitute of Technology Bombay, Mumbai, India   **July 2008 - June 2013**

Dual Degree (B.Tech+M.Tech), Department of Electrical Engineering

- Bachelors of Technology in Electrical Engineering and Masters of Technology in Microelectronics.
- Master Thesis: Plasmonic Solar Cell modeling and simulation

PATENTS

- Saurabh TEMBHURNE, Meng LIN, Sophia HAUSSENER. *Integrated Photo-Electrochemical Device for Concentrated Irradiation.* PCT/IB2017/055019, (Patent no. **US** 62/376923 and **EP**16020308.9).

BOOK CHAPTERS

- Sophia Haussener, Yannick Gaudy, Saurabh TEMBHURNE, *Modelling derived design guidelines for photo-electrochemical devices.* Chapter 9, Energy and Environment Series No. 20, Royal Society of Chemistry, 2018.

JOURNAL PUBLICATIONS

- S. Y. Tembhurne, F. Nandjou and S. Haussener. *Experimental demonstration of an efficient and scalable integrated photo-electrochemical hydrogen generation device operating under concentrated solar irradiation*, submitted 2017.
- S. Y. Tembhurne and S. Haussener. *Controlling strategies for concentrated integrated photo-electrochemical devices exposed to fluctuating or sustained disturbances,* in preparation for submission 2018.

- S. Y. Tembhurne and S. Haussener. *Integrated Photo-Electrochemical Solar Fuel Generators under Concentrated Irradiation- Part I: 2-D Non-Isothermal Multi-physics Modeling*, in J. Electrochem. Soc. 2016, 163 (10) H988-H998.
- S. Y. Tembhurne and S. Haussener. *Integrated Photo-Electrochemical Solar Fuel Generators Under Concentrated Irradiation- Part II: Thermal Management a Crucial Design Consideration*, in J. Electrochem. Soc. 2016, 163 (10) H999-H1007.
- M. Dumortier, S. Y. Tembhurne and S. Haussener. *Holistic design guidelines for solar hydrogen production by photoelectrochemical routes*, in Energy Environmental Science, vol. 8, p. 3614 - 3628, 2015.
- Vijay K. Arora, Mastura Shafinaz Zainal Abidin, Saurabh Tembhurne, and Munawar A. Riyadi. *Concentration dependence of drift and magnetoresistance ballistic mobility in a scaled-down metal-oxide semiconductor field-effect transistor*, in Applied Physics Letters 99, no. 6 (2011): 063106.

INTL. CONFERENCES
- S. Tembhurne, S. Haussener. In Meeting Abstracts, no. 32, pp. 1561-1561. ECS, 2017.
- S. Tembhurne, F. Nandjou, S. Haussener. In Meeting Abstracts, no. 32, pp. 1560-1560. ECS, 2017.
- S. Tembhurne, S. Haussener. In Meeting Abstracts, no. 38, pp. 1921-1921. ECS, 2016.
- S. Tembhurne, S. Haussener. In Meeting Abstracts, no. 43, pp. 1745-1745. ECS, 2015.
- S. Tembhurne, M. Dumortier, S. Haussener. In Meeting Abstracts, no. 8, pp. 598-598. ECS, 2014.
- S. Tembhurne, M. Dumortier, S. Haussener. In 15th IHTC, Kyoto, Japan, 2014.
- S. Tembhurne, S. Murthy, S. Ganguly, IEEE Nano, Birmingham, UK, 2012.

KEY ENTREPRENEURIAL ACHIEVEMENTS
- Founded 'SoHHytec'- aimed at providing solar fuel the smarter way and gathered up the team.
- Winner of Nano-Tera Entrepreneurship Next step PhD program 2015 (4 kCHF)
- Winner of Buhler Energy Challenge 2015
- Best Nano-Tera Entrepreneurship Project Award 2016
- Finalist- Venture Lab's Academia-Industry Training (AIT) 2016
- Winner of EPFL Enable grant (60 kCHF) 2016-17
- Winner of Bridge PoC grant (4th call- 130kCHF) 2017-18

WORK EXPERIENCE
CIPEC device and implementation of the same   **Sep. 2013-Feb. 2018**

Laboratroy of Renewable Energy Science and Engineering| EPFL
Ph.d. Degree Thesis/ Doctoral Thesis
Guide: Prof. Sophia Haussener
Concentrated Integrated Photo-Electrochemical (CIPEC) device is designed and a detailed 2-dimensional coupled multi-physics model using finite element

and finite volume methods is developed to predict the performance of the CIPEC device. Developed performance optimization strategies utilizing device design, component and material choice, and adaptation of operational conditions. Designed and developed a fully integrated lab-scale prototype of the CIPEC device based on the design guidelines generated from the 2D model and the holistic design guidelines formulated using the techno-economic model. Designed a controller and controlling strategies for CIPEC device operation alleviating the device degradation during the lifetime of the device.

 Highlight: *US patent no. 62/376923, European patent no. EP16020308.9, 4 Journal publications and 6 conference presentations*

Plasmonic Solar Cell (PSC) Modeling and Simulation   **Jan. 2012 – Jun. 2013**

National Center for Photovoltaic Research and Education| IIT Bombay
Dual Degree Thesis / Master Thesis
Guide: Prof. Swaroop Ganguly
Developed simulation framework in TCAD Sentaurus for integration of optical and electrical simulations. Showed that co-optimizing the plasmonic structures and the basic Solar Cell (SC) simultaneously, by solving the electromagnetics and semiconductor transport equations together, is the only meaningful way to design PSCs. Formulated design guidelines and the methods for achieving 2-6 fold increase in thin film solar cell efficiency with plasmonics. Finally demonstrated the need for co-optimization of solar cell and plasmonic structure.
Highlight: *Oral presentation at IEEE Nano 2012, 12th Intl. Conf. on Nanotechnology*

Low-Dimensional Nanoelectronic Transport   **May - July 2011**

Materials Innovation and Nano-Electronics(MINE) Research Group | UTM Malaysia
Research Internship
Guide: Prof. Vijay K. Arora |Wilkes University, Pennsylvania, US
Optimized and implemented the ballistic model for carrier transport in MATLAB. Analyzed the variation of drift and magneto-resistance mobility with length & concentration. Excellent agreement with the experimental data on length-limited ballistic mobility is obtained.
Add-on: Laboratory training and hand on experience on Raman spectroscopy, Ellipsometry, Thermal CVD, Scanning e- Microscopy (SEM).
Highlight: *Co-authored Research Publication in Applied Physics Letters*

KEY ACADEMIC PROJECTS

Forster Resonance Energy Transfer   **January - April 2012**

In semester project | IIT Bombay
Guide: Prof. S. Ganguly and Prof. A. Tulapurkar

90nm MOSFET Device modeling and simulation   **November 2011**

In semester project | IIT Bombay
Guide: Prof. Souvik Mahapatra

Smart remote control of electronic appliances using Power Line Carrier Communication	January – April 2011

Electronic Design Project |IIT Bombay
Guide: Prof. M. S. Baghini and Prof. J. Mukherjee

PiN diode breakdown voltage improvement	March – April 2012

In semester project | IIT Bombay
Guide: Dr. Ritu Sodhi |Director, Fairchild Semiconductor (India) Pvt. Ltd.

Wilkinson Power Divider design	Oct. – Nov. 2010

Microwave IC design Project | IIT Bombay
Guide: Prof. J. Mukherjee

KEY SCHOLASTIC ACHIEVEMENTS

- Bridge fellow with the Bridge PoC grant for the year 2017-18.
- "Dr. Ambedkar National Merit Award" by Govt. of India for meritorious performance in XII .
- Awarded High Distinction in Australian National Chemistry Quiz (senior division)-2007.
- "Student of the year" for 2 consecutive years for extraordinary performance in all fields at the school.

SKILL SET

- **EDA tools:** COMSOL, Solidworks, Matlab, Synopsys, Lumerical, NGspice, Multisim, ADS, ANSYS, Eagle layout editor, Excel, Origin
- **Operating system:** Windows, Linux(Debian, Redhat)
- **Languages:** C++, Python, Visual C++, Verilog, 8085 assembly, Latex, HTML